6-25-2018 2:00 PM

Methods for the Investigation of Microvascular Control of Oxygen Distribution

Richard Sove
The University of Western Ontario

Supervisor
Ellis, Christopher G.
The University of Western Ontario Co-Supervisor
Fraser, Graham M.
The University of Western Ontario

Recommended Citation

Abstract

The purpose of this thesis was to develop tools for studying oxygen-dependent regulation of red blood cell (RBC) flow distribution in the microcirculation. At the microvascular level, arterioles dictate the distribution of oxygen (O_2) carrying RBCs to downstream capillaries, a process which needs to be tightly regulated and coupled to O_2 off loading from capillaries to the tissue. To investigate potential regulatory mechanisms, an O_2 exchange platform was developed to manipulate the RBC hemoglobin O_2 saturation (SO_2) at the muscle surface while limiting the changes in SO_2 to only a single capillary network. Decreasing SO_2 in a single capillary network resulted in an increase in supply rate, while increasing SO_2 caused a decrease in supply rate. This finding is consistent with our hypothesis that ATP released in capillaries in response to low SO_2 is responsible for vasodilation of upstream arterioles to regulate blood flow. To determine whether the dynamics of ATP was fast enough to enable RBC signalling in capillaries, an *in vitro* microfluidic system was developed to generate a rapid decrease in RBC SO_2. The feasibility of this experimental design was first tested computationally using a mathematical model that consisted of blood flow, oxygen and ATP transport as well as a model for hemoglobin binding, ATP release, ATP/luciferin/luciferase reaction and digital camera light detection. The model demonstrated that the concept was theoretically feasible and yielded important insights such as the signal sensitivity to flow rate. The model further revealed that measured light intensity levels would not be directly related to ATP concentrations, thus, care must be taken when interpreting the data. It was determined that the microfluidic device would be fabricated using soft lithography techniques that resulted in a device that differed significantly from our original theoretical design since all of the layers would be oxygen permeable except for a glass coverslip with a small opening for gas exchange between the liquid and gas channel. To optimize the geometric design of this microfluidic device, to maximize the desaturation the RBCs, a finite element model was developed. Based on this design a device was constructed. To test whether the design generated a rapid decrease in RBC SO_2, a low hematocrit high SO_2 RBC suspension was perfused through the device exposed to 95% N_2 and 5% CO_2 in the gas channel. Finally, to overcome challenges with existing approaches for measuring SO_2 in the device, a novel image analysis technique using digital inpainting was developed. The inpainting approach demonstrated a rapid change in RBC SO_2 at the entrance to the window, thus the microfluidic device is ready to be used to measure the dynamics of O_2-dependent ATP release from RBCs. The new inpainting algorithm was also applied to *in vivo* video sequences where it was shown

to provide more accurate SO_2 measurements and to work under conditions where existing approaches fail. In summary, this thesis provides a set of *in vivo, in vitro* and computational tools that can be used to study the mechanisms of SO_2-dependent regulation of the microvascular blood flow.

The Co-Authorship Statement

A version of the second chapter titled "Localized oxygen exchange platform for intravital video microscopy for the investigation of microvascular oxygen regulation" is in preparation for publication. This article was co-authored by Stephanie Milkovich, Hristo Nikolov, David Holdsworth, Graham Fraser, and Christopher Ellis.

A version of the third chapter titled "A Computational Model of a Microfluidic Device to Measure the Dynamics of Oxygen-Dependent ATP Release from Erythrocytes" was published in PLoS One. This article was co-authored by Nour Ghonaim, Daniel Goldman and Christopher Ellis.

A version of the fourth chapter titled "Finite Element Model of Oxygen Transport for the Design of Geometrically Complex Microfluidic Devices Used in Biological Studies" was published in PLoS One. This article was co-authored by Graham Fraser, Daniel Goldman and Christopher Ellis.

A version of the fifth chapter titled "Using digital inpainting to estimate incident light intensity for the calculation of red blood cell oxygen saturation from microscopy images" was accepted to the Journal of Biophotonics. This article was co-authored by Nicole Drakos, Graham Fraser and Christopher Ellis.

A version of the sixth chapter titled "Microfluidic Device for the Rapid Oxygen Desaturation of Hemoglobin in Red Blood Cells: A Tool for Studying Oxygen-Dependent ATP Release" is in preparation for publication. This article was co-authored by Hristo Nikolov, David Holdsworth, Graham Fraser, and Christopher Ellis.

Acknowledgments

In this section, I would like to extend my gratitude to all those who have made the completion of this work possible. I would like to acknowledge not only those who have contributed directly to the science, but also those who have played an important role leading up to the completion of this work.

Firstly, I would like to express my deepest gratitude to my supervisors Drs. Christopher Ellis and Graham Fraser for their guidance and support. I have had the privilege to benefit from two great mentors, one who has had the full experience of a successful career and one who's career is just taking off and thus has recently been through the stages through which I am about to embark. I would like to thank them for giving me the freedom to pursue my interests and for sharing their wisdom when I was in need.

Secondly, I would like to acknowledge the members of my advisory committee, Drs. Jeffery Dixon, Daniel Goldman and Stephen Sims whose advice and critical analyses of my work throughout the completion of my doctoral research have played an integral role in my development as a scientist.

I would like to extend a special thanks Stephanie Milkovich whose support and guidance in the lab were invaluable to my progress. She was also involved in the data collection for the animal work; and for that I am grateful. I would also like to thank all lab members, past and present for their support and advice throughout my degree. I am particularly grateful to Paulina Kowalewska whose insights in protocol development and hours of troubleshooting were much appreciated.

I am also grateful to all the collaborators and co-authors involved in my project, especially Daniel Lorusso who taught me the secrets of microfluidics and Hristo Nikolov who would 3D print anything I asked for.

I would like to thank NSERC and CIHR for the financial support of this work.

Finally I would like to acknowledge all of the friends and family who helped me

get through this degree, especially my parents, Chuck and Teresa Sové, and my siblings Todd, Sean and Jessica Sové who were always available to provide emotional support. A special thanks to my aunt and uncle, Madelyn and Shawn Porter who have been my home-away-from-home here in London. I would like to express the greatest appreciation to Nicole Drakos for her patience and understanding, insightful conversations, help in the editing process and continued moral support.

Table of Contents

List of Tables

List of Figures

Chapter 1

Understanding Oxygen Regulation in the Microcirculation

Oxygen (O_2) is necessary for normal cell function, and due to diffusion limitations, the circulatory system is a necessary means of delivering O_2 to most cells throughout the body. In order to meet physiological demands, our bodies must be able to adapt to changes in metabolism as well as to perturbations in O_2 supply. While O_2 regulation comprises a vast set of literature, this thesis is focused on O_2 regulation at the microvascular level, and thus this section will provide a broad overview of O_2 regulation at global scales as well as examples of proposed mechanisms at the microvascular level. For a review of vascular control mechanisms in the microcirculation, see the 2005 review by Segal [1].

Most mechanisms control O_2 supply by means of blood flow modulation; an increase in blood flow leads to an increase in O_2 supply. Blood flow can be modulated globally by increasing heart rate or contractility, or locally by controlling the vascular tone of arterioles. The latter is accomplished by contraction/relaxation of vascular smooth muscle. Modulation of heart rate can elicit a change in systemic flow rate and pressure, though this form of O_2 supply control can be inefficient since blood flow would be increased everywhere, even to regions that do not require more O_2. It is more

efficient to simply redirect flow, rather than increase flow rate everywhere.

The myogenic response provides an example of vascular tone modulation. In this mechanism, arterioles respond to local increases in blood pressure. The increased blood pressure causes the smooth muscle in the blood vessel walls to stretch, resulting in the contraction of the muscle.

For efficient regulation, O_2 supply (blood flow) must be linked to O_2 demand (rate of O_2 consumption) [2–4]. There has been evidence of O_2 supply being linked directly to the presence/absence of O_2 as well. Several studies report that the presence of O_2 leads to vasoconstriction [5–9], while the absence leads to vasodilation [10–12]. The location of the O_2 sensor remains unknown [13]. Some researchers have suggested that an O_2 sensor lies within the blood vessels of the microcirculation [10, 14–21]. Others have proposed the putative sensor is located in the tissue surrounding the vessels [22, 23]. There have also been suggestions that a sensor for O_2 lies within the RBC.

As the carrier of O_2, the RBC would be a logical choice for the sensor. For instance, in a study of hypoxia, Stein *et al.* suggested that SO_2 is a more critical determinant of O_2 supply to tissue than oxygen tension (PO_2) [24]. Since PO_2 affects the diffusion of oxygen from the blood to the tissue, and the RBCs are the only component of the system that is affected by SO_2 (through their binding to hemoglobin); this suggests that the mechanism responsible for sensing oxygen likely occurs within the RBC. There have been three mechanisms proposed where the O_2 sensor is located in the RBC.

One of the proposed RBC-mediated mechanisms is through the release of S-nitrothiol (SNO) from hemoglobin [25]. SNO has been shown to be released from the hemoglobin in RBCs in response to the conformational change associated with the deoxygenation of hemoglobin. SNO is suggested to be a vasoactive molecule that elicits vasodilation in arterioles, increasing blood flow to downstream capillaries. Despite the evidence supporting the role of SNO as a mechanism for O_2 regulation, there are numerous studies refuting this as a viable mechanism [26–28].

Another proposed mechanism suggests that fully deoxygenated hemoglobin acts as a nitrite reductase. In this mechanism, nitrite is converted to nitric oxide, which plays an important role in vasodilation [26, 29, 30]. Due to the slow dynamics associated with the reduction of nitrite, this mechanism likely lacks the temporal resolution required to tightly regulate O_2 supply [31].

Finally, ATP has been shown to be released from RBCs in response to low O_2 [32] and other stimuli [32–34]. The ATP released into the plasma of blood vessels binds to receptors on the membrane of the endothelial cells lining the vessel lumen [35]. This is thought to trigger a conducted signal through gap junctions in the endothelium, leading to vasodilation of upstream arterioles [36, 37]. Of the three mechanisms discussed above, this third mechanism is the only mechanism capable of triggering a conducted vasodilatory response, enabling the capillaries, the primary site of O_2 exchange, to contribute to regulation of O_2 [31].

The main goal of this thesis is to develop tools to study O_2-dependent ATP release in RBCs. Evidence for O_2-dependent ATP release will be presented in Section 1.1, followed by an introduction to some important methodology that can be applied

to the study of the local regulation of O_2 distribution. In particular, fundamental principles of hemoglobin SO_2 measurements (Section 1.2), the basics of computational modelling (Section 1.3), and an introduction into microfluidics (Section 1.4) will be discussed. Finally, the outline of this thesis will be presented in Section 1.5.

1.1 Oxygen-Dependent ATP Release from Red Blood Cells

In 1919, August Krogh proposed a mathematical model of O_2 delivery to tissue [38]. His idealized model assumed that each capillary in a tissue supplied a cylinder of tissue surrounding it. In his model, all of O_2 delivery was assumed to happen at the level of capillaries, thus each capillary had the same entrance O_2 concentration. The model suggested that the size of the tissue cylinder is dictated by the concentration of O_2 in the capillaries and the O_2 consumption rate of tissue. Based on this, it was proposed that increasing capillary density could compensate for increased metabolic demand.

Since Krogh's work, many researchers have been searching for mechanisms for capillary recruitment. However, this view that capillaries have uniform O_2 content is over-simplistic; in 1970, Dulling and Berne demonstrated a substantial loss of O_2 in artierioles [39]. Various animal models and tissue preparations have confirmed this finding [40–42]. There is also evidence for O_2 exchange from arterioles to capillaries [18]. These findings suggest that there is a diffusional loss of O_2 in arterioles, leading to a radial gradient across the arteriole where O_2 content of RBCs nearest to the wall would be lower than those travelling near the centreline [43, 44], since O_2 would be lost through the wall. At asymmetric bifurcations, slower flowing RBCs near the wall

would flow down the low-flow branch of the bifurcation, leading to a heterogeneous distribution of O_2. This evidence lead to a contradiction of the original assumptions in Krogh's model. Due to the complexity of O_2 distribution in the circulation, a more locally sensitive mechanism is required to regulate the distribution of O_2 to meet metabolic demands. As discussed in the previous section, one potential mechanism is the O_2-dependent release of ATP from RBCs.

In the late 1940s, the optical detection and measurement of ATP was made possible following the finding that firefly lantern extract (known today as firefly luciferin and luciferase) luminesces in the presence of ATP [45]. This assay was further refined by Strehler and McElroy in 1957 [46]. Since then, many researchers have used this assay to investigate the presence of extracellular ATP in various tissues and organs [47–49]. For example, Forrester and Lind detected ATP in human blood plasma [48]; this was the first hint at ATP release from RBCs.

Oxygen-dependent ATP release from RBCs was first measured by Bergfeld and Forester in 1992 [32]. They used the firefly luciferase assay to measure a significant increase in plasma ATP concentrations following exposure to low O_2 and high pH. In 1995, Ellsworth *et al.* were able to isolate the two effects and measured increased plasma ATP concentrations in response to O_2 with a fixed pH [33].

It was further shown that the injection of ATP into the vascular lumen leads to a dose-dependent vasodilatory response [50]. This is proposed to be triggered by the binding of ATP to the purinurgic receptor, P_{2Y2}, on the inner luminal wall [35, 37, 51–53]. The purinurgic activation results in the synthesis and release of vasodilators, such as nitric oxide (NO) and prostacyclin (PGI_2), which act to relax the vascular smooth muscle in

arterioles [54]. This cascade also activates calcium-sensitive potassium channels, leading to hyperpolarization of endothelial and/or smooth muscle cells [55–57]; smooth muscle hyperpolarization leads to dialtion [58, 59]. Hyperpolarization can be conducted through gap junctions to adjacent endothelial/smooth muscle cells, leading to a conducted vasodilatory response [55–57]. Further evidence for ATP release has shown that decreasing the O_2 content of blood vessels in the absence of RBCs elicits no vascular response [34].

Jagger *et al.* showed a linear relationship between the steady-state RBC SO_2 and the amount of ATP released [60]. This lead to the hypothesis that ATP release was related to the conformational change in hemoglobin due to its change in saturation. This hypothesis was supported by using carbon monoxide to keep hemoglobin in its saturated conformation and varying the O_2 content of the RBCs. This was further confirmed by several human studies [61–63].

The ATP release mechanism for O_2 regulation was also supported by Ghonaim *et al. in vivo* by manipulating the surface O_2 levels of a rat skeletal muscle preparation using a gas exchange chamber [64]. They showed that a change in tissue O_2 leads to a change in supply rate. ATP release has also been shown to be altered in diseases such as prediabetes [65, 66], type II diabetes [67] and sepsis [68].

In the current view of ATP release, ATP is released from RBCs into capillaries under local hypoxic conditions. The ATP released into the plasma is then able to bind to receptors on the endothelium of the capillary which RBCs are in contact with. This triggers a conducted vasodilatory response upstream to feeding arterioles that can then dilate to increase RBC flow, and hence O_2 supply. Figure 1.1 shows the pro-

posed mechanism for a single RBC signalling to capillary endothelial cells. Since the RBCs (sensors) are moving through the capillaries, the time-dependence (dynamics) of ATP release dictates the ability of the regulatory system to accurately report the location of low O_2; if ATP is released too late, the RBC will be far downstream from the site of low O_2.
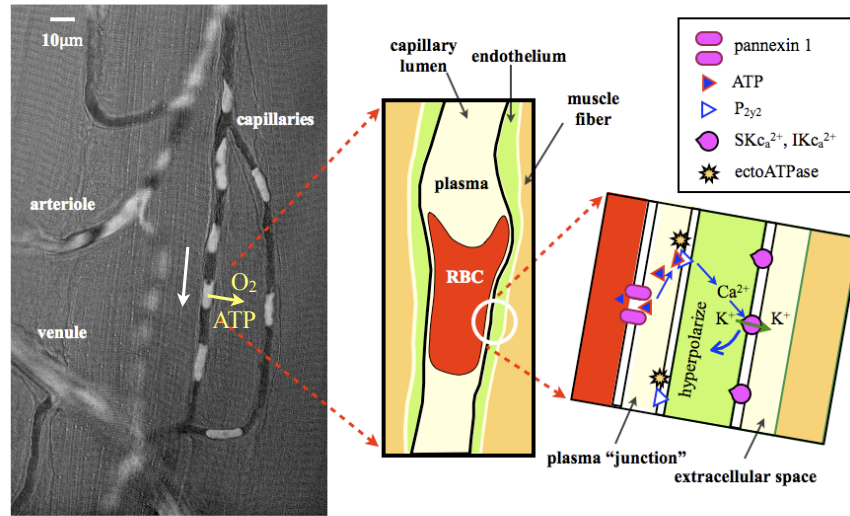
Figure 1.1: *Current understanding of O_2-dependent ATP release from RBCs. Anatomic composite image from a single 40X microscopy video frame (opacity 64%) superimposed on a functional image (left). The video frame was processed as optical density such that low values (black) represent background and high values (white) represent high absorbers, such as RBCs. The functional image consists of the minimum pixel intensity over time; in the functional image areas with passing cells appear dark. The white arrow indicates the direction of RBC flow. (Center) Schematic representation of a single RBC in close contact with the capillary endothelium. (Right) Schematic representation of the ATP release mechanism in response to low O_2. Following RBC desaturation, ATP is release through pannexin 1 channels in the RBC membrane. ATP in the vessel lumen either binds to endothelial P_{2Y2} receptors or is degraded by ectoATPases. P_{2Y2} binding activates Ca^{2+}-sensitive potassium channels, resulting in hyperpolarization of the endothelial cell, which can be conducted through gap junctions. This figure was adapted from [69].*

In summary, ATP release seems to be an important mechanism in the regulation of O_2, however, its dynamics have not yet been fully elucidated. The main goal

of this thesis is to develop methodology to explore the dynamics of O_2-dependent ATP release. Since this mechanism is dependent on RBC SO_2, the methodology developed in this thesis involves perturbing SO_2. Therefore quantifying the degree of desaturation is imperative. Section 1.2 outlines the methodology behind optical measurements of SO_2 from microscopy images.

1.2 Measuring Hemoglobin Oxygen Saturation

The measurement of hemoglobin oxygen saturation (SO_2) is made possible by the spectral properties of hemoglobin; hemoglobin absorbs light differently based on the binding of oxygen. Figure 1.2 shows the hemoglobin absorption spectrum for fully saturated- and fully desaturated-hemoglobin in the visible light spectrum; data in this figure were tabulated by Scott Prahl [70]. The quantity shown in this figure is called the molar extinction coefficient, which is a measure of the amount of light absorbed per concentration of hemoglobin per path length. It is specifically defined in the relationship between incident and transmitted light:

$$I = I_0 10^{-\varepsilon(\lambda)cx}, \tag{1.1}$$

where I_0 is the incident light intensity, I is the intensity of light transmitted through the hemoglobin sample, c is the concentration of hemoglobin and x is the path length. The extinction coefficient of hemoglobin at wavelength λ is given by $\varepsilon(\lambda)$. The argument of the exponential is known as optical density $OD \equiv \varepsilon cx$ and can be calculated by
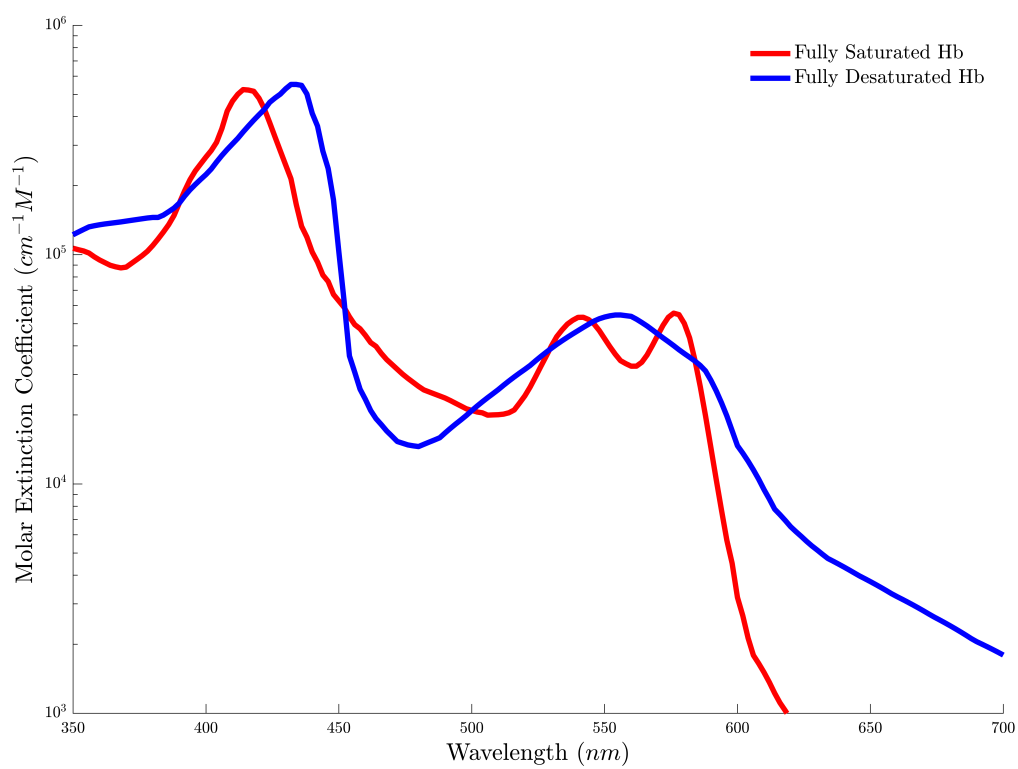
Figure 1.2: *Extinction coefficient for fully oxygen saturated- (red) and fully oxygen desaturated- (blue) hemoglobin as a function of wavelength in the visible range.*

$$OD = \log_{10}\left(\frac{I_0}{I}\right). \tag{1.2}$$

Expanding the optical density expression, $OD = \varepsilon c x$, the optical density of red bloods cells can be written as

$$OD(\lambda) = \left(\varepsilon_{Hb_{O_2}}(\lambda)SO_2 + \varepsilon_{Hb}(\lambda)(1 - SO_2)\right)cx, \tag{1.3}$$

where SO_2 is hemoglobin oxygen saturation and $\varepsilon_{Hb_{O_2}}$ and ε_{Hb} are the extinction coefficients for fully saturated- and fully desaturated- hemoglobin, respectively.

Given the optical density of RBCs at two wavelengths, λ_1 and λ_2 we can determine SO_2 by taking the ratio of the optical densities and solving for SO_2.

$$SO_2 = \frac{b_1 - b_2 R}{a_2 R - a_1} \tag{1.4a}$$

$$R = \frac{OD(\lambda_1)}{OD(\lambda_2)} \tag{1.4b}$$

$$a_i = \varepsilon_{Hb_{O_2}}(\lambda_i) - \varepsilon_{Hb}(\lambda_i) \tag{1.4c}$$

$$b_i = \varepsilon_{Hb}(\lambda_i) \tag{1.4d}$$

where the constants a_1, a_2, b_1 and b_2 are usually obtained by calibration with RBCs of known SO_2. If the second wavelength, λ_2, is chosen to be O_2-independent, also called isosbestic, the relationship between optical ratio and SO_2 becomes linear [71].

The intensity value, I, can be measured from the pixel intensity in an image. The incident light, I_0, however, is not directly measurable. This value is often approximated using video data to measure the light intensity of the plasma gaps between the RBCs as they travel single file through the capillaries [72]. As the RBCs move out of the way, the plasma intensity gives the intensity of the pixels behind the RBC. This can be accomplished algorithmically by calculating the maximum intensity at each pixel over a specified number of frames, since RBCs absorb more light, and thus have lower intensity values than the plasma. In Japee *et al.*, the maximum intensity minus three standard deviations is used as the value for I_0. In more recent studies, the maximum value is used since low-noise digital cameras are used to acquire the images.

Overall, RBC SO_2 provides a good measure of tissue oxygenation [24] and is a invaluable tool in the study of O_2 regulation. However, there are scenarios in which we would like to determine concentrations of O_2 that may be difficult or impossible to measure. Computational modelling provides a useful way to predict the spatial distribution of oxygen and other physical quantities based on mathematical models. Section 1.3 presents a simplified overview of computational modelling based on conservation laws and some useful numerical techniques that can be used to solve the governing partial differential equations.

1.3 Computational Modelling

Computational modelling consists of using computers to simulate the behaviour of complex processes based on a mathematical representation; they can be used to simulate physiological scenarios to facilitate the understanding of the system without the time or cost associated with experiments. For instance, to study the effect of capil-

lary perfusion loss on tissue oxygenation, Fraser *et al.* used a computational model of O_2 transport to predict tissue oxygenation where perfusion loss was simulated by systematically removing capillaries from the simulation [73]. This approach is more feasible than using an experimental model where more variability is introduced.

Various types of mathematical models can be constructed based on the goals and needs of the study. The mathematical models in this thesis are constructed based on the physical principle of conservation. In conservation models, the dependent variables are often functions of space. These models can also be either dynamic (time-dependent), or steady-state (constant in time). This section outlines how these types of mathematical models are formulated followed by several strategies for solving the governing equations on a computer.

1.3.1   Mathematical Models

Many mathematical models are formulated as a (set of) partial differential equation(s) (PDE(s)) that describe the how a physical phenomenon varies through space and/or evolves over time. These PDEs are generally formulated from conservation laws, such as the conservation of mass. Once the set of PDEs are determined, a set of initial and boundary conditions are required to obtain a unique solution. Physical models based on conservation principles result in PDEs of the following form

$$\frac{\partial u}{\partial t} + \vec{v} \cdot \nabla u = \nabla \cdot (D\nabla u) + s, \tag{1.5}$$

where u is the quantity of interest. The first term on the left hand side of the PDE

represents the evolution of u over time and the second term represents spatial translation of u at the velocity, $\vec{v}$. On the right hand side, the first term represents the diffusion of u where D dictates the extent of diffusion and the second term represent sources/sinks of u, where s is the strength of the source/sink. For example, in the context of mass transport, u would be solute concentration. The terms of the PDE from left to right would represent temporal evolution, convection, diffusion, and secretion/consumption, respectively.

To define the system uniquely, a set of initial/boundary conditions must be defined. Initial conditions define the system at the beginning of the time of interest at every point in space and the boundary conditions define the system at the boundaries of the domain for all time after $t = 0$. Initial and boundary conditions are generally given in terms of the dependent variable or its derivatives.

In general, PDEs cannot be solved exactly; in order to obtain a solution, a numerical approximation must be made. There are three common classes of approximation techniques for PDEs: (1) the finite difference method (FDM), (2) the finite volume method (FVM) and (3) the finite element method (FEM). Each discretization method, solves for the function of interest, $u(x, y, z, t)$, at discrete points in time and space, u_i^n (where n is the time index and i is the spatial index).

1.3.2   Finite Difference Method

FDM approximates the derivatives in the PDE using a difference approximation. In order to obtain an approximation of the partial derivatives, the time and spatial domains need to be discretized into a grid such that the grid lines lie along the coordinate directions. Continuous functions can then be expressed as a set of discrete

values organized into a tabular structure (e.g. $f(x, y, z, t) \approx f_{i,j,k}^n$). One example of a finite difference approximation is called Euler's method and is defined as follows

$$\frac{\partial u}{\partial t} \approx \frac{u_{i,j,k}^{n+1} - u_{i,j,k}^n}{\Delta t^n}, \tag{1.6}$$

where Δt^n is the n$^{\text{th}}$ temporal step size. This FDM approximation is first order, meaning the error is linearly proportional to Δt. More accurate schemes can be derived using higher-order Taylor-series expansions.

Using these difference approximations, we can write the entire differential equation in terms of discrete variables. This procedure transforms the PDE into a system of algebraic equations which can then be solved computationally.

The finite difference method is generally quite simple to implement and can be used to discretize even the most complex PDEs. The main disadvantage to the FDM is that it is not straightforward to implement for complex geometries. For more complicated geometries, the finite difference method is often used to approximate the temporal derivatives and the rest of the PDE can be discretized using either FVM or FEM.

1.3.3 Finite Volume Method

FVM uses a discrete approximation of the integral form of the conservation law. Equation 1.5 can be rewritten as the following integral equation

$$\int_{\partial\Omega} \hat{n} \cdot (\vec{v}u - D\nabla u)\, dA = \int_{\Omega} s\, dV, \tag{1.7}$$

where Ω is the spatial domain and $\partial\Omega$ is the boundary; $\hat{n}$ is the unit normal to the boundary.

The integrals are approximated by a discrete summation. One example would be the midpoint rule on a cubic volume:

$$\int_0^1 \int_0^1 \int_0^1 f(x,y,z)dxdydz \approx f\left(\frac{x_i}{2}, \frac{y_i}{2}, \frac{z_i}{2}\right)\Delta x_i^3, \tag{1.8}$$

where i is the volume's index and Δx_i are the side lengths of the cubic volume elements. This quadrature rule is first-order accurate; more accurate schemes can be derived. Once each integral in the equation is approximated, a system of algebraic equations are obtained and can be solved using a computer.

1.3.4 Finite Element Method

FEM uses variational calculus to minimize the residual, R, of the spatial PDE. The residual of the PDE presented in Equation 1.5 is given by

$$R(\tilde{u}) = \vec{v} \cdot \nabla\tilde{u} - \nabla \cdot (D\nabla\tilde{u}) - s, \tag{1.9}$$

for some function $\tilde{u}$. If the residual of the PDE is zero then $u = \tilde{u}$ is the solution.

The fundamental theorem of variation calculus states that if

$$\int_\Omega v(\vec{x})w(\vec{x})dV = 0, \tag{1.10}$$

for all $w(\vec{x})$, then $v(\vec{x}) = 0$ for all $\vec{x}$ in Ω. This theorem can be used to constrain the residual to zero. Rewriting the theorem using the residual we find:

$$\int_\Omega w(\vec{x}) \left(\vec{v} \cdot \nabla u - \nabla \cdot (D\nabla u) - s \right) dV = 0, \tag{1.11}$$

The dependent variable, u, is then chosen to be

$$u(\vec{x}) = \sum_i^N u_i\phi_i, \tag{1.12}$$

where ϕ_i is the ith shape function of the spatial discretization. The shape function has the properties that $\phi_i = 1$ at the ith node of the spatial discretization and 0 at every other node and ϕ_i varies according to a polynomial along the adjacent elements (for example ϕ_i can be piecewise linear). This choice of u results in an algebraic equation with N unknowns; the system is closed with the choice of N different $w(\vec{x})$ functions. One example is the Galerkin method which chooses $w_j = \phi_j$ [74].

1.3.5   Solution of Algebraic Equations

After obtaining the system of equations, it must be solved to get the approximate solution to the PDE. There are many methods to solve linear systems of equations, most of them rely on an iterative procedure. The solver should be chosen based on the size and shape of the resulting matrix. For example, if the matrix is symmetric and positive definite, the conjugate gradient method solves the system in $O(n)$ operations. The generalized minimal residual (GMRES) method is a more robust linear solver that works for any matrix [75]. With GMRES, speed is sacrificed in order to handle a more general problem.

1.3.6   Mathematical Modelling in This Thesis

This thesis uses numerous computational models and numerical techniques in the development of tools to study microvascular O_2 regulation. In particular, we use the finite difference and finite element methods. The finite difference method is the simplest to implement for simple geometries; for more complex geometries, the finite element method is used.

In Chapter 2, an *in vivo* microfluidic device is developed to perturb the local O_2 levels in a rat skeletal muscle preparation. A time-dependent computational model of O_2 transport is used to estimate how far into the muscle the perturbations extend; this model is discretized using the finite difference method and parallelized to reduce computation time. Chapters 3, 4 and 6 present the design, development, fabrication and validation of an *in vitro* microfluidic device designed to measure the release time of ATP from RBC in response to low O_2. In Chapter 3, computational modelling is used to simulate the *in vitro* experiment to determine if it is theoretically feasible;

these PDEs are discretized using the finite difference method. In Chapter 4, a 3D model of the O_2 transport through the microfluidic device is used to optimize its geometry. The finite element method was used for the discretization to facilitate the use of arbitrarily complex geometries. Finally, Chapter 5 presents an image analysis method to estimate RBC SO_2. Though no physical models are used, partial differential equations are used to estimate the incident light intensity; these equations are discretized using the finite difference method.

In summary, mathematical modelling is a useful tool for predicting the transport of O_2 in systems used to study microvascular O_2 regulation, both *in vivo* and *in vitro*. Computational modelling, however, does not address design considerations related to the fabrication of microfluidic devices. Section 1.4 presents a selective overview of microfluidic fabrication techniques.

1.4 Microfluidic Device Fabrication Principles

Microfluidics is a rapidly emerging field with a wide range of scientific applications. It is defined as the manipulation of fluids in channels having characteristic lengths on the order of tens to hundreds of micrometers [76]. Microfluidics were first developed in the 1970s using techniques from the well-established field of microelectronics [77]. In the 1990s, microfluidics began to rapidly grow as research expanded into the use of new classes of materials, notably polymers [76]. Applications include rapid analysis of bodily fluids (e.g. blood) [78], point of care diagnosis [79], analysis of environmental contaminants [80], fluid dynamics [81], *in vivo* drug delivery [82] and biomimetic systems [83].

Microfluidics have several advantages over many other experimental methods since they have lower reagent consumption due to the small volumes used and allow for higher throughput. Further, with the advances in polymer fabrication techniques, microfluidic devices have low manufacturing costs and their fabrication process has become accessible to general scientists [84]. This allows for the fabrication of specialized microfluidic devices with relative ease, therefore, microfluidic devices can be rapidly prototyped, accelerating research progress.

The objective of this section is to outline the basic principles of common fabrication techniques. Section 1.4.1 will begin with considerations with regards to the materials used in the fabrication of microfluidic device. Next, Section 1.4.2 will describe several common techniques used to fabricate components used in the production. Finally, select popular bonding techniques will be discussed in Section 1.4.3.

1.4.1   Material Considerations

Early microfluidic devices were primarily fabricated in glass or silicon using photolithography and chemical etching [85, 86]. Glass has the benefit of being optically transparent, electrically insulating, thermally conducting, rigid and resistant to most organic solvents. Silicon has similar benefits to glass, though it is optically opaque and is electrically conductible. During the etching process, silicon is able to maintain vertical side walls, whereas channels etched in glass result in curved side walls [87]. Additionally, the fabrication process for both materials requires a clean room, dangerous chemicals in the etching process and high pressures or temperatures in the bonding process [85, 88]. Thus, the manufacturing process for microfluidic devices fabricated in glass or silicon generally require a special facility and often have large costs.

More recently, polymers have become a popular class of materials to use in the fabrication of microfluidic device [76]. Polymers can be classified into three categories; (1) thermosets, (2) thermoplastics and (3) elastomers.

Thermosets are polymers that become cross-linked and harden when heated or irradiated. After hardening, thermosets cannot be reshaped, thus they are stable at high temperatures. Further, they are resistant to most solvents and optically transparent. Their high strength makes them ideal for fabricating channels with high aspect ratios. One thermoset used in microfluidics is the UV-sensitive epoxy SU-8 [89]. Though, due to the high cost of thermosets, they have limited applications in microfluidics [90].

Thermoplastics are solid polymers that, when heated become soft and moldable. Common thermoplastics include poly(methylmethacrylate) (PMMA), polycarbonate, polystyrene, polyvinyl chloride (PVC) and polyethylene terephthalate (PET) [91]. Thermoplastics can be reshaped multiple times, which allows for a flexible manufacturing process. Like thermosets, they are typically rigid and impermeable to gases, though they are incompatible with most organic solvents (e.g. ketones and hydrocarbons). Due to the high temperatures required, thermoplastics tend to have more applications in commercial manufacturing of microfluidics than in an academic setting [90].

Elastomers are polymers that consist of entangled cross-linked polymer chains. The entanglement gives elastomers their elastic property. Due to their porous structure, elastomers tend to be permeable to gases and other small molecules. This makes elastomers incompatible with many solvents, since small molecules dissolved in the

solvent can be adsorbed into the elastomer [92]. However, their elasticity allows them to be used as valves in microfluidic devices [93]. The most common elastomer in microfluidics is poly(dimethyl siloxane) (PDMS) [76]. PDMS is inexpensive and optically transparent.

1.4.2 Fabrication Techniques

In the fabrication of microfluidic channels, a cavity is made in the material to form a channel, the channel is then sealed with a flat piece of material by some bonding process. The process by which the channel is formed depends on the material used.

For glass and silicon, the most common method for forming the channel is using photolithography to etch the cavity into the material. The glass or silicon is first cleaned thoroughly, then a photoresist is spin coated onto the substrate. Following this, a photomask is applied and the substrate with photoresist is exposed to light. The glass/silicon is then treated with a chemical to etch the material where the photoresist is absent. The depth of the channel is dictated by the length of exposure. After the etching is done, the remaining photoresist is removed. This process yields rectangular channels for silicon and rounded channels for glass, where the curvature depends on the chemical used for etching and depth.

For polymers, the most common method is replica molding, where the polymer is cast onto a master containing a positive resist of the channel. After the polymer is cured, the replica is removed from the mold and is ready to be sealed. The master molds are usually fabricated using photolithography [84] or micro-machining [93].

Thin membranes are often required for applications in microfluidics; for elastomers, this is generally formed by way of spin coating. The spin coating process allows for a thin, even layer of the polymer to be made. The thickness of the layer is controlled by the angular frequency of the rotating plate. The time for spin coating must be carefully chosen; the time must be sufficient for the process to reach steady state, but not so long that evaporation occurs.

1.4.3   Bonding Techniques

Once the individual components are fabricated, they are bonded together to form the final microfluidic device. This section will outline popular bonding techniques for PDMS. For components made from glass or silicon, fusion or anodic bonding can be used. For a complete review, see [94]. Four methods will be discussed: oxygen plasma, varying curing ratio, partial curing and corona treatment.

In the oxygen plasma method, the contact surfaces of two PDMS components are brought into conformal contact after being treated with oxygen plasma. This process oxidizes the surfaces to allow the PDMS structures to be irreversibly bonded [84]. This method results in hydrophilic surfaces, which have the benefit of allowing easier fluid filling, though this benefit subsides over time [95]. The main drawbacks of this method are that it is expensive and must be done in an evacuated chamber in clean-room conditions.

In the varying curing agent method, different ratios of prepolymer and cross-linker are used to create the bond. In this method, one of the components is made with more prepolymer than cross-linker, while the second component will be made with more cross-linker [96]. This approach is advantageous since it does not require ad-

ditional surface treatment, however, it may not be suitable for all applications since the material properties will vary throughout the PDMS [95].

In the partial curing method, a fully cured component is put into contact with a partially cured component, resulting in an irreversible bond. This method has been shown to be effective and inexpensive for making multilayered devices [95].

In the corona discharge method, a handheld device generates a high electric field on the surface of fully cured PDMS, causing surface oxidization [97]. This process can be done at room temperature and pressure, without the need of a vacuum system [95].

1.5   Purpose

The objective of this thesis is to develop methodology that can be used to study the complex regulatory mechanisms involved in the regulation of O_2 distribution. Overall, it presents the development of two microfluidic devices. The first device, presented in Chapter 2 is an *in vivo* device that can be used to perturb the local O_2 content of specific networks of capillaries in order to interrogate the regulatory mechanisms of the microvasculature. The next two chapters detail mathematical models used to design an *in vitro* device that can probe the O_2-dependent ATP release from RBCs in isolation. Specifically, Chapter 3 presents a theoretical model of an *in vitro* experiment designed to measure the temporal behaviour of O_2-dependent ATP release from RBCs. Chapter 4 uses a finite element model of O_2 transport through the proposed device in order to optimize the geometric design. To assess the ability of this device to desaturate RBCs, current *in vivo* methodology for measuring SO_2

needs to be extended in order to apply to the *in vitro* images; Chapter 5 details an image processing algorithm to we developed to do this. Chapter 6 presents the actual fabrication of this *in vitro* microfluidic device, and verifies its ability to deoxygenate RBCs. Finally, Chapter 7 discusses the implications of the findings of this work and potential avenues to be pursued in the future.

References

[1] S. S. Segal, "Regulation of blood flow in the microcirculation," *Microcirculation*, vol. 12, no. 1, pp. 33–45, 2005.

[2] H. V. Sparks, "Effect of local metabolic factors on vascular smooth muscle," *Comprehensive Physiology*, 1980.

[3] H. A. Kontos and E. P. Wei, "Oxygen-dependent mechanisms in cerebral autoregulation," *Annals of Biomedical Engineering*, vol. 13, no. 3-4, pp. 329–334, 1985.

[4] A. S. Golub and R. N. Pittman, "Bang-bang model for regulation of local blood flow," *Microcirculation*, vol. 20, no. 6, pp. 455–483, 2013.

[5] B. R. Duling, "Microvascular responses to alterations in oxygen tension," *Circulation Research*, vol. 31, no. 4, pp. 481–489, 1972.

[6] P. M. Hutchins, R. F. Bond, and H. D. Green, "Participation of oxygen in the local control of skeletal muscle microvasculature," *Circulation Research*, vol. 34, no. 1, pp. 85–93, 1974.

[7] Y. Zhu, T. Park, and J. M. Gidday, "Mechanisms of hyperoxia-induced reductions in retinal blood flow in newborn pig," *Experimental Eye Research*, vol. 67, no. 3, pp. 357–369, 1998.

[8] D. G. Welsh, W. F. Jackson, and S. S. Segal, "Oxygen induces electromechanical coupling in arteriolar smooth muscle cells: a role for L-type Ca^{2+} channels," *American Journal of Physiology-Heart and Circulatory Physiology*, vol. 274, no. 6, pp. H2018–H2024, 1998.

[9] J. C. Frisbee and J. H. Lombard, "Parenchymal tissue cytochrome P450 4A enzymes contribute to oxygen-induced alterations in skeletal muscle arteriolar tone," *Microvascular Research*, vol. 63, no. 3, pp. 340–343, 2002.

[10] R. N. Pittman and B. R. Duling, "Oxygen sensitivity of vascular smooth muscle: I. in vitro studies," *Microvascular Research*, vol. 6, no. 2, pp. 202–211, 1973.

[11] K. Fredricks, Y. Liu, and J. H. Lombard, "Response of extraparenchymal resistance arteries of rat skeletal muscle to reduced PO_2," *American Journal of Physiology-Heart and Circulatory Physiology*, vol. 267, no. 2, pp. H706–H715, 1994.

[12] J. C. Frisbee, K. G. Maier, J. R. Falck, R. J. Roman, and J. H. Lombard, "Integration of hypoxic dilation signaling pathways for skeletal muscle resistance arteries," *American Journal of Physiology-Regulatory, Integrative and Comparative Physiology*, vol. 283, no. 2, pp. R309–R319, 2002.

[13] W. F. Jackson, "Arteriolar oxygen reactivity: where is the sensor and what is the mechanism of action?," *The Journal of Physiology*, vol. 594, no. 18, pp. 5055–5077, 2016.

[14] B. R. Duling, "Oxygen sensitivity of vascular smooth muscle. II. in vivo studies," *American Journal of Physiology–Legacy Content*, vol. 227, no. 1, pp. 42–49, 1974.

[15] W. F. Jackson and B. R. Duling, "The oxygen sensitivity of hamster cheek pouch arterioles. in vitro and in situ studies.," *Circulation Research*, vol. 53, no. 4, pp. 515–525, 1983.

[16] W. F. Jackson, "Arteriolar oxygen reactivity: where is the sensor?," *American Journal of Physiology-Heart and Circulatory Physiology*, vol. 253, no. 5, pp. H1120–H1126, 1987.

[17] M. L. Ellsworth, A. S. Popel, and R. N. Pittman, "Assessment and impact of heterogeneities of convective oxygen transport parameters in capillaries of striated muscle: experimental and theoretical," *Microvascular Research*, vol. 35, no. 3, pp. 341–362, 1988.

[18] M. L. Ellsworth and R. N. Pittman, "Arterioles supply oxygen to capillaries by diffusion as well as by convection," *American Journal of Physiology-Heart and Circulatory Physiology*, vol. 258, no. 4, pp. H1240–H1243, 1990.

[19] R. L. Hester, "Uptake of metabolites by postcapillary venules: mechanism for the control of arteriolar diameter," *Microvascular Research*, vol. 46, no. 2, pp. 254–261, 1993.

[20] E. J. Messina, D. Sun, A. Koller, M. S. Wolin, and G. Kaley, "Increases in oxygen tension evoke arteriolar constriction by inhibiting endothelial prostaglandin synthesis," *Microvascular Research*, vol. 48, no. 2, pp. 151–160, 1994.

[21] A. Pries, J. Heide, K. Ley, K.-F. Klotz, and P. Gaehtgens, "Effect of oxygen tension on regulation of arteriolar diameter in skeletal muscle in situ," *Microvascular Research*, vol. 49, no. 3, pp. 289–299, 1995.

[22] F. J. Haddy and J. B. Scott, "Metabolically linked vasoactive chemicals in local regulation of blood flow.," *Physiological Reviews*, vol. 48, no. 4, pp. 688–707, 1968.

[23] D. R. Harder, J. Narayanan, E. K. Birks, J. F. Liard, J. D. Imig, J. H. Lombard, A. R. Lange, and R. J. Roman, "Identification of a putative microvascular oxygen sensor," *Circulation Research*, vol. 79, no. 1, pp. 54–61, 1996.

[24] J. C. Stein and M. L. Ellsworth, "Capillary oxygen transport during severe hypoxia: role of hemoglobin oxygen affinity," *Journal of Applied Physiology*, vol. 75, no. 4, pp. 1601–1607, 1993.

[25] J. S. Stamler, L. Jia, J. P. Eu, T. J. McMahon, I. T. Demchenko, J. Bonaventura, K. Gernert, and C. A. Piantadosi, "Blood flow regulation by S-nitrosohemoglobin in the physiological oxygen gradient," *Science*, vol. 276, no. 5321, pp. 2034–2037, 1997.

[26] R. P. Patel, N. Hogg, N. Y. Spencer, B. Kalyanaraman, S. Matalon, and V. M. Darley-Usmar, "Biochemical characterization of human S-nitrosohemoglobin effects on oxygen binding and transnitrosation," *Journal of Biological Chemistry*, vol. 274, no. 22, pp. 15487–15492, 1999.

[27] M. T. Gladwin, J. R. Lancaster, B. A. Freeman, and A. N. Schechter, "Nitric oxide's reactions with hemoglobin: a view through the SNO-storm," *Nature Medicine*, vol. 9, no. 5, pp. 496–500, 2003.

[28] M. T. Gladwin and A. N. Schechter, "NO contest," 2004.

[29] K. Cosby, K. S. Partovi, J. H. Crawford, R. P. Patel, C. D. Reiter, S. Martyr, B. K. Yang, M. A. Waclawiw, G. Zalos, X. Xu, *et al.*, "Nitrite reduction to nitric oxide by deoxyhemoglobin vasodilates the human circulation," *Nature Medicine*, vol. 9, no. 12, pp. 1498–1505, 2003.

[30] M. T. Gladwin, J. H. Crawford, and R. P. Patel, "The biochemistry of nitric oxide, nitrite, and hemoglobin: role in blood flow regulation," *Free Radical Biology and Medicine*, vol. 36, no. 6, pp. 707–717, 2004.

[31] M. L. Ellsworth, C. G. Ellis, D. Goldman, A. H. Stephenson, H. H. Dietrich, and R. S. Sprague, "Erythrocytes: oxygen sensors and modulators of vascular tone," *Physiology*, vol. 24, no. 2, pp. 107–116, 2009.

[32] G. Bergfeld and T. Forrester, "Release of ATP from human erythrocytes in response to a brief period of hypoxia and hypercapnia," *Cardiovascular Research*, vol. 26, no. 1, pp. 40–47, 1992.

[33] M. L. Ellsworth, T. Forrester, C. G. Ellis, and H. H. Dietrich, "The erythrocyte as a regulator of vascular tone," *American Journal of Physiology-Heart and Circulatory Physiology*, vol. 269, no. 6, pp. H2155–H2161, 1995.

[34] R. S. Sprague, M. L. Ellsworth, A. H. Stephenson, and A. J. Lonigro, "ATP: the red blood cell link to NOs and local control of the pulmonary circulation," *American Journal of Physiology-Heart and Circulatory Physiology*, vol. 271, no. 6, pp. H2717–H2722, 1996.

[35] L. Corr and G. Burnstock, "Analysis of P2-purinoceptor subtypes on the smooth muscle and endothelium of rabbit coronary artery.," *Journal of Cardiovascular Pharmacology*, vol. 23, no. 5, pp. 709–715, 1994.

[36] D. M. Collins, W. T. McCullough, and M. L. Ellsworth, "Conducted vascular responses: communication across the capillary bed," *Microvascular Research*, vol. 56, no. 1, pp. 43–53, 1998.

[37] M. Malmsjö, D. Erlinge, E. D. Högestätt, and P. M. Zygmunt, "Endothelial P2Y receptors induce hyperpolarisation of vascular smooth muscle by release of endothelium-derived hyperpolarising factor," *European journal of pharmacology*, vol. 364, no. 2, pp. 169–173, 1999.

[38] A. Krogh, "The number and distribution of capillaries in muscles with calculations of the oxygen pressure head necessary for supplying the tissue," *The Journal of Physiology*, vol. 52, no. 6, pp. 409–415, 1919.

[39] B. R. Duling and R. M. Berne, "Longitudinal gradients in periarteriolar oxygen tension," *Circulation Research*, vol. 27, no. 5, pp. 669–678, 1970.

[40] D. P. Swain and R. N. Pittman, "Oxygen exchange in the microcirculation of hamster retractor muscle," *American Journal of Physiology-Heart and Circulatory Physiology*, vol. 256, no. 1, pp. H247–H255, 1989.

[41] M. L. Ellsworth, C. G. Ellis, A. S. Popel, and R. N. Pittman, "Role of microvessels in oxygen supply to tissue," *Physiology*, vol. 9, no. 3, pp. 119–123, 1994.

[42] A. G. Tsai, P. C. Johnson, and M. Intaglietta, "Oxygen gradients in the microcirculation," *Physiological Reviews*, vol. 83, no. 3, pp. 933–963, 2003.

[43] M. L. Ellsworth and R. N. Pittman, "Evaluation of photometric methods for quantifying convective mass transport in microvessels," *American Journal of Physiology-Heart and Circulatory Physiology*, vol. 251, no. 4, pp. H869–H879, 1986.

[44] H. Carvalho and R. N. Pittman, "Longitudinal and radial gradients of PO_2 in the hamster cheek pouch microcirculation," *Microcirculation*, vol. 15, no. 3, pp. 215–224, 2008.

[45] W. D. McElroy, "The energy source for bioluminescence in an isolated system," *Proceedings of the National Academy of Sciences*, vol. 33, no. 11, pp. 342–345, 1947.

[46] B. L. Strehler and W. McElroy, "[122] assay of adenosine triphosphate," *Methods in Enzymology*, vol. 3, pp. 871–873, 1957.

[47] P. Holton, "The liberation of adenosine triphosphate on antidromic stimulation of sensory nerves," *The Journal of Physiology*, vol. 145, no. 3, pp. 494–504, 1959.

[48] T. Forrester and A. Lind, "Identification of adenosine triphosphate in human plasma and the concentration in the venous effluent of forearm muscles before, during and after sustained contractions," *The Journal of Physiology*, vol. 204, no. 2, pp. 347–364, 1969.

[49] J. L. Gordon, "Extracellular ATP: effects, sources and fate.," *Biochemical Journal*, vol. 233, no. 2, p. 309, 1986.

[50] W. T. McCullough, D. M. Collins, and M. L. Ellsworth, "Arteriolar responses to extracellular ATP in striated muscle," *American Journal of Physiology-Heart and Circulatory Physiology*, vol. 272, no. 4, pp. H1886–H1891, 1997.

[51] L. Needham, N. J. Cusack, J. D. Pearson, and J. L. Gordon, "Characteristics of the P2 purinoceptor that mediates prostacyclin production by pig aortic endothelial cells," *European Journal of Pharmacology*, vol. 134, no. 2, pp. 199–209, 1987.

[52] A. Rubino, V. Ralevic, and G. Burnstock, "Contribution of P1 (A2b subtype) and P2-purinoceptors to the control of vascular tone in the rat isolated mesenteric arterial bed," *British Journal of Pharmacology*, vol. 115, no. 4, pp. 648–652, 1995.

[53] A.-K. Wihlborg, M. Malmsjö, A. Eyjolfsson, R. Gustafsson, K. Jacobson, and D. Erlinge, "Extracellular nucleotides induce vasodilatation in human arteries via prostaglandins, nitric oxide and endothelium-derived hyperpolarising factor," *British Journal of Pharmacology*, vol. 138, no. 8, pp. 1451–1458, 2003.

[54] R. F. Furchgott and J. V. Zawadzki, "The obligatory role of endothelial cells in the relaxation of arterial smooth muscle by acetylcholine," *Nature*, vol. 288, no. 5789, p. 373, 1980.

[55] S. S. Segal and B. R. Duling, "Propagation of vasodilation in resistance vessels of the hamster: development and review of a working hypothesis.," *Circulation Research*, vol. 61, no. 5 Pt 2, pp. II20–5, 1987.

[56] S. S. Segal and B. R. Duling, "Conduction of vasomotor responses in arterioles: a role for cell-to-cell coupling?," *American Journal of Physiology-Heart and Circulatory Physiology*, vol. 256, no. 3, pp. H838–H845, 1989.

[57] S. S. Segal, D. N. Damon, and B. R. Duling, "Propagation of vasomotor responses coordinates arteriolar resistances," *American Journal of Physiology-Heart and Circulatory Physiology*, vol. 256, no. 3, pp. H832–H837, 1989.

[58] W. B. Campbell, D. Gebremedhin, P. F. Pratt, and D. R. Harder, "Identification of epoxyeicosatrienoic acids as endothelium-derived hyperpolarizing factors," *Circulation Research*, vol. 78, no. 3, pp. 415–423, 1996.

[59] M. Fukao, H. S. Mason, J. L. Kenyon, B. Horowitz, and K. D. Keef, "Regulation of BKCa channels expressed in human embryonic kidney 293 cells by epoxyeicosatrienoic acid," *Molecular Pharmacology*, vol. 59, no. 1, pp. 16–23, 2001.

[60] J. E. Jagger, R. M. Bateman, M. L. Ellsworth, and C. G. Ellis, "Role of erythrocyte in regulating local O2 delivery mediated by hemoglobin oxygenation," *American Journal of Physiology-Heart and Circulatory Physiology*, vol. 280, no. 6, pp. H2833–H2839, 2001.

[61] R. C. Roach, M. D. Koskolou, J. A. Calbet, and B. Saltin, "Arterial O2 content and tension in regulation of cardiac output and leg blood flow during exercise in humans," *American Journal of Physiology-Heart and Circulatory Physiology*, vol. 276, no. 2, pp. H438–H445, 1999.

[62] J. González-Alonso, D. B. Olsen, and B. Saltin, "Erythrocyte and the regulation of human skeletal muscle blood flow and oxygen delivery," *Circulation Research*, vol. 91, no. 11, pp. 1046–1055, 2002.

[63] J. González-Alonso, S. P. Mortensen, E. A. Dawson, N. H. Secher, and R. Damsgaard, "Erythrocytes and the regulation of human skeletal muscle blood flow and oxygen delivery: role of erythrocyte count and oxygenation state of haemoglobin," *The Journal of Physiology*, vol. 572, no. 1, pp. 295–305, 2006.

[64] N. W. Ghonaim, L. W. Lau, D. Goldman, C. G. Ellis, and J. Yang, "A micro-delivery approach for studying microvascular responses to localized oxygen delivery," *Microcirculation*, vol. 18, no. 8, pp. 646–654, 2011.

[65] M. S. Hanson, M. L. Ellsworth, D. Achilleus, A. H. Stephenson, E. A. Bowles, M. Sridharan, S. Adderley, and R. S. Sprague, "Insulin inhibits low oxygen-induced atp release from human erythrocytes: Implication for vascular control," *Microcirculation*, vol. 16, no. 5, pp. 424–433, 2009.

[66] C. G. Ellis, D. Goldman, M. Hanson, A. H. Stephenson, S. Milkovich, A. Benlamri, M. L. Ellsworth, and R. S. Sprague, "Defects in oxygen supply to skeletal muscle of pre-diabetic ZDF rats," *American Journal of Physiology-Heart and Circulatory Physiology*, vol. 298, no. 6, pp. H1661–H1670, 2010.

[67] R. S. Sprague, A. H. Stephenson, E. A. Bowles, M. S. Stumpf, and A. J. Lonigro, "Reduced expression of Gi in erythrocytes of humans with type 2 diabetes is associated with impairment of both cAMP generation and ATP release," *Diabetes*, vol. 55, no. 12, pp. 3588–3593, 2006.

[68] R. M. Bateman, M. D. Sharpe, J. E. Jagger, and C. G. Ellis, "Sepsis impairs microvascular autoregulation and delays capillary response within hypoxic capillaries," *Critical Care*, vol. 19, no. 1, p. 389, 2015.

[69] C. G. Ellis, S. Milkovich, and D. Goldman, "What is the efficiency of atp signaling from erythrocytes to regulate distribution of o$_2$ supply within the microvasculature?," *Microcirculation*, vol. 19, no. 5, pp. 440–450, 2012.

[70] S. Prahl, "Optical absorption of hemoglobin," tech. rep., Oregon Medical Laser Center, 1999.

[71] M. L. Ellsworth, R. N. Pittman, and C. G. Ellis, "Measurement of hemoglobin oxygen saturation in capillaries," *American Journal of Physiology-Heart and Circulatory Physiology*, vol. 252, no. 5, pp. H1031–H1040, 1987.

[72] S. A. Japee, R. N. Pittman, and C. G. Ellis, "A new video image analysis system to study red blood cell dynamics and oxygenation in capillary networks," *Microcirculation*, vol. 12, no. 6, pp. 489–506, 2005.

[73] G. M. Fraser, S. Milkovich, D. Goldman, and C. G. Ellis, "Mapping 3-D functional capillary geometry in rat skeletal muscle in vivo," *American Journal of Physiology-Heart and Circulatory Physiology*, vol. 302, no. 3, pp. H654–H664, 2012.

[74] J. N. Reddy and D. K. Gartling, *The finite element method in heat transfer and fluid dynamics.* CRC Press, 2010.

[75] Y. Saad and M. H. Schultz, "GMRES: A generalized minimal residual algorithm for solving nonsymmetric linear systems," *SIAM Journal on Scientific and Statistical Computing*, vol. 7, no. 3, pp. 856–869, 1986.

[76] J. C. McDonald, D. C. Duffy, J. R. Anderson, D. T. Chiu, and H. Wu, "Fabrication of microfluidic systems in poly(dimethylsiloxane)," *Electrophoresis*, no. 21, pp. 27–40, 2000.

[77] S. C. Terry, J. H. Jerman, and J. B. Angell, "A gas chromatographic air analyzer fabricated on a silicon wafer," *IEEE Transactions on Electron Devices*, vol. 26, no. 12, pp. 1880–1886, 1979.

[78] I. R. Lauks, "Microfabricated biosensors and microanalytical systems for blood analysis," *Accounts of Chemical Research*, vol. 31, pp. 317–324, May 1998.

[79] M. A. Burns, C. H. Mastrangelo, T. S. Sammarco, F. P. Man, J. R. Webster, B. N. Johnsons, B. Foerster, D. Jones, Y. Fields, A. R. Kaiser, and D. T. Burke, "Microfabricated structures for integrated DNA analysis," *Proceedings of the National Academy of Sciences of the United States of America*, vol. 93, pp. 5556–5561, May 1996.

[80] A. van den Berg, A. Grisel, E. Verney-Norberg, B. H. van der Schoot, M. Koudelka-Hep, and N. F. de Rooij, "On-wafer fabricated free-chlorine sensor with ppb detection limit for drinking-water monitoring," *Sensors and Actuators B: Chemical*, vol. 13, no. 1, pp. 396–399, 1993.

[81] J. P. Brody, P. Yager, R. E. Goldstein, and R. H. Austin, "Biotechnology at low Reynolds numbers," *Biophysical Journal*, vol. 71, pp. 3430–3441, Dec. 1996.

[82] J. T. Santini, M. J. Cima, and R. Langer, "A controlled-release microchip," *Nature*, vol. 397, pp. 335–338, Jan. 1999.

[83] A. M. Ghaemmaghami, M. J. Hancock, H. Harrington, H. Kaji, and A. Khademhosseini, "Biomimetic tissues on a chip for drug discovery," *Drug Discovery Today*, vol. 17, pp. 173–181, Feb. 2012.

[84] D. C. Duffy, J. C. McDonald, O. J. A. Schueller, and G. M. Whitesides, "Rapid prototyping of microfluidic systems in poly(dimethylsiloxane)," *Analytical Chemistry*, vol. 70, pp. 4974–4984, Oct. 1998.

[85] G. T. Kovacs *et al.*, *Micromachined transducers sourcebook*. WCB/McGraw-Hill New York, 1998.

[86] H.-P. Saluz, M. Köhler, and T. Mejevaia, *Microsystem technology: a powerful tool for biomolecular studies*. Birkhäuser, 2012.

[87] X. Mu, Q. Liang, P. Hu, K. Ren, Y. Wang, and G. Luo, "Laminar flow used as liquid etch mask in wet chemical etching to generate glass microstructures with an improved aspect ratio," *Lab on a Chip*, vol. 9, no. 14, pp. 1994–1996, 2009.

[88] M. J. Madou, *Fundamentals of microfabrication: the science of miniaturization*. CRC press, 2002.

[89] R. J. Jackman, T. M. Floyd, R. Ghodssi, M. A. Schmidt, and K. F. Jensen, "Microfluidic systems with on-line UV detection fabricated in photodefinable epoxy," *Journal of Micromechanics and Microengineering*, vol. 11, no. 3, p. 263, 2001.

[90] K. Ren, J. Zhou, and H. Wu, "Materials for microfluidic chip fabrication," *Accounts of Chemical Research*, vol. 46, no. 11, pp. 2396–2406, 2013.

[91] H. Becker and C. Gärtner, "Polymer microfabrication technologies for microfluidic systems," *Analytical and Bioanalytical Chemistry*, vol. 390, no. 1, pp. 89–111, 2008.

[92] R. Mukhopadhyay, "When PDMS isn't the best," 2007.

[93] J. S. Go and S. Shoji, "A disposable, dead volume-free and leak-free in-plane PDMS microvalve," *Sensors and Actuators A: Physical*, vol. 114, no. 2, pp. 438–444, 2004.

[94] Y. Temiz, R. D. Lovchik, G. V. Kaigala, and E. Delamarche, "Lab-on-a-chip devices: How to close and plug the lab?," *Microelectronic Engineering*, vol. 132, pp. 156–175, 2015.

[95] M. A. Eddings, M. A. Johnson, and B. K. Gale, "Determining the optimal PDMS–PDMS bonding technique for microfluidic devices," *Journal of Micromechanics and Microengineering*, vol. 18, no. 6, p. 067001, 2008.

[96] M. A. Unger, H.-P. Chou, T. Thorsen, A. Scherer, and S. R. Quake, "Monolithic microfabricated valves and pumps by multilayer soft lithography," *Science*, vol. 288, no. 5463, pp. 113–116, 2000.

[97] K. Haubert, T. Drier, and D. Beebe, "PDMS bonding by means of a portable, low-cost corona system," *Lab on a Chip*, vol. 6, no. 12, pp. 1548–1549, 2006.

Chapter 2

Localized oxygen exchange platform for intravital video microscopy investigations of microvascular oxygen regulation

2.1   Introduction

Oxygen (O_2) regulation is a critical physiological function where precise regulatory control is required to ensure the metabolic demands of the tissues of the body are met. In order for such a level of control to be possible, there must be various mechanisms in place to sense O_2 demand and correspondingly adjust O_2 supply.

Numerous studies have confirmed that the presence/absence of O_2 in the microcirculation results in a vasoactive response such that high levels of O_2 result in vasoconstriction [1–5] and low levels of O_2 result in vasodilation [6–8]. These findings allude to the existence of an O_2 sensor, the location of which remains unclear [9]. Potential locations include the red blood cell (RBC), arteriolar smooth muscle, arteriolar endothelium and even extra-vascular cells; see [9] for an in-depth review.

There has been substantial evidence pointing to the RBC as the sensor for O_2 in the microcirculation; see review by Ellsworth *et al.* [10]. One potential mechanism that has been proposed is the O_2-dependent release of ATP from RBCs. In this mechanism, ATP is released from RBCs in response to decreased oxygen tension leading to increased plasma ATP [11, 12]. The intra-luminal ATP then binds to P_{2Y2} receptors on the blood vessel endothelium triggering an upstream vasodilatory response [13–16]. Several pathological conditions have been associated with an impaired ability to release ATP, such as sepsis [17] and type II diabetes [18–20], potentially affecting the ability to regulate oxygen.

Various studies have used microscopy in conjunction with methods to alter the tissue oxygenation to interrogate the regulatory system [4, 5, 8]. For instance, suffusion solutions with varying levels of O_2 have been used to control O_2 in several tissue preparations to study the regulatory response [5, 8]. In previous studies, we used intravital video microscopy that combines a gas exchange platform with computer controlled gas flow meters to manipulate the gas composition at the surface of rat *extensor digitorum longus* (EDL) muscle to study the response of the microcirculation to a range of O_2 concentrations [21–23]. In these studies, the entire surface of the muscle was affected by the change in O_2. While these approaches were able to elicit vasodilatory responses, more localized changes in O_2 could potentially reveal information leading to the location of the O_2 sensor.

More recently, a localized micro-delivery system was developed that was capable of limiting the change in RBC oxygen saturation (SO_2) to a circular area of approximately 175 µm in diameter [24], however, changes in supply rate were not reported [24]. This finding was supported by a mathematical model of the regulatory system that suggests that the signal for vasodilation is additive and depends on the number of capillaries that are stimulated [25]. A later study used a larger exchange window (1 mm long by 0.1 mm wide) to manipulate the RBC SO_2 of a much larger area; this larger exchange window elicited a flow response [26]. This work further supports the idea that the vasodilatory signal is additive.

The work in Ghonaim *et al.* [26] showed promising results which were consistent with the proposed ATP release mechanism, however, there were some limitations for studying O_2 regulatory mechanisms. First, stimulating multiple microvascular units at the same time potentially affects multiple feeding arterioles. Additionally, the setup in Ghonaim *et al.* could only resolve capillaries that were less than 60 µm from the surface; one challenge associated with using gas exchange chambers with intravital microscopy is that the chamber must be placed in between the objective and the muscle, reducing the effective focal depth. This impedes the ability to focus on structures deeper in the tissue.

This study presents a refined gas exchange design that is modular and capable of changing local tissue O_2 tension in small regions affecting single microvascular units. One potential benefit of such a device is to determine if stimulation of a single microvascular unit is sufficient to elicit a flow response. By making the design modular, the device can be easily adjusted to suit different needs. For example, the shape and size of the exchange surfaces can easily be changed. This design also aims to maximize the focal plane in order to view structures deeper in the tissue as well as allowing for viewing of adjacent regions in the tissue. In addition, we used a GPU accelerated computational model of oxygen transport to estimate O_2 content in the tissue and the temporal affects of changing O_2 in the chamber. Overall, we developed a modular gas exchange device for studying oxygen regulation in the microcirculation.

2.2   Methods

2.2.1   Gas Chamber Design and Fabrication

The gas exchange chamber was comprised of a microscope stage insert, a gasket to form the side walls of the channel and a platform for the inlet and outlet of the channel (see Figure

6.1). The bottom of the channel was closed by a replaceable glass slide. The top of the channel was closed by a custom, laser-cut glass slide with five windows for gas exchange using a process described in [27]; the windows were sealed with a thin, gas-permeable, membrane. The components were assembled together using vacuum grease to ensure no gas leakage.
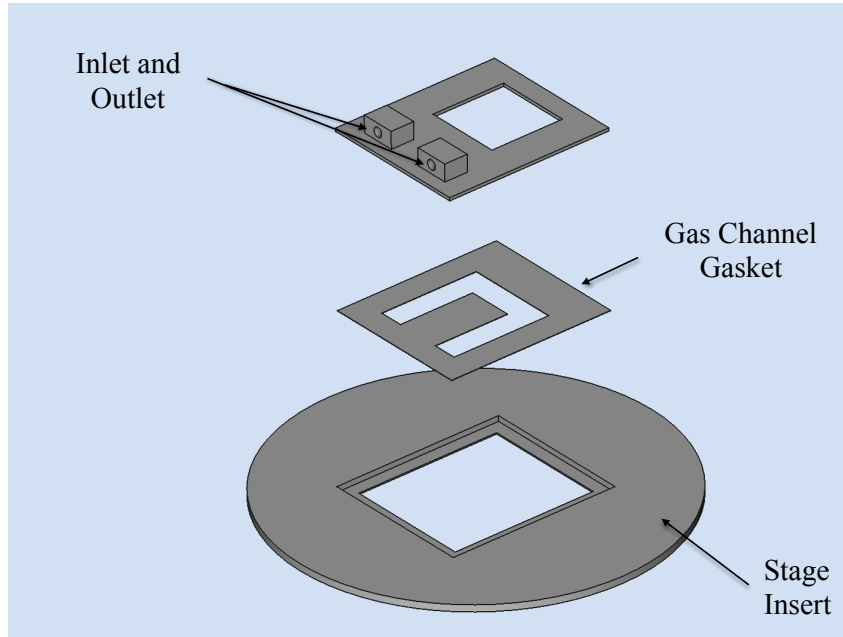
Figure 2.1: *Three dimensional CAD model of gas chamber components. Inlet/outlet mount and stage insert were 3D printed. The gas channel gasket was made out polymethyl-methacrylate (PMMA). The gas channel is sealed on the bottom with a glass cover slide and on the top with a laser-cut glass cover slide.*

The stage insert and platform for the inlet and outlet were designed in FreeCAD and 3D printed. The gasket was fabricated by hand cutting 100-µm sheets of polymethyl-methacrylate (PMMA) to the desired shape. The gas-permeable membrane was fabricated in PDMS using a spin-coating technique similar to [28]. PDMS (Sylgard 184, Dow Corning Corporation) in a 10:1 prepolymer to cross-linker ratio by weight was spin-coated at 1700 rpm for 30 seconds; resulting membranes were approximately 45 µm in thickness.

Gas composition (O_2, CO_2 and N_2) was controlled using computer controlled mass flow meters. Gas temperature was maintained at 37 °C.

2.2.2 Animal Preparation

Male Sprague-Dawley (150-200g) rats were anesthetized with 65 mg per kg of body weight of pentobarbital sodium by intraperitonial injection. Following injection, the animals were tracheotomized for ventilation as previously described [20, 29]. Animals were mechanically ventilated with 30% oxygen and balance nitrogen while their inspired O_2, heart rate, and blood pressure levels were continuously recorded as described in [20]. The *Extensor digitorum longus* (EDL) muscle of the hind limb was prepared for microscopy as described in [30]; this preparation was based on that by Tyml and Budreau [31]. The muscle was extended on the microscope stage using suture attached to the edge of the muscle. The muscle was then covered with oxygen-impermeable Saran Wrap and a glass cover slip to isolate it from the room oxygen conditions. The tissue was trans-illuminated with a 75 W xenon lamp (Olympus U-LH75XEAPO) using an Olympus IX-81 inverted microscope equipped with 10X (Olympus U Plan S-APO; 0.4 NA) and 20X (Olympus U Plan LWD; 0.45 NA) objectives. The corresponding images were captured using the dual video camera system previously described in [20]. The experiments used in this study were approved by the University of Western Ontario's Animal Care and Use Committee (see Appendix A).

2.2.3 Data Analysis

Intravital video microscopy images were acquired at 21 frames per second at two wavelengths, 438 nm and 450 nm using a beam splitter. Images were analyzed offline using software developed in MATLAB (Mathworks) to quantify SO_2 and hemodynamics as previously described [30, 32–34].

2.2.4 Mathematical Model of Tissue Oxygenation

A mathematical model of tissue oxygenation is used to determine the extent of oxygen diffusion in the tissue from the gas exchange chamber. Tissue oxygenation was simulated in
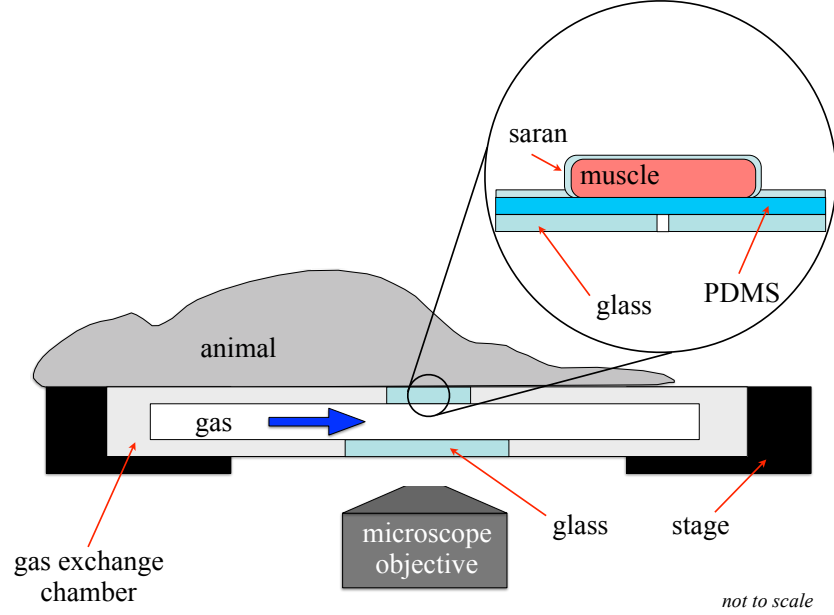
Figure 2.2: *Intravital video microscopy experimental setup. This figure shows the experimental setup for an intravital experiment to allow for oxygen exchange to a localized area of tissue. In this setup, the muscle is extended over the gas exchange window and covered in gas-impermeable saran wrap to isolate the muscle from the surrounding environment.*

3D over time. Tissue oxygen partial pressure, PO$_2$, was determined by numerically solving:

$$k\frac{\partial P}{\partial t} = Dk\nabla^2 P + Kk\left(1 - \frac{P}{P_0}\right) - M_0\frac{P}{P + P_{crit}}$$

where D and k are oxygen diffusivity and solubility in tissue, respectively, M_0 is the maximal tissue oxygen consumption, P_{crit} is the PO$_2$ at which consumption is half VO_2, P_0 is the average capillary PO$_2$ and K is the rate of oxygen transport from the capillaries into the tissue. The parameters used in our model are summarized in Table 4.1.

This model assumes the tissue is homogeneously consuming oxygen and that there is a homogeneous supply of oxygen from the capillaries. Similar models were implemented in previous studies to predict tissue oxygenation [24, 38].

The temporal derivative was discretized using an implicit-explicit method similar to [40]

Table 2.1: *Parameters used in mathematical model.*

Parameter	Value	Reference
D	2.41×10^{-5} cm^2/s	Bentley *et al.* [35]
k	3.89×10^{-5} mL O$_2$/mL/mmHg	Mahler *et al.* [36]
M_0	1.57×10^{-4} mL O$_2$/mL/s	Sullivan & Pittman [37]
K	30 mmHg	Goldman [38]
P_0	48 mmHg	Goldman [38]
P_{crit}	0.5 mmHg	Honig & Gayeski [39]

and the spatial derivatives were discretized using a second order central difference scheme. In this scheme, the linear source term was evaluated at the current time step, where as the other terms were evaluated at the previous time step. This scheme was chosen since it is fully explicit and has greater stability than the forward Euler scheme. The numerical solution was parallelized on a graphical processing unit (GPU) and implemented in C++/CUDA. The numerical grid was spatially decomposed onto a 1024-core GPU. A four-minute simulation with one million spatial nodes was solved in under five minutes. Computation time is limited by the solution write-out frequency.

2.3 Results

Five gas exchange windows were patterned into glass slides to facilitate positioning of the muscle relative to the exchange window (Figure 2.3). Windows were designed to be 200 by 400 µm. The spacing of the windows was chosen to allow for regions between the windows that are unaffected by the change in O$_2$. This was verified with our mathematical model; see Figure 2.4. Dark markings can been seen around the edges of the windows; this is due to the laser fabrication process. It can be noted that these marks only appear on one side of the glass slide. We chose the non-marked side to be in contact with the muscle to ensure that the markings are out of the focal plane when focused on the muscle; this can be seen in Figure 2.3 panel C.

We used a model of O$_2$ transport that was modified from that used in [24, 38] to predict the
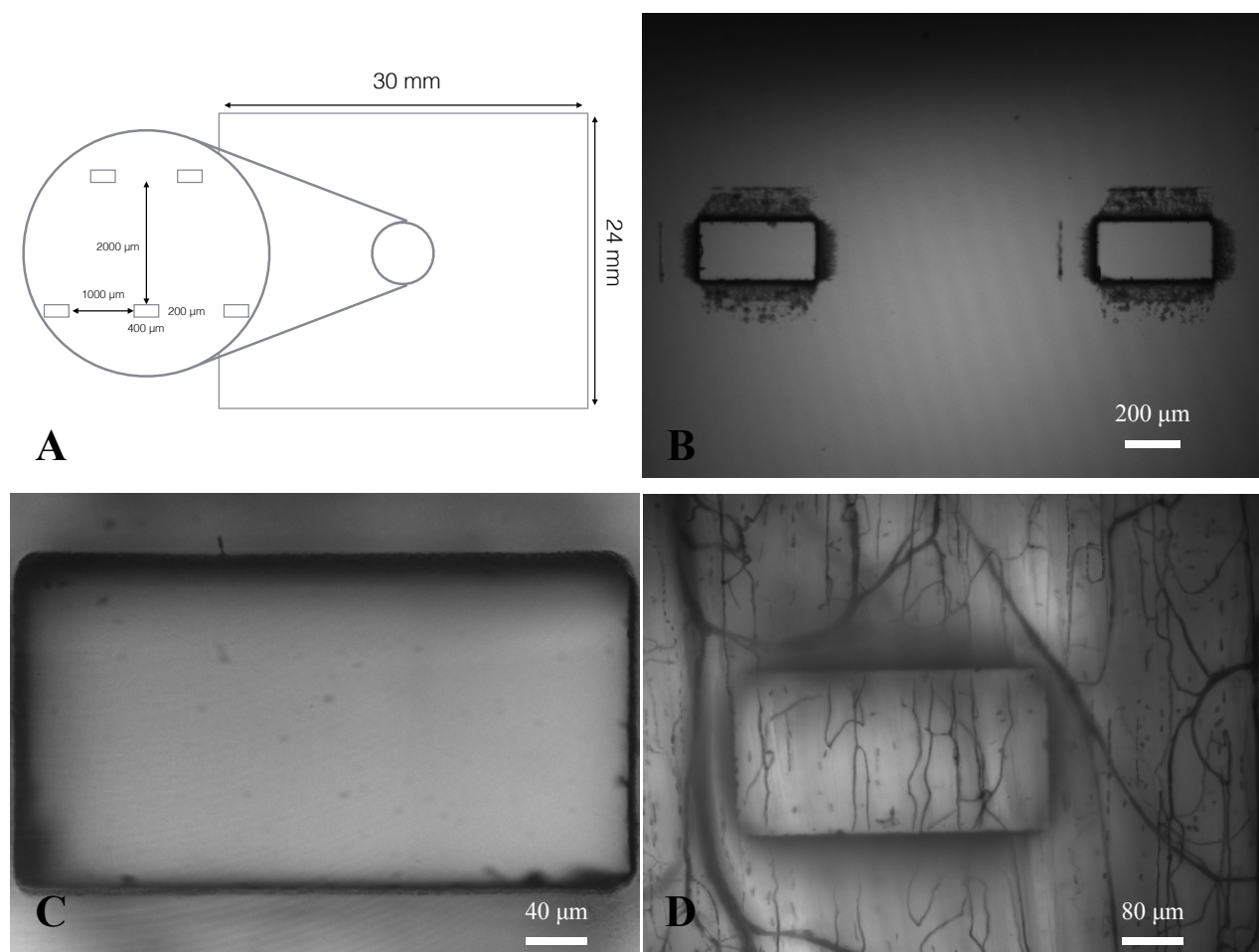
Figure 2.3: *Gas exchange window design. Panel A shows a diagram of the design of the gas exchange windows. Panel B shows a 4X micrograph of the two of the exchange windows cantered in the field of view. Dark markings can be seen around the edges of the window. Panel C shows a 20X micrograph of an exchange window focused on the edge closest to the objective. Panel D shows a 10X functional image of the minimum intensity values over time.*

distribution of O_2 in the tissue. This model only considers diffusion, neglecting convective effects caused by RBCs transporting O_2. The model suggests that only a small area will be affected by the window (Figure 2.5).
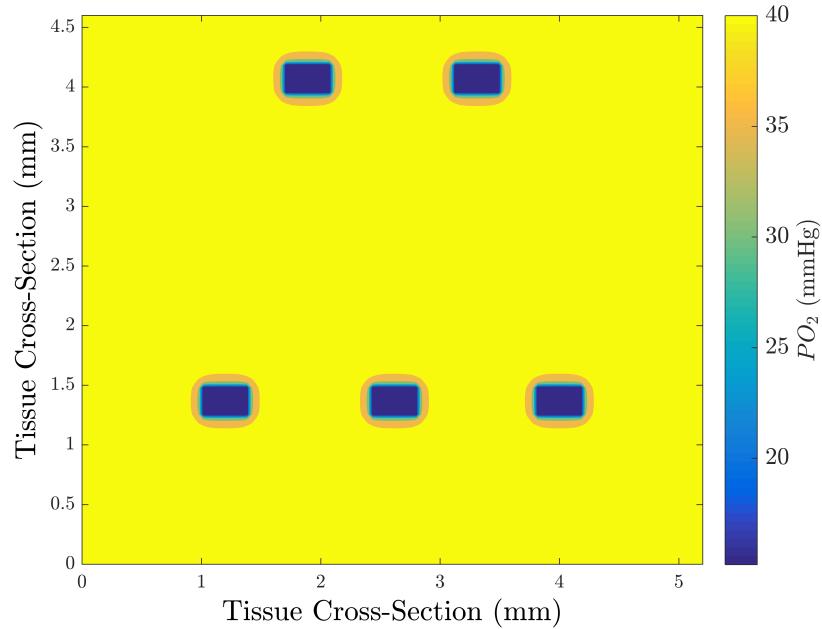
Figure 2.4: *Computational simulation predicting the extent of diffusion between the five windows. Contour map of the steady-state O_2 distribution in the tissue around the gas exchange windows. The displayed plane is oriented with the imaging plane of the microscope and at a depth of 25 μm into the tissue from the surface of the glass slide.*

To verify that the exchange window is affecting RBC SO_2, we performed step changes in gas O_2 and measured the resulting RBC SO_2. At baseline, the gas composition contained 5% O_2, 5% CO_2, and balance N_2. After one minute, the gas composition was changed to 2 % O_2, 5% CO_2 and balance N_2. An example of a step change for various capillaries in the field of view is shown in Figure 2.6. After the drop in gas chamber O_2, the SO_2 drops rapidly then steadily increases. This increase may be explained by the increased flow rate in response to the low O_2. It can also be noted that the trend is similar for all capillaries in the field of view.

A further demonstration of the desaturation capabilities of this device are shown in Figure 2.7. This figure shows the distribution of capillary SO_2 values when the window O_2 is set
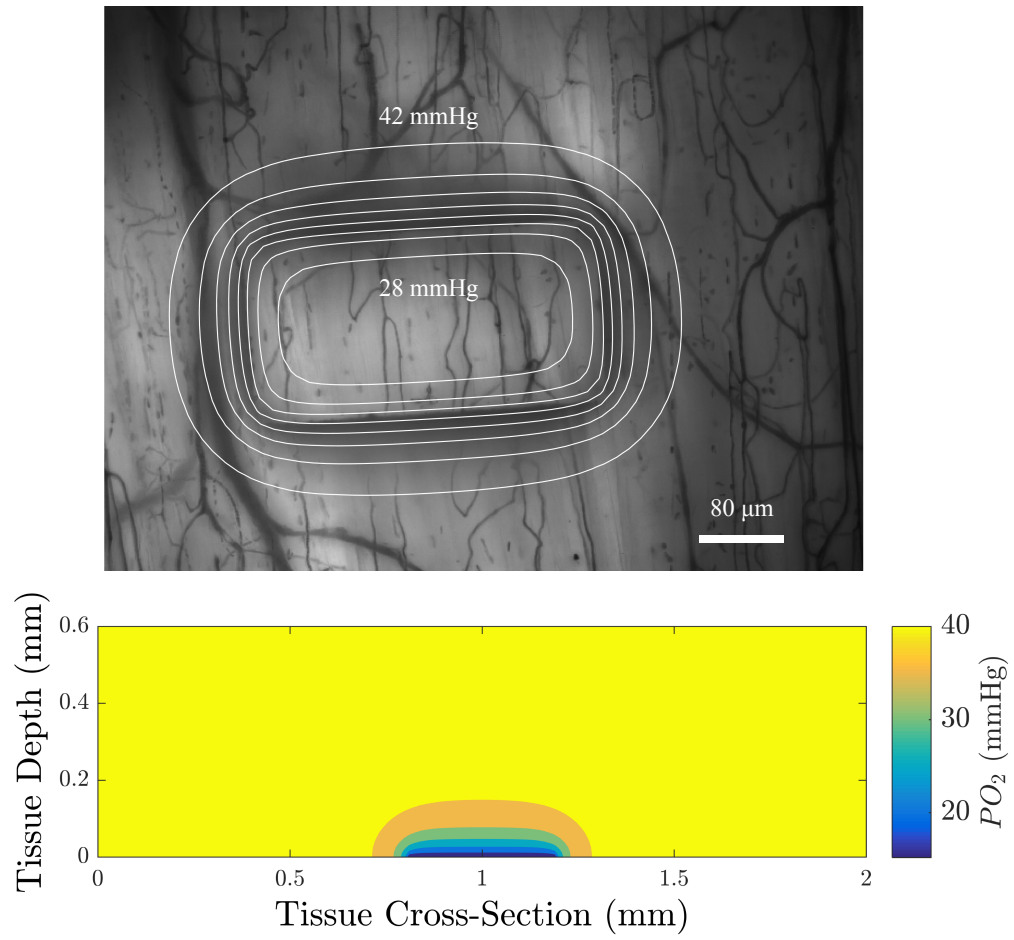
Figure 2.5: *Predicted oxygen distribution. The top pannel shows an intravital video minimum intensity functional image with contour lines displaying constant oxygen; each line is 2 mmHg apart. The model assumes the plane is 25 μm from the surface of the window. The bottom panel shows a colormap of the oxygen distribution as a function of depth in the tissue.*
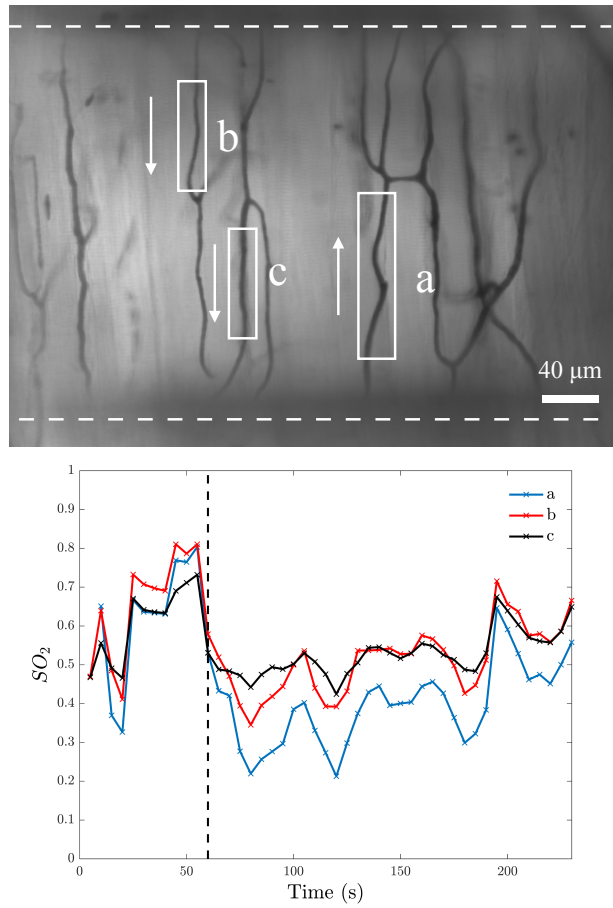
Figure 2.6: *Capillary SO_2 in response to a step change in O_2. The top panel shows the minimum intensity function image of the field of view. The capillaries analyzed are identified by white boxes, with arrows to indicate the direction of RBC flow, and the white dashed line indicates the position of the exchange window. The bottom panel shows RBC SO_2 as a function of time; the time at which O_2 was changed is indicated with the black dashed line.*

to 2%, 5% and 7% (5% CO_2 and balance N_2). These results demonstrate the large varia-
tions in RBC SO_2 experienced in the microcirculation, even when subjected to variations in
window O_2. The variations are probably due to the variability in RBC supply rate between
vessels, which vary from approximately 2 RBC/s to 40 RBC/s in this field of view.
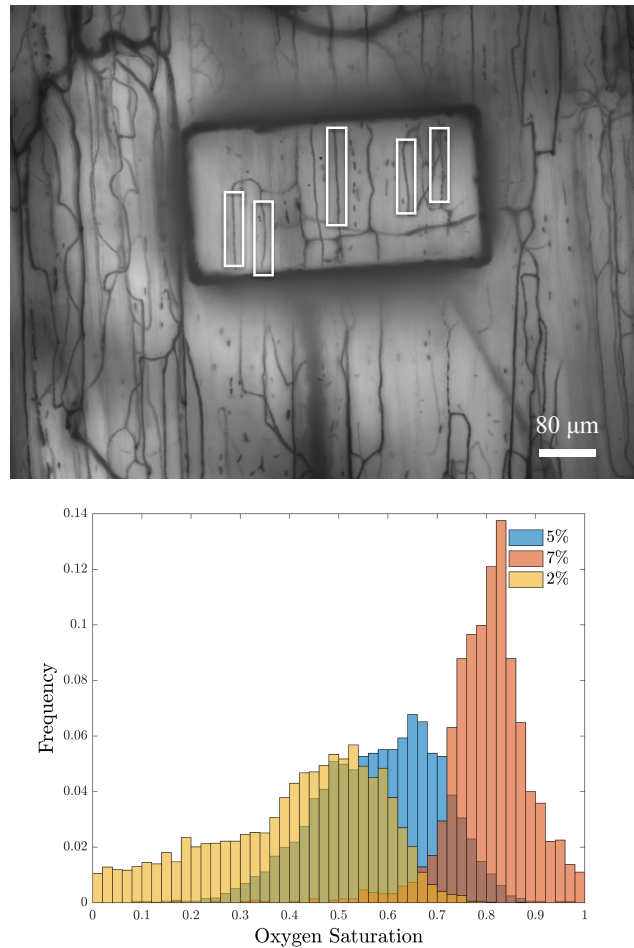
Figure 2.7: *Distribution of RBC SO_2 in response to three window O_2 levels (2%, 5% and 7%). The
top panels shows the minimum intensity functional image of the analyzed field of view; the analyzed
capillaries are indicated with white boxes. The bottom panel shows the distribution of the average
capillary SO_2 binned into 1 second intervals for window O_2 of 2% (orange), 5% (blue) and 7% (red).
Histogram bins are partially transparent to show the overlap.*

The computational model was also used to verify how quickly changes in chamber O_2 affect
tissue O_2 at varying depths in the tissue. The model assumes the gas composition at the
window changes instantly; thus the model is determining the temporal diffusion limitation.

Figure 2.8 A shows the simulation results for a step change in O_2 from 5% to 2% centred in the window at varying tissue depths. The results of a square wave in O_2 are shown in panel B. The simulation demonstrates that diffusion reaches steady-state within 3 seconds of the the step change. The delay in the change in chamber O_2 was measured experimentally using a PO_2 sensor in the outlet of the gas channel; typical delays are on the order of 2 seconds. Thus, we expect a total delay of 5 seconds.
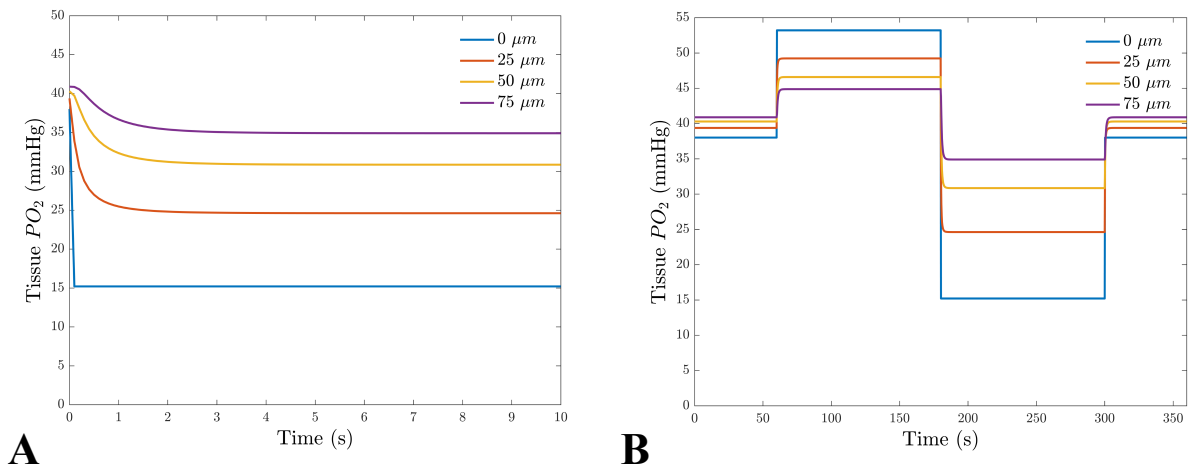
Figure 2.8: *Predicted time-dependent changes in tissue O_2. Panel A shows predicted tissue O_2 for a step change in chamber O_2 for different depths in the tissue. Panel B shows the predicted tissue O_2 in response to a square wave in chamber O_2 (one minute of 5% O_2, two minutes of 7% O_2, two minutes of 2% O_2 and one minute of 5% O_2).*

To demonstrate that the device can induce flow rate responses, we measured both RBC SO_2 in selected in-focus capillaries as well as RBC supply rate in response to a square wave change in chamber O_2. The square wave consisted of one minute of 5% O_2 followed by two minutes of 7% percent, two minutes of 2% percent and one minute of 5% with 3% and balance N_2. The analyzed field of view and results of the square wave are shown in Figure 2.9.
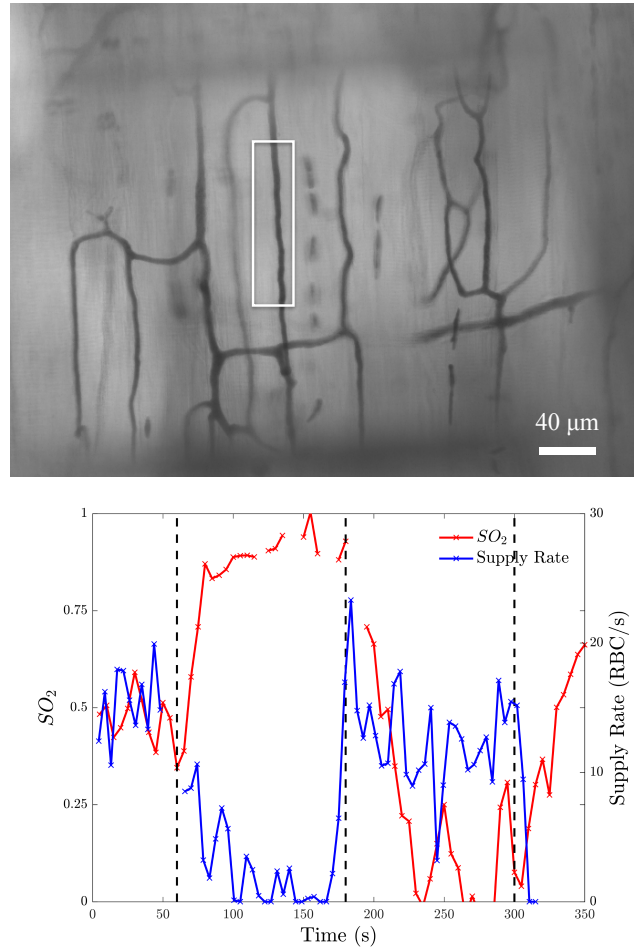
Figure 2.9: *Oxygen saturation and supply rate change in response to square wave oxygen challenge. The top panel shows the minimum intensity function image of the analyzed field of view at 20X magnification. The analyzed capillary is indicated with a white box. The bottom panel shows the induced SO_2 changes along with the corresponding change in RBC supply rate. The black dashed lines indicate the time at which the chamber O_2 was changed.*

2.4   Discussion

In this study, we developed a modular gas exchange platform to deliver a localized gas composition to the surface of tissue for use in intravital microscopy studies. Our platform is able to change RBC SO_2 to capillaries within a localized area of approximately 560 by 360 µm (Figure 2.5). The changes in capillary RBC O_2 were demonstrated both experimentally (Figures 2.6, 2.7) and computationally (Figure 2.5); the later was able to predict the extent of the affected area. This gas exchange platform is able to induce both increased and decreased microvascular flow response to changing levels of O_2. The computational

model predicts that O_2 diffusion into the tissue will reach steady-state within 5 seconds of changing the chamber O_2. This prediction may be impacted by the presence of blood vessels, for which the model does not account.

In previous work, we used a smaller gas exchange window to induce RBC SO_2 changes [24]. Ghonaim *et al.* suggested that not enough capillaries were stimulated to elicit a flow response [25, 26]. This is supported by the use of a larger gas exchange window to induce RBC SO_2 changes in more capillaries to which the vasculature responded [26]. In the current study, we used a window size that was larger than that used in [24] but smaller than that used in [26] and were able to get consistent vascular response with our chamber. The changes in SO_2 in both [24, 26] were consistent with those in our chamber. This finding supports the hypothesis that the ATP release signal is additive since we are affecting more capillaries than in [24].

Various studies in the literature have been successful in causing changes in RBC SO_2 both *in vivo* and *ex vivo* [1–8]. One approach is to alter the inspired O_2 levels as in [3], resulting in changed RBC SO_2, though this may result in systemic hyper/hypoxia [9]. Another approach involves using superfusion solutions with different gas compositions to bathe the tissue in order to control the surface O_2 levels [5, 8]. While this method confines the changes in O_2 to the tissue being studied, the changes affect the entire muscle surface. Additionally, these methods may affect the physiological pathways as molecules may be continuously washed away with the superfusate. Superfusion solutions are likely to cause confounding results and make isolating specific vessels challenging since they may be affecting mechanisms at difference levels of the vasculature [9]. Further, due to the low solubility of O_2 in water, superfusion solutions have a limited in their ability carry O_2. For these reasons, gas exchange chambers may be more advantageous than superfusion solutions in the investigations of localized O_2 regulation.

Despite the many benefits of the approach employed in this work, there are a few challenges that are worth noting. Firstly, due to the opening in the glass, the tissue view through the window is on a different focal plane than the surrounding tissue at the same tissue depth. Because of this, it is not possible to focus on capillaries in and out of the window at the same tissue depth simultaneously. However, due to the optical clarity outside the window, we are able to focus on capillaries outside of the window, enabling us to look at the effects of changing gas composition on the surroundings.

Another challenge associated with this experiment is placement of the muscle over the exchange windows. This requires careful manipulation of the muscle in order to place the muscle over the windows such that the window would be affecting the capillary bundle of interest. It seems that moving the muscle multiple time may increase the likeliness that the muscle become stressed and stops responding to changes in O_2. Including more windows closer together would increase the probability of one of the windows being over an interesting area in the muscle, though care must be taken to ensure that the other windows do not affect vessels that come into the area of interest.

In the current study, the longer side of the window was placed perpendicular to capillaries, though it is just as easy to rotate the windows ninety degrees such that the long direction is oriented with the capillaries. This allows for stimulation of the capillaries along their length without crossing over too many networks.

It would be interesting to determine if changes in capillary RBC distribution are due to simple rheology (i.e. bifurcation law) or if there are other active mechanisms in place, such as pericytes to control flow in capillaries. One interesting application of this platform would be to position the window over multiple capillaries fed from the same arteriole to determine if their distribution of flow rates remains constant in response to oxygen; this should be the case if flow is dictated by simple rheology since capillaries cannot change their diameter.

This device is well-suited to studying oxygen regulation at the microvascular level. For instance, this platform could be used to determine if stimulating capillaries in one bundle affects all bundles connected to the same feed arteriole. Such an experiment could help support the SO_2-dependent ATP release from RBC hypothesis. Conversely, if the O_2 sensor is located in the extravascular space rather than the RBCs, the O_2 exchange platform could further be used to stimulate areas of the muscle that lack capillaries to investigate the presence of an RBC sensor.

Additionally, this approach could be used in *ex vivo* and *in vitro* studies where the control of gas composition needs to be locally confined. For example, this gas exchange platform could be used in conjunction with a microfluidic device to desaturate flowing RBCs as suggested in [41, 42]. As proposed in these studies, such a device could probe the dynamics of the ATP release mechanism if it is indeed caused by RBC desaturation.

In summary, we have developed a gas exchange platform capable of causing local changes in RBC SO_2. We have also shown that these changes are consistent with the ATP release hypothesis that multiple capillaries need to be stimulated in order to elicit a microvascular flow rate response. While our device stimulates a large enough region to obtain a flow response, it is also localized enough that we will be able to probe individual parts of the microvascular bed, and it is optically clear enough that we can observe the response both in the stimulated, as well as neighbouring regions. This tool offers exciting possibilities to study microvascular regulation, and may be able to definitively determine the location of the elusive oxygen sensor.

References

[1] B. R. Duling, "Microvascular responses to alterations in oxygen tension," *Circulation Research*, vol. 31, no. 4, pp. 481–489, 1972.

[2] P. M. Hutchins, R. F. Bond, and H. D. Green, "Participation of oxygen in the local control of skeletal muscle microvasculature," *Circulation Research*, vol. 34, no. 1, pp. 85–93, 1974.

[3] Y. Zhu, T. Park, and J. M. Gidday, "Mechanisms of hyperoxia-induced reductions in retinal blood flow in newborn pig," *Experimental Eye Research*, vol. 67, no. 3, pp. 357–369, 1998.

[4] D. G. Welsh, W. F. Jackson, and S. S. Segal, "Oxygen induces electromechanical coupling in arteriolar smooth muscle cells: a role for L-type Ca^{2+} channels," *American Journal of Physiology-Heart and Circulatory Physiology*, vol. 274, no. 6, pp. H2018–H2024, 1998.

[5] J. C. Frisbee and J. H. Lombard, "Parenchymal tissue cytochrome P450 4A enzymes contribute to oxygen-induced alterations in skeletal muscle arteriolar tone," *Microvascular Research*, vol. 63, no. 3, pp. 340–343, 2002.

[6] R. N. Pittman and B. R. Duling, "Oxygen sensitivity of vascular smooth muscle: I. in vitro studies," *Microvascular Research*, vol. 6, no. 2, pp. 202–211, 1973.

[7] K. Fredricks, Y. Liu, and J. H. Lombard, "Response of extraparenchymal resistance arteries of rat skeletal muscle to reduced PO_2," *American Journal of Physiology-Heart and Circulatory Physiology*, vol. 267, no. 2, pp. H706–H715, 1994.

[8] J. C. Frisbee, K. G. Maier, J. R. Falck, R. J. Roman, and J. H. Lombard, "Integration of hypoxic dilation signaling pathways for skeletal muscle resistance arteries," *American Journal of Physiology-Regulatory, Integrative and Comparative Physiology*, vol. 283, no. 2, pp. R309–R319, 2002.

[9] W. F. Jackson, "Arteriolar oxygen reactivity: where is the sensor and what is the mechanism of action?," *The Journal of Physiology*, vol. 594, no. 18, pp. 5055–5077, 2016.

[10] M. L. Ellsworth, C. G. Ellis, D. Goldman, A. H. Stephenson, H. H. Dietrich, and R. S. Sprague, "Erythrocytes: oxygen sensors and modulators of vascular tone," *Physiology*, vol. 24, no. 2, pp. 107–116, 2009.

[11] G. Bergfeld and T. Forrester, "Release of ATP from human erythrocytes in response to a brief period of hypoxia and hypercapnia," *Cardiovascular Research*, vol. 26, no. 1, pp. 40–47, 1992.

[12] M. L. Ellsworth, T. Forrester, C. G. Ellis, and H. H. Dietrich, "The erythrocyte as a regulator of vascular tone," *American Journal of Physiology-Heart and Circulatory Physiology*, vol. 269, no. 6, pp. H2155–H2161, 1995.

[13] R. S. Sprague, M. L. Ellsworth, A. H. Stephenson, and A. J. Lonigro, "ATP: the red blood cell link to no and local control of the pulmonary circulation," *American Journal of Physiology-Heart and Circulatory Physiology*, vol. 271, no. 6, pp. H2717–H2722, 1996.

[14] W. T. McCullough, D. M. Collins, and M. L. Ellsworth, "Arteriolar responses to extracellular ATP in striated muscle," *American Journal of Physiology-Heart and Circulatory Physiology*, vol. 272, no. 4, pp. H1886–H1891, 1997.

[15] D. M. Collins, W. T. McCullough, and M. L. Ellsworth, "Conducted vascular responses: communication across the capillary bed," *Microvascular Research*, vol. 56, no. 1, pp. 43–53, 1998.

[16] H. H. Dietrich, M. L. Ellsworth, R. S. Sprague, and R. G. Dacey Jr, "Red blood cell regulation of microvascular tone through adenosine triphosphate," *American Journal of Physiology-Heart and Circulatory Physiology*, vol. 278, no. 4, pp. H1294–H1298, 2000.

[17] R. M. Bateman, M. D. Sharpe, J. E. Jagger, and C. G. Ellis, "Sepsis impairs microvascular autoregulation and delays capillary response within hypoxic capillaries," *Critical Care*, vol. 19, no. 1, p. 389, 2015.

[18] R. S. Sprague, A. H. Stephenson, E. A. Bowles, M. S. Stumpf, and A. J. Lonigro, "Reduced expression of Gi in erythrocytes of humans with type 2 diabetes is associated with impairment of both cAMP generation and ATP release," *Diabetes*, vol. 55, no. 12, pp. 3588–3593, 2006.

[19] M. S. Hanson, M. L. Ellsworth, D. Achilleus, A. H. Stephenson, E. A. Bowles, M. Sridharan, S. Adderley, and R. S. Sprague, "Insulin inhibits low oxygen-induced atp release from human erythrocytes: Implication for vascular control," *Microcirculation*, vol. 16, no. 5, pp. 424–433, 2009.

[20] C. G. Ellis, D. Goldman, M. Hanson, A. H. Stephenson, S. Milkovich, A. Benlamri, M. L. Ellsworth, and R. S. Sprague, "Defects in oxygen supply to skeletal muscle of prediabetic ZDF rats," *American Journal of Physiology-Heart and Circulatory Physiology*, vol. 298, no. 6, pp. H1661–H1670, 2010.

[21] J. Jagger, S. McCullen, C. Yun, and C. Ellis, "Erythrocyte hemodynamics as a function of the local O_2 environment in the EDL muscle of the rat," in *FASEB Journal*, vol. 18, pp. A632–A632, 2004.

[22] C. Ellis, S. Milkovich, and D. Goldman, "Experimental protocol investigating local regulation of oxygen supply in rat skeletal muscle *in vivo*," in *Journal of Vascular Research*, vol. 43, pp. 45–45, 2006.

[23] S. L. Milkovich, M. MacKie, D. Goldman, and C. G. Ellis, "Local regulation of oxygen supply in rat skeletal muscle in vivo: variations in hemodynamic response," *The FASEB Journal*, vol. 21, no. 5, pp. A481–A481, 2007.

[24] N. W. Ghonaim, L. W. Lau, D. Goldman, C. G. Ellis, and J. Yang, "A micro-delivery approach for studying microvascular responses to localized oxygen delivery," *Microcirculation*, vol. 18, no. 8, pp. 646–654, 2011.

[25] N. W. Ghonaim, G. M. Fraser, C. G. Ellis, J. Yang, and D. Goldman, "Modeling steady state SO_2-dependent changes in capillary ATP concentration using novel O_2 micro-delivery methods," *Frontiers in physiology*, vol. 4, 2013.

[26] N. W. Ghonaim, "Investigating conducted microvascular response to localized oxygen delivery in vivo using a novel micro-delivery approach," 2013.

[27] S. Nikumb, Q. Chen, C. Li, H. Reshef, H. Zheng, H. Qiu, and D. Low, "Precision glass machining, drilling and profile cutting by short pulse lasers," *Thin Solid Films*, vol. 477, no. 1-2, pp. 216–221, 2005.

[28] J. C. McDonald, D. C. Duffy, J. R. Anderson, D. T. Chiu, and H. Wu, "Fabrication of microfluidic systems in poly(dimethylsiloxane)," *Electrophoresis*, no. 21, pp. 27–40, 2000.

[29] C. G. Ellis, M. L. Ellsworth, R. N. Pittman, and W. L. Burgess, "Application of image analysis for evaluation of red blood cell dynamics in capillaries," *Microvascular research*, vol. 44, no. 2, pp. 214–225, 1992.

[30] G. M. Fraser, S. Milkovich, D. Goldman, and C. G. Ellis, "Mapping 3-D functional capillary geometry in rat skeletal muscle in vivo," *American Journal of Physiology-Heart and Circulatory Physiology*, vol. 302, no. 3, pp. H654–H664, 2012.

[31] K. Tyml and C. Budreau, "A new preparation of rat extensor digitorum longus muscle for intravital investigation of the microcirculation.," *International journal of microcirculation, clinical and experimental*, vol. 10, no. 4, pp. 335–343, 1991.

[32] S. A. Japee, C. G. Ellis, and R. N. Pittman, "Flow visualization tools for image analysis of capillary networks," *Microcirculation*, vol. 11, no. 1, pp. 39–54, 2004.

[33] S. A. Japee, R. N. Pittman, and C. G. Ellis, "A new video image analysis system to study red blood cell dynamics and oxygenation in capillary networks," *Microcirculation*, vol. 12, no. 6, pp. 489–506, 2005.

[34] S. A. Japee, R. N. Pittman, and C. G. Ellis, "Automated method for tracking individual red blood cells within capillaries to compute velocity and oxygen saturation," *Microcirculation*, vol. 12, no. 6, pp. 507–515, 2005.

[35] T. B. Bentley, H. Meng, and R. N. Pittman, "Temperature dependence of oxygen diffusion and consumption in mammalian striated muscle," *American Journal of Physiology-Heart and Circulatory Physiology*, vol. 264, no. 6, pp. H1825–H1830, 1993.

[36] M. Mahler, C. Louy, E. Homsher, and A. Peskoff, "Reappraisal of diffusion, solubility, and consumption of oxygen in frog skeletal muscle, with applications to muscle energy balance.," *The Journal of general physiology*, vol. 86, no. 1, pp. 105–134, 1985.

[37] S. M. Sullivan and R. N. Pittman, "*In vitro* O_2 uptake and histochemical fiber type of resting hamster muscles," *Journal of Applied Physiology*, vol. 57, no. 1, pp. 246–253, 1984.

[38] D. Goldman, "A mathematical model of oxygen transport in intact muscle with imposed surface oscillations," *Mathematical biosciences*, vol. 213, no. 1, pp. 18–28, 2008.

[39] C. Honig and T. Gayeski, "Correlation of O$_2$ transport on the micro and macro scale.," *International journal of microcirculation, clinical and experimental*, vol. 1, no. 4, pp. 367–380, 1982.

[40] U. M. Ascher, S. J. Ruuth, and B. T. Wetton, "Implicit-explicit methods for time-dependent partial differential equations," *SIAM Journal on Numerical Analysis*, vol. 32, no. 3, pp. 797–823, 1995.

[41] R. J. Sové, N. Ghonaim, D. Goldman, and C. G. Ellis, "A computational model of a microfluidic device to measure the dynamics of oxygen-dependent ATP release from erythrocytes," *PLOS ONE*, vol. 8, p. e81537, Nov. 2013.

[42] R. J. Sové, G. M. Fraser, D. Goldman, and C. G. Ellis, "Finite element model of oxygen transport for the design of geometrically complex microfluidic devices used in biological studies," *PLOS ONE*, vol. 11, no. 11, p. e0166289, 2016.

Chapter 3

A Computational Model of a Microfluidic Device to Measure the Dynamics of Oxygen-Dependent ATP Release from Erythrocytes[1]

3.1   Introduction

In the human body, the regulation of oxygen transport is an important process to ensure that the demands for oxygen are met. The circulatory system has various mechanisms responsible for the delivery of oxygen to regions of high metabolic activity. Oxygen regulation can occur on a large scale or locally within specific tissue. The vessels responsible for local regulation mechanisms are known to be the small arterioles and capillaries, which comprise the microcirculation.

Erythrocytes have been shown to release ATP in response both to low erythrocyte hemoglobin oxygen saturation (SO_2) [2, 3] and to increased shear stress on the erythrocyte membrane [2, 4]. Both mechanisms are suspected to be involved in the regulation of flow in the microcirculation. In a recent study, the dynamics of shear-dependent release of ATP from erythrocytes was measured by flowing erythrocytes through a constriction in a microfluidic

---

[1]A version of this chapter has been published in PLoS One [1].

device to induce a brief period of increased shear stress [4]. The authors report that the ATP release occurred within 25 to 75 milliseconds after the period of increased shear.

The oxygen-dependent release of ATP is hypothesized to be a mechanism involved in regulating the distribution of oxygen within the microvasculature, where the erythrocyte plays the role of the oxygen sensor [5]. An important aspect of this hypothesis is the time required for ATP release to occur following a change in SO_2, since this determines the spatial accuracy with which the erythrocyte can signal for vasodilation. Our ultimate goal is to measure the dynamics of oxygen-dependent release of ATP by applying a similar approach to the study by Wan *et al.* [4]. In the place of the constriction in the microfluidic device, we will use an oxygen-permeable membrane to cause a rapid change in SO_2 as the erythrocytes flow through the channel.

Understanding this mechanism may also have important clinical implications. In patients with type II diabetes, ATP release is known to be significantly lower for the same change in oxygen saturation [6]. However, we do not know if the time course is also altered in type II diabetes and other cardiovascular diseases [6].

Several concerns must be assessed to design an effective microfluidic device for the study of oxygen-dependent ATP release. First, we must determine whether a practical device can cause a sufficient drop in SO_2 to cause ATP release and whether the change in SO_2 is fast enough to measure the dynamics. Second, we must assess whether the experimental setup can resolve ATP release times as fast as 25 milliseconds. In this study, we will describe a computational model of a microfluidic system to address the aforementioned concerns.

The microfluidic device should be designed such that the majority of the channel is oxygen-impermeable and should contain an oxygen-permeable region at which the oxygen partial pressure (PO_2) is held at a lower PO_2 than that of the blood. As the blood passes the

oxygen-permeable region, oxygen diffuses out of the blood causing a drop in SO_2. We implemented a similar approach to decrease PO_2 in a 2011 study of methods for localized oxygen delivery *in vivo* [7]. In the current study, oxygenated blood would flow through the channel at a constant flow rate to produce a steady state distribution of SO_2 and ATP levels within the channel. A possible design for a microfluidic device is shown in Fig. 3.1.
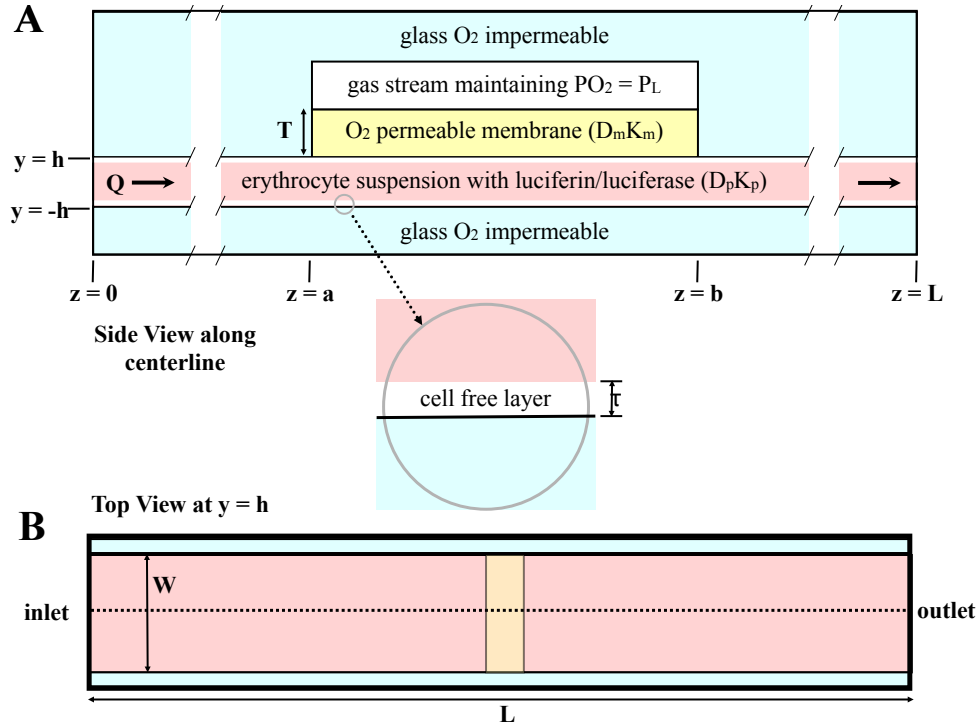
Figure 3.1: *Two-dimensional representation of a microfluidic device for measuring oxygen-dependent ATP release from erythrocytes.* *A. shows the side view along the centerline. This view of the diagram is to scale; the vertical dashed lines indicate where the diagram is broken to allow for the entire device to be shown. B. shows the top view; the dotted line indicates the centerline. Note: this view of the diagram is not to scale.*

To measure ATP levels, the blood in the system will be mixed with a solution of luciferin and luciferase as it enters the microfluidic device. Luciferin and luciferase react with ATP, producing light proportional to the concentration of ATP [8, 9] . The light intensity levels will be measured using a microscope and still-framed camera with appropriate exposure time. Since ATP release will be measured in steady state, changes in time can be measured as changes in position along the channel. Exploiting time in terms of distance allows for the measurement of time on the order of milliseconds without having to use a light detection

system with high temporal resolution. In this paper we present a mathematical model of the microfluidic system to aid in the design the experimental setup and to gain further insights into this phenomenon. The mathematical model will also give us the tools necessary to analyze future experimental results.

3.2   Methods

3.2.1   Overview of Model

The model is comprised of a number of coupled modules, each corresponding to a component of the mass transport and light detection system. The first underlying module in this simulation is a model for the hemodynamics of system. This module determines how the blood plasma and erythrocytes will behave and interact as they flow through the microfluidic device. Based on the hemodynamic module, a second module for oxygen transport was developed. This module describes the convection and diffusion of oxygen within the blood and it also includes the relationship between PO_2 and SO_2.

A module for ATP release was added based on both SO_2 and the hemodynamic module. The ATP module describes the rate of ATP release throughout the microfluidic device. A simple linear relationship between SO_2 and ATP release rate was used, as this is sufficient to determine whether the device is capable of measuring ATP. A linear model was also used in a previous study [10] . A time delay term was included in this module, which accounts for the time required for ATP to be released following the change in SO_2. This term was included to ensure the device was capable of measuring the dynamics of ATP release. A further module for ATP transport was constructed based on the diffusion and convection of ATP in the blood plasma. The degradation of ATP due to the reaction with the luciferin and luciferase solution was also included.

In addition to the degradation of ATP, a module for the light generated by the luciferin and luciferase reaction was developed. This luminescence module was based on the kinetics of the reaction between ATP and the luciferin and luciferase solution. From this module, the amount of light coming from the system was determined and used to calculate the light intensity signal that would be measured by a digital camera. This module includes both the attenuation of light as it passes through hemoglobin based on extinction coefficients and the efficiency of a scientific digital camera for measuring light levels at a wavelength of 560 nm. In this configuration, image acquisition is taken from the top of the channel to acquire the information closest to the oxygen-permeable membrane. A detailed mathematical description of each module follows below.

3.2.2 Hemodynamic Module

The geometry of this model is presented in Fig. 3.1; it considers a slice in the yz-plane along the centerline. Blood flow is assumed to be viscous and in steady state. The module incorporates a core region of blood flow mixed with erythrocytes where hematocrit is assumed to be constant and a cell-free plasma layer along the channel walls where hematocrit is assumed to be zero.

In this model, velocities in the x and y directions are assumed to be zero. The velocity profile of the blood plasma was derived from the Navier-Stokes equations for fluid dynamics. Steady state is assumed, and the shear stress between the cell-free layer and core region is assumed to be equal at the interface. Equation 3.1 governs the flow velocity of the blood plasma.

$$v_p(y) = \frac{3Q}{4w\left[h^3 + \left(\frac{\mu_p}{\mu_c} - 1\right)y_i^3\right]} \begin{cases} \left((h^2 - y_i^2) + \frac{\mu_p}{\mu_c}\left(y_i^2 - y^2\right)\right) & 0 \le y \le y_i \\ (h^2 - y^2) & y_i \le y \le h \end{cases} \tag{3.1}$$

In this equation Q is the flow rate, h is half the height of the channel, w is the width of the

channel, y is the distance from the center of the channel, y_i is the position of the interface between the cell-free layer and the cell-plasma mixture, μ_p is the dynamics viscosity of the cell-free layer and μ_c is the dynamic viscosity of the cell-plasma mixture and is calculated empirically based on the work of Pries *et al.* [11] .

The erythrocytes flow at a velocity slower than the plasma due to slipping. The slip velocity, slp, defines the magnitude of slipping between the plasma and erythrocytes [12]. Equation 3.2 governs the flow velocity of the erythrocytes.

$$v_{RBC} = v_p \left(1 - slp\right) \tag{3.2}$$

Tube hematocrit in a flowing system is different from inlet or discharge hematocrit, and is defined as the fraction of erythrocytes flowing in the core region of blood flow [13]. Equation 3.3 defines the relationship between tube hematocrit (H_T), discharge hematocrit (H_D) and the channel height. τ is the cell-free plasma layer thickness.

$$\frac{H_T}{H_D} = \frac{(1 - slp)}{\left(2 - \left(1 - \frac{\tau}{h}\right)\right)} \tag{3.3}$$

3.2.3   Oxygen Transport Module

Oxygen movement is dictated by diffusion and convection in a flowing system. In this module, oxygen is assumed to diffuse in the y-direction and to move by convection in the z-direction. Oxygen is also transported by erythrocytes through the binding of oxygen to hemoglobin. Equation 3.4a governs oxygen transport in the cell-free plasma layer and Equation 3.4a governs oxygen transport in the blood mixture [12].

PO_2 is the partial pressure of oxygen; D_p is the diffusion coefficient of oxygen in blood plasma; K_p and K_{RBC} are the oxygen solubility in the cell-free plasma layer and blood

mixture respectively; $[Hb_T]$ is the total hemoglobin concentration, and is the derivative of the Hill equation (see Eq. 3.5 below). The initial condition is described by Equation 3.4c and the boundary conditions are described by Equation 3.4d. The oxygen-permeable membrane is present on the upper wall of the channel and extend from $z = a$ to $z = b$ where the PO_2 is set to P_L. D_m and K_m are the diffusion coefficient and solubility of the oxygen-permeable membrane respectively. T is the thickness of the oxygen-permeable membrane.

$$v_p \frac{\partial PO_2}{\partial z} = D_p \frac{\partial^2 PO_2}{\partial y^2} \tag{3.4a}$$

$$\left(v_p \left(1 - H_T \right) + v_{RBC} H_T \frac{K_{RBC}}{K_p} \left(1 + \frac{[Hb_T]}{K_{RBC}} \frac{dSO_2}{dPO_2} \right) \right) \frac{\partial PO_2}{\partial z} = D_p \frac{\partial^2 PO_2}{\partial y^2} \tag{3.4b}$$

$$PO_2(y, 0) = P_0, \qquad\qquad -h \leq y \leq h \tag{3.4c}$$

$$\frac{\partial PO_2}{\partial y}(h, z) = 0 \qquad\qquad \begin{aligned}&0 \leq z \leq a, \\ &b \leq z \leq L\end{aligned}$$

$$\frac{\partial PO_2}{\partial y}(-h, z) = 0 \qquad\qquad 0 \leq z \leq L \tag{3.4d}$$

$$D_p K_p \frac{\partial PO_2}{\partial y}(h, z) = D_m K_m \frac{P_L - P(h)}{T} \qquad\qquad a \leq z \leq b$$

SO_2 was calculated based on the Hill equation, and depends on the PO_2 output of the oxygen transport module. Equation 3.5 is the Hill equation, where N is the Hill coefficient, which characterizes the binding cooperativity of hemoglobin, and P_{50} is the PO_2 at 50% saturation.

$$SO_2 = \frac{PO_2^N}{PO_2^N + P_{50}^N} \tag{3.5}$$

3.2.4   ATP Release Module

This module describes ATP release rates and assumes that the relationship between ATP release rate and SO_2 is linear with a minimum release rate (R_{min}) when hemoglobin is fully

saturated and a maximum release rate (R_{max}) when it is fully de-saturated. Finally, the module assumes that there is a delay between the change in saturation and the change in ATP release rate. Equation 5.12 governs ATP release rate for these assumptions, where td is the time delay.

$$R = (R_{min} - R_{max})SO_2(y, z - v_p t_d) + R_{max} \tag{3.6}$$

3.2.5 ATP Transport Module

This module assumes that ATP diffuses in the y-direction and moves by convection in the z-direction. It assumes that ATP cannot diffuse through the erythrocyte membrane. This module includes erythrocytes as an ATP source and the depletion of ATP due to the reaction with luciferin and luciferase. Equation 3.7 governs ATP transport, where $[ATP]$ is the concentration of ATP; D_{ATP} is the diffusion coefficient of ATP in blood plasma and k_t is the reaction rate constant for the luciferin and luciferase reaction with ATP.

$$v_p \frac{\partial [ATP]}{\partial z}(1 - H_t) = D_{ATP}\frac{\partial^2 [ATP]}{\partial y^2}(1 - H_T) + R \cdot H_T - k_t[ATP](1 - H_T) \tag{3.7}$$

The differential equation was solved assuming that there is no ATP flux at the channel walls and that the luciferin and luciferase solution is being mixed at the inlet of the channel. It is assumed that there is no ATP entering the channel at the inlet and there is no ATP flux at the O_2-permeable membrane.

3.2.6 Luminescence Module

The luminescence in this system is derived from the kinetics of the reaction between ATP and luciferin/luciferase. Equation 3.8 shows the complete reaction [9].

$$\text{ATP} + \text{luciferin} + \text{O}_2 \xrightleftharpoons{\text{luciferase}} \text{oxyluciferin} + \text{AMP} + \text{PP}_i + \text{CO}_2 + \text{h}\nu \qquad (3.8)$$

This reaction has first order kinetics such that the rate of reaction only depends on the concentration of ATP [8] ; therefore, the rate at which light is produced is proportional to the rate of ATP consumption. For the amount of ATP released from erythrocytes, the concentration of the luciferin and luciferase solution will be much greater than that of ATP; therefore product inhibition can be assumed to be negligible. Equation 3.9 describes the rate, I, at which light is produced, where α is the quantum efficiency, V is the volume of each voxel, N_A is Avogadro's number and k_t is the rate constant of the reaction [9] . The reaction constant k_t varies typically between 0.1 and 1.0 s^{-1} [9].

$$I = \alpha \cdot V N_A \cdot k_t \cdot [ATP] \qquad (3.9)$$

3.2.7 Optics Module

Photon detection is based on the number of photons that reach the digital camera's charge-coupled device (CCD) and the device's ability to undergo the photoelectric effect. This module accounts for photon attenuation by hemoglobin and the fact that a point source emits light in all directions. Equation 3.10 describes the number of photons acquired per pixel; where t_s is the camera's shutter speed; A_{pixel} is the surface area of the pixel and μ is the attenuation coefficient.

$$\gamma = \int_0^{2h} I \cdot t_s \cdot A_{pixel} \frac{e^{-\kappa y}}{4\pi y^2} dy \qquad (3.10)$$

It is known that oxyhemoglobin and deoxyhemoglobin have different attenuation coefficients depending on wavelength. Equation 3.11 describes the light attenuation coefficient through the blood mixture as a function of saturation, where κ_p, κ_{Hb} and κ_{HbO_2} are the attenuation coefficients of the blood plasma, deoxyhemoglobin and oxyhemoglobin respectively at the

wavelength of light produced by the luciferin/luciferase reaction with ATP, 560 nm.

$$\kappa = (1 - H_T)\,\kappa_p + H_T\left((1 - SO_2)\,\kappa_{Hb} + SO_2\kappa_{HbO_2}\right) \qquad (3.11)$$

The signal read by the device comes from the amount of electrons released by the photons collected from the photoactive region of each well of the CCD. Thus the signal depends on the efficiency of the photoelectric effect (η) and the amount of photons collected on the surface of each well. Equation 3.12 describes the signal read by the device, where S_{total} is measured in electrons.

$$S_{total} = \eta \cdot \gamma \qquad (3.12)$$

The device reads out each well and converts the number of electrons measured into a digital signal that depends on the memory information of the device. Equation 3.13 gives a measurement of the output signal relative to the maximum measurable signal by the CCD; this will be referred to as the relative output signal. The full-well capacity (FWC) of the CCD is the maximum number of electrons that each well can hold.

$$S_{relative} = \begin{cases} \dfrac{S_{total}}{FWC}, & S_{total} < FWC \\ 1, & S_{total} \geq FWC \end{cases} \qquad (3.13)$$

3.2.8 Simulations

All numerical analyses were done in Mathworks MATLAB 7.11.0 (R2010b). Grid spacing for the model was 321×4000 (y-z). The parameters of the model are specified in Table 4.1. All simulations reached a stable solution. The default simulation was performed with a grid spacing of 321×4000, 642×8000 and 1284×16000; these simulations reached the same stable solution.

Table 3.1: *Model Parameters*

Parameter	Variable	Value
Flow Rate (μL/min)	Q	7.8
Device Height (μm)	H	100
Device Width [13] (μm)	W	1500
Plasma Viscosity (Pa·s)	μ_p	0.001
Slip Coefficient [12]	slp	0.1
Discharge Hematocrit	H_D	0.2
Plasma Layer Thickness (μm)	τ	1
O_2 Diffusivity in Plasma [12] (μm^2/s)	D_p	2750
O_2 Solubility in RBCs [12] (μM/mmHg)	K_{RBC}	1.47
O_2 Solubility in Plasma [12] (μM/mmHg)	K_p	1.33
Total Heme Concentration [12] (μM)	Hb_T	5350
Inlet PO_2 (mmHg)	P_0	150
O_2-Permeable Membrane PO_2 (mmHg)	P_b	10
O_2-Permeable Membrane Start Position (μm)	a	7000
O_2-Permeable Membrane End Position (μm)	b	7700
Device Length (μm)	L	14000
O_2 Diffusivity in O_2-Permeable Membrane (μm^2/s)	D_m	160000
O_2 Solubility in O_2-Permeable Membrane (μM/mmHg)	K_m	17.959
O_2-Permeable Membrane Thickness (μm)	T	100
Hill Coefficient [12]	N	2.7
Partial Pressure at 50% Saturation [12] (mmHg)	P_{50}	27
Minimum ATP Release Rate (μM/s)	R_{min}	0
Maximum ATP Release Rate (μM/s)	R_{max}	14
ATP Release Time (s)	t_d	0
ATP Diffusivity in Plasma [14] (μm^2/s)	D_{ATP}	475
ATP/Luciferin Reaction Rate [9] (s^{-1})	k_t	0.1
Quantum Efficiency [9]	α	0.88
Shutter Speed (s)	t_s	10
Pixel Surface Area* (μm^2)	A_{pixel}	166.41
Plasma Attenuation Coefficient (μm^{-1})	k_p	0.1
Oxyhemoglobin Attenuation Coefficient** (μm^{-1})	k_{O_2Hb}	0.040176
Hemoglobin Attenuation Coefficient** (μm^{-1})	k_{Hb}	0.066261
Camera Efficiency*	η	0.7
Full Well Capacity* (electrons)	FWC	22000

Units are given in the first column. One asterisk (*) indicates parameters taken from the specification of Qimaging's Rolera XR camera. Two asterisks (**) indicates parameters calculated from tabulated molar extinction coefficients for hemoglobin in water at 560 nm; these values were compiled by Scott Prahl (prahl@ece.ogi.ed).

3.3 Results

The computational model simulated experiments with the parameters specified in Table 1. The parameters that are varied during the simulations are summarized in Table 2. The first simulation was used to test the feasibility of the experimental setup. This simulation shows that the PO_2 decreases from 150 mmHg to below 57 mmHg in the vicinity of the oxygen-permeable membrane and to 95 mmHg across the entire width of the channel 3 mm downstream from the end of the membrane (Fig. 3.2A). This simulation also shows that the SO_2 decreases from 99% to below 65% in the immediate vicinity of the oxygen-permeable membrane (Fig. 3.2B) but rapidly rises back up to 97% within 1.9 mm downstream. It should be noted that this erythrocyte resaturation occurs due to the diffusion of oxygen from regions further from the membrane that were initially less affected by low O_2 at the membrane surface. The ATP concentration, accounting for both the release from erythrocytes and degradation by luciferin/luciferase, is shown to reach a peak value of 0.2 μM in the vicinity of the oxygen-permeable membrane with the concentration decreasing immediately after the end of the membrane (Fig. 3.2C). The relative output signal shown in Fig. 3.2D is the accumulated light produced by the luciferin/luciferase reaction as measured by the camera; this measurement is normalized by the maximum signal measurable by the camera for the parameter settings given in Table 1. The relative output signal begins a rapid increase from 0.032 at the position of the beginning of the membrane and reaches a maximum value of 0.191 at the end of the membrane.

The second simulation was used to analyze the choice of channel height and its effect on the resulting output signal (Fig. 3.3). All the channel heights show a rapid increase at the beginning of the oxygen-permeable membrane, this corresponds to ATP release being turned on due to the rapid desaturation of the erythrocytes. However, the 25 and 50 μm channels do not show a clear turn off of ATP release; this is because the O_2-permeable membrane reduces O_2 levels across the entire channel and hence the erythrocytes do not resaturate downstream of the membrane (Fig. 3.3A).

Table 3.2: *Simulation Parameter Range*

Parameter	Range	Simulation Number
Device Height (μm)	$25 - 400$	2
Membrane Permeability (M·μm^2/(mmHg·s))	$0.06 - 3.84$	7
Flow Rate (μL/min)	$3.30 - 18.24$	4
ATP Release Time (s)	$0.00 - 4.00$	3, 4
Maximum ATP Release Rate (μM/s)	$10.0 - 25.0$	5
Minimum ATP Release Rate (μM/s)	$0.0 - 1.5$	5
ATP/luciferin Reaction Rate (s^{-1})	$0.0 - 1.0$	6

Model parameters that were varied in each of the simulations along with the range of the parameter values. Units are given in the first column and simulation number is indicated in the last column.

The third simulation was used to analyze the change in output signal when varying the ATP release time. Increasing release times resulted in a downstream shift in the output signal peak by 1304 μm per second of ATP release time. It should be noted that for this case the mean velocity in the channel is 1263 μm/s (Fig. 3.4).

The fourth simulation was used to analyze the effect of flow rate on the maximum signal strength and spatial resolution (Fig. 3.5). Increased flow rate resulted in an increased flux in oxygen across the oxygen-permeable membrane (Fig 3.5A). Increased flow rate resulted in increased spatial resolution (Fig. 3.5B); however, it also resulted in decreased signal strength (Fig. 3.5C). For a 5.5 fold increase in flow rate, signal strength decreases by a factor of 3.6. For the 25-millisecond ATP release time, the peak signal shifts linearly with flow rate.

The fifth simulation considered two parameters that control the ATP release module. The first parameter determines the release rate when the erythrocyte is fully saturated; this is the minimum ATP release rate, R_{min}. The second parameter determines the release rate when the erythrocyte is fully desaturated; this is the maximum ATP release rate, R_{max}. The results of increasing R_{min} and R_{max} are shown in Figs 3.6A and 3.6B, respectively.
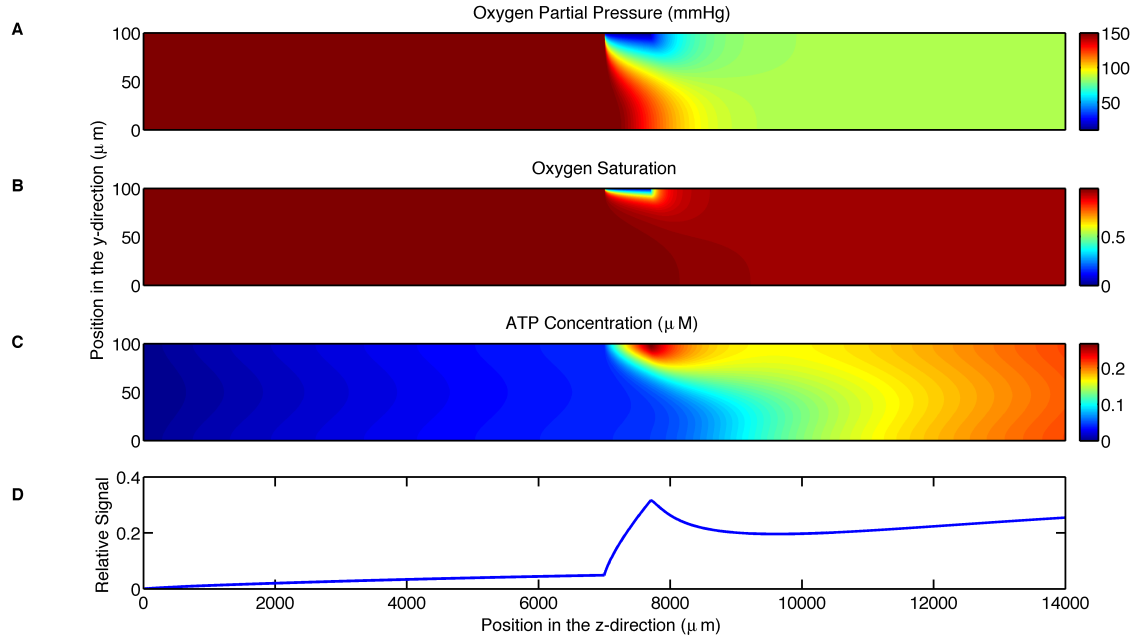
Figure 3.2: *Shows the simulation results for the parameters in Table 1.* A. displays the oxygen partial pressure (mmHg) as a function of position (μm) throughout the microfluidic device. B. displays hemoglobin oxygen saturation as a function of position (μm) throughout the microfluidic device. C. displays the ATP concentration (μM) as a function of position (μm) throughout the microfluidic device. D. displays the relative output signal as a function of longitudinal position.

Changing the minimum and maximum ATP release rates resulted in a change in the shape of the output signal.

The sixth simulation was used to investigate the effect of the rate of the luciferin/luciferase reaction on the concentration of ATP in the channel; three degradation rates (0, 0.1, 1.0 s^{-1}) were simulated. Although the case with zero degradation does not result in an output signal that can be measured by the camera, this simulation shows the ATP concentration due to the release from erythrocytes (Fig. 3.7A). As the degradation rate increases, ATP concentration in the channel decreases. With increasing degradation rate, the amount of light produced increases and hence the signal strength as measured by the camera also increases. This results in the apparent paradox that the highest signal strength occurs with the lowest ATP concentration in the channel. The total concentration of ATP in the channel for the zero degradation case is a factor of 1.3 and 4.9 larger than the total concentration for the degradation rates of 0.1 s^{-1} (Fig. 3.7B) and 1.0 s^{-1} (Fig. 3.7C), respectively. The
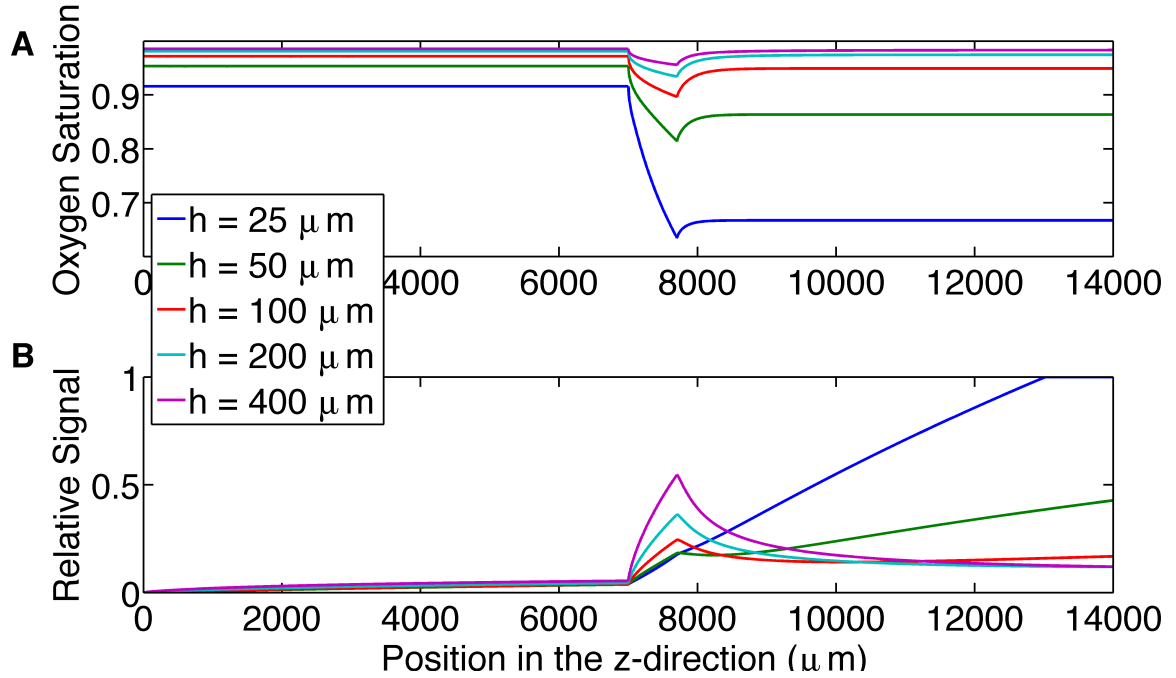
Figure 3.3: *Shows the effect of increasing channel height.* *A. displays the mean hemoglobin oxygen saturation across the channel as a function of position (µm) along the microfluidic device for channel heights of 25, 50, 100, 200 and 400 µm. B. displays the relative output signal as a function of position (µm) for channel heights of 25, 50, 100, 200 and 400 µm.*

maximum output signal is 5.2 fold larger with a degradation rate of 1.0 s^{-1} compared to 0.1 s^{-1} (Fig. 3.7D).

The seventh simulation was used to analyze the effect of the permeability of the oxygen-permeable membrane on SO_2 (Fig. 3.8). The membrane with the highest permeability $(3.84 \text{ (M } \mu\text{m}^2)/(\text{mmHg s}))$ had the ability to cause a maximum decrease from 99% to 12% whereas the membrane with the lowest permeability $(0.06 \text{ (M m2/(mmHg s))})$ was able to cause a maximum decrease from 99% to 53%.

3.4 Discussion

The first simulation predicts that this design of a microfluidic device will be able to cause a sufficient drop in oxygen partial pressure across the width of the channel (Fig. 3.2A). This
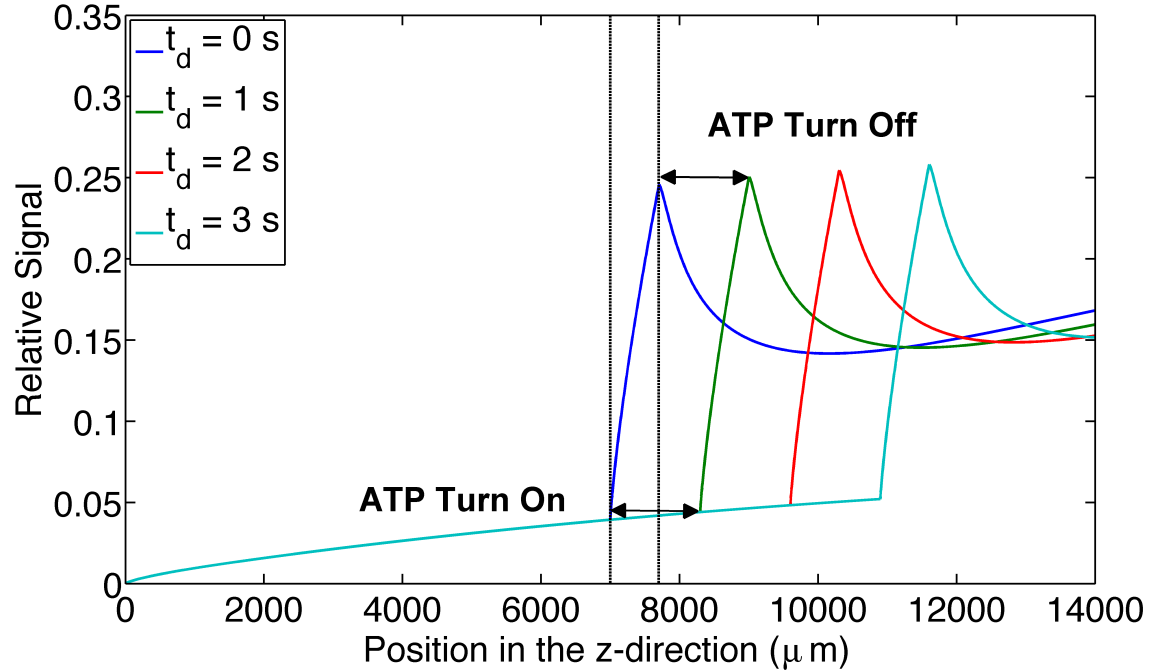
Figure 3.4: *Shows the effect of increasing ATP release times. The figure displays the relative output signal for increasing ATP release times (0 s, 1 s, 2 s and 3 s) as a function of longitudinal position (µm) throughout the microfluidic device. ATP release turn on and turn off time is indicated on the graph for the 1 s delay time.*

finding also verifies that the design of the device is effective for the purpose of causing a decrease in oxygen saturation. From this simulation, it is evident that a similar experimental procedure to that of the study of shear-dependent ATP release [4] can be repeated with this microfluidic device to study the oxygen-dependent release of ATP.

The first simulation also confirms that a digital camera will be able to measure a signal given the small concentration of ATP released from red blood cells using an exposure time of 10 seconds. The advantage of using a digital camera over a photomultiplier tube (a common method of acquiring low intensity light) is the ability to acquire all of the spatial light intensity data simultaneously at a high spatial resolution. The resulting image in combination with the simulation can be used to estimate the ATP concentration prior to degradation by the luciferin and luciferase reaction.

From the results of simulation 2 (Fig. 3.3), larger channel heights cause a peak in the
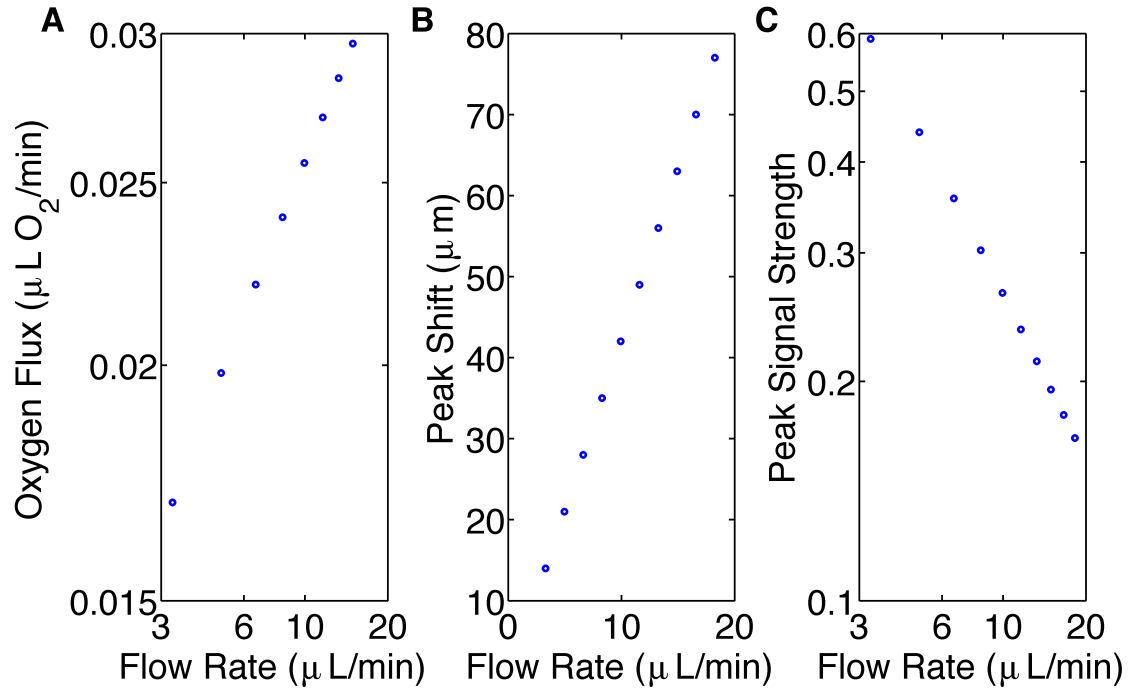
Figure 3.5: ***Shows the effects of flow rate on the system.*** *A. displays the oxygen flux (μL O_2/min) across the oxygen-permeable membrane as a function of flow rate ($\mu L/min$) using a log-log scale. The data lie on a straight line with slope of 0.37. B. displays the local maximum shift (mm) caused by a 25 ms delay in ATP release as a function of flow rate ($\mu L/min$). The data lie on a straight line with slope 4.2. C. displays the magnitude of the local maximum of the output signal as a function of flow rate (mL/min) using a log-log scale. The data lie on a straight line with slope of 20.75.*

output signal, allowing us to determine the location where ATP release turns off as the erythrocytes resaturate with oxygen from deeper in the channel.

Varying ATP release times and analyzing the corresponding output signals shows a visible change in the output signal curve. Increasing the ATP release time results in a downstream shift in the signal peak. This implies that ATP release time is measurable with this setup provided that the system remains in steady state. This allows us to use our system of high spatial resolution to obtain high temporal resolution. Measuring the distance between the beginning of the oxygen-permeable membrane and the start of the rapid increase in signal gives us information about the amount of time it take for ATP release to turn on. Measuring the distance between the end of the oxygen-permeable membrane and the peak in signal gives us information about the time it takes ATP release to turn off. In our model these
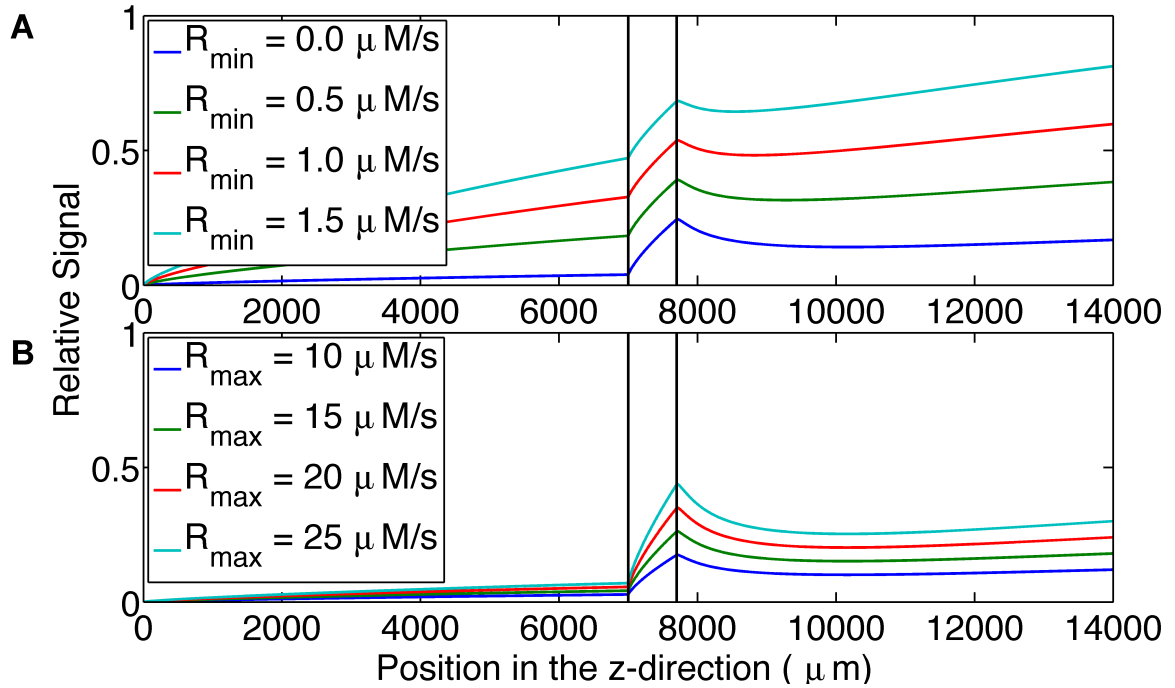
Figure 3.6: *Shows the effect of ATP release rate parameters on output signal.* *A. displays the relative output signal for increasing minimum ATP release rates (0.0 µM/s, 0.5 µM/s, 1.0 µM/s, 1.5 µM/s) as a function of longitudinal position (mm) in the microfluidic device. B. displays the relative output signal for increasing maximum ATP release rates (10 µM/s, 15 µM/s, 20 µM/s, 25 µM/s) as a function of longitudinal position (µm) in the microfluidic device. The system is more sensitive to changes in minimum ATP release rate.*

two times are modelled as being the same, however, a recent study modelling the dynamics of the signal transduction pathway for ATP release suggests they may be different [15].

Varying flow rate and analyzing the corresponding change in the peak signal position shows that the system's resolution increases as flow rate increases, allowing us to control temporal resolution. However, the signal strength decreases with increasing flow rate. This finding demonstrates that there is a compromise between our system's resolution and the amount of measurable signal. Additionally, oxygen flux across the oxygen-permeable membrane increases with increasing flow rate; this follows a power law with a power of 0.37. This finding is consistent with mass transport theory, which results in a power of 1/3 for high shear Péclet number [16]. The small discrepancy in the power may be due to the inhomogeneous distribution of oxygen throughout the oxygen-permeable membrane and because the shear Péclet number for our simulations may not be sufficiently large. The shear Péclet number
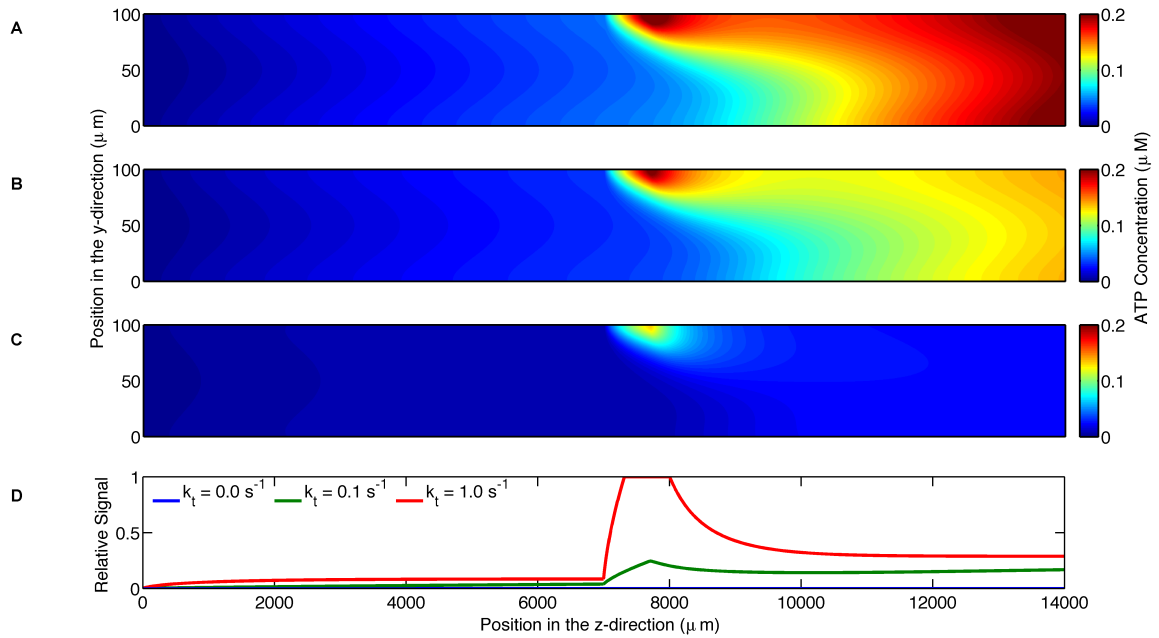
Figure 3.7: *Shows the effect of ATP degradation on output signal. A. displays ATP concentration (µM) as a function of position (µm) throughout the microfluidic device where the blood does not contain the luciferin/luciferase solution. B. displays ATP concentration (µM) as a function of position (µm) throughout the microfluidic device where the blood contains the luciferin/luciferase solution with a degradation rate of 0.1 s21. C. displays ATP concentration (µM) as a function of position (µm) throughout the microfluidic device where the blood contains the luciferin/ luciferase solution with a degradation rate of 1 s21. D. shows output signal as a function of longitudinal position along the microfluidic device for the two degradation rates. The higher degradation rate results in a larger output signal.*

for oxygen transport in our simulations range from 108.78 and 601.72. Despite the increase in O_2 flux with increasing flow rate, the signal strength decreases due to the decrease in erythrocyte transit time from leading to trailing edge of the membrane. As transit time decreases there is less time for erythrocytes to release ATP.

The flow rates used in this study (3.30-18.24 µL/min) are much smaller than the flow rate used in the study by Wan *et al.* (50 µL/min) [4], implying that the shear-dependent ATP release can be ignored. Varying the exposure time is another parameter that can be controlled to increase signal strength.

Another important finding from this study is that to calculate ATP release time, we need to
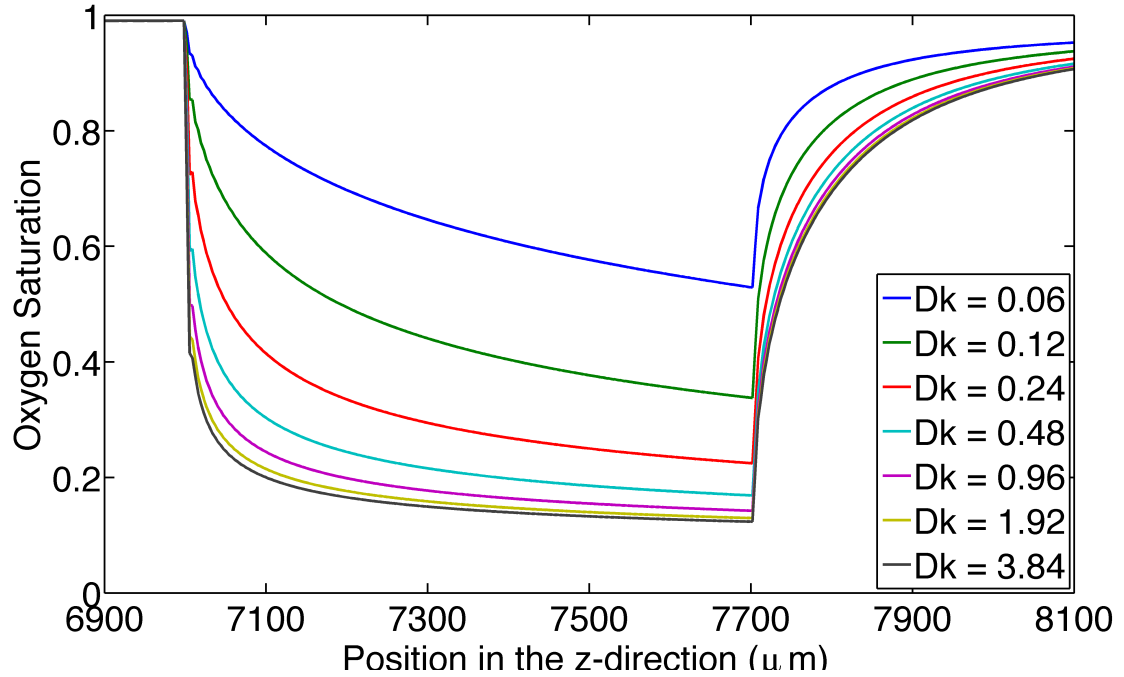
Figure 3.8: ***Displays the effect of the permeability of the oxygen-permeable membrane on oxygen saturation.*** *This figure shows hemoglobin oxygen saturation near the oxygen-permeable membrane as a function of time (s) for increasing permeability of the oxygen-permeable membrane in units $M{\cdot}\mu m^2/(mmHg{\cdot}s)$.*

know the velocity of the blood, which is variable across the device. Deciding which velocity to use is necessary to calculate the correct release time. This time can be calculated using our model.

ATP release rate and ATP concentration can be determined from the simulation, providing useful information about the system that would be difficult to measure directly. Comparing the simulations with and without the degradation due to the luciferin and luciferase reaction (Fig. 3.7), it is shown that the concentrations of ATP in the system differ by over a factor of two. This finding demonstrates that in order to determine the concentration of ATP released by the erythrocytes in a dynamic system, the calculations must account for the degradation due to the reaction. The light intensity profile measured by the camera does not directly reflect the ATP concentration produced by the oxygen-dependent release; this is due to the ATP degradation by the luciferin and luciferase reaction in a flowing system. Fig. 3.7 demonstrates that different degradation rates can have a substantial ef-

fect on the estimated ATP concentrations indicating that one must carefully determine what the ATP degradation rate is for the experimental system used. Relying solely on the measured light intensity signal may result in misinterpretation of the ATP release dynamics.

From the results of the sixth simulation (Fig. 3.8), it is demonstrated that with increasing O_2 diffusivity of the O_2-permeable membrane, the drop in saturation becomes independent of the diffusivity.

Varying the minimum and maximum ATP release rates independently and analyzing the resulting output signal shows a measurable signal difference between the different parameters of the ATP release module. This finding supports the objective of being able to study the oxygen-dependent release of ATP because the model allows for the differentiation of individual components of the ATP release module. Further, the model can be used with the experimental procedure to adjust the three parameters (minimum and maximum release rate and release time) in the model so they match the experimental results.

A recent study suggests that ATP release may be proportional to the rate of oxygen desaturation rather than the magnitude of the saturation [15]. By varying the oxygen permeability of the oxygen-permeable membrane, the model shows that the rate of desaturation may be controlled. By varying the length of the membrane, we can control the magnitude of desaturation; this will allow for the verification of this theory (see Fig. 3.8).

As we gain a better understanding of the dynamics of the signalling pathway for ATP release, these can be incorporated into our simulation. Ultimately, model parameters could be varied to yield the best fit with experimental measurements. Improving the model of ATP release will allow it to be used for modelling local oxygen regulation in the microvasculature *in vivo* and for the design and interpretation of *in vivo* experiments.

The results of such experiments can then be compared to the ATP release magnitude and dynamics that occur in cardiovascular disease. Finding differences between the ATP release magnitude and dynamics will allow the device combined with the model to be used to screen blood from patients with cardiovascular disease to determine whether cardiovascular disease is present.

In conclusion, a microfluidic device can be designed to produce a rapid decrease in the oxygen saturation of erythrocytes across the width of the channel resulting in a measurable ATP signal that can be analyzed for the dynamics of oxygen saturation-dependent ATP release. In addition, this computational model is an effective tool to optimize the microfluidic experiment to be able to determine the time course of ATP release from erythrocytes. Further, it can be used to determine other unknown parameters such as the minimum and maximum ATP release rate. The model may also be used in the analysis of experimental results that may be difficult to interpret, such as determining the concentration of ATP in the system prior to the degradation from the luciferin and luciferase reaction and the conversion of the spatial displacement of ATP release into ATP release time. The model can also be modified based on experimental results to further develop the model leading to a better understanding of the ATP release pathway. Further, this model is testable; experimental measurements of oxygen saturations [17] and ATP concentrations [8] can be made to justify the results of the model. In future studies, the model may be also used for the analysis of systems *in vivo* where parameter may often be very difficult to measure.

References

[1] R. J. Sové, N. Ghonaim, D. Goldman, and C. G. Ellis, "A computational model of a microfluidic device to measure the dynamics of oxygen-dependent ATP release from erythrocytes," *PLOS ONE*, vol. 8, p. e81537, Nov. 2013.

[2] H. H. Dietrich and M. L. Ellsworth, "Red blood cell regulation of microvascular tone through adenosine triphosphate," *American Journal of . . .* , 2000.

[3] M. L. Ellsworth, C. G. Ellis, D. Goldman, A. H. Stephenson, H. H. Dietrich, and R. S. Sprague, "Erythrocytes: Oxygen sensors and modulators of vascular tone," vol. 24, pp. 107–116, Apr. 2009.

[4] J. Wan, W. D. Ristenpart, and H. A. Stone, "Dynamics of shear-induced ATP release from red blood cells," *Proceedings of the National Academy of Sciences*, vol. 105, pp. 16432–16437, Oct. 2008.

[5] M. L. Ellsworth, "The red blood cell as an oxygen sensor: what is the evidence?," *Acta physiologica Scandinavica*, vol. 168, pp. 551–559, Apr. 2000.

[6] R. S. Sprague, E. A. Bowles, D. Achilleus, A. H. Stephenson, C. G. Ellis, and M. L. Ellsworth, "A selective phosphodiesterase 3 inhibitor rescues low PO2-induced ATP release from erythrocytes of humans with type 2 diabetes: implication for vascular control," *AJP: Heart and Circulatory Physiology*, vol. 301, pp. H2466–H2472, Dec. 2011.

[7] N. W. Ghonaim, L. W. M. Lau, D. Goldman, C. G. Ellis, and J. Yang, "A micro-delivery approach for studying microvascular responses to localized oxygen delivery," vol. 18, pp. 646–654, Nov. 2011.

[8] M. DeLuca and W. D. McElroy, "Kinetics of the firefly luciferase catalyzed reactions," *Biochemistry*, vol. 13, no. 5, pp. 921–925, 1974.

[9] K. Salama, H. Eltoukhy, A. Hassibi, and A. E. Gamal, "Modeling and simulation of luminescence detection platforms," *Biosensors and Bioelectronics*, vol. 19, pp. 1377–1386, June 2004.

[10] J. C. Arciero, B. E. Carlson, and T. W. Secomb, "Theoretical model of metabolic blood flow regulation: roles of ATP release by red blood cells and conducted responses," *Am J Physiol Heart Circ Physiol*, 2008.

[11] A. R. Pries, D. Neuhaus, and P. Gaehtgens, "Blood viscosity in tube flow: dependence on diameter and hematocrit," *AJP: Heart and Circulatory Physiology*, vol. 263, pp. H1770–H1778, Dec. 1992.

[12] T. E. Moschandreou, C. G. Ellis, and D. Goldman, "Influence of tissue metabolism and capillary oxygen supply on arteriolar oxygen transport: A computational model," *Mathematical Biosciences*, vol. 232, pp. 1–10, July 2011.

[13] M. A. Moyers-Gonzalez and R. G. Owens, "Mathematical modelling of the cell-depleted peripheral layer in the steady flow of blood in a tube," *Biorheology*, 2010.

[14] M. J. Hubley, B. R. Locke, and T. S. Moerland, "The effects of temperature, pH, and magnesium on the diffusion coefficient of ATP in solutions of physiological ionic strength," *Biochimica et Biophysica Acta (BBA) - General Subjects*, vol. 1291, pp. 115–121, Oct. 1996.

[15] D. Goldman, "Toward a multiscale description of microvascular flow regulation: O2-dependent release of ATP from human erythrocytes and the distribution of ATP in capillary networks," pp. 1–11, July 2012.

[16] W. Zhang, H. A. Stone, and J. D. Sherwood, "Mass transfer at a microelectrode in channel flow," *The Journal of Physical Chemistry*, vol. 100, no. 22, pp. 9462–9464, 1996.

[17] M. L. Ellsworth, R. N. Pittman, and C. G. Ellis, "Measurement of hemoglobin oxygen saturation in capillaries," *AJP: Heart and Circulatory Physiology*, vol. 252, pp. H1031–H1040, May 1987.

Chapter 4

Finite Element Model of Oxygen Transport for the Design of Geometrically Complex Microfluidic Devices Used in Biological Studies[1]

4.1 Introduction

Red blood cells (RBCs) have been shown to release adenosine triphosphate (ATP) in response to numerous stimuli [2–5], including hemoglobin oxygen saturation (SO_2) [6]. Following release, ATP binds to purinergic receptors on capillary endothelial cells which conduct an electrical response to upstream arterioles, leading to their vasodilation [7]. Therefore, RBCs are believed to play an important role in the local regulation of oxygen (O_2) distribution through the SO_2-dependent release of ATP [8, 9].

In addition to its importance in regulatory physiology, SO_2-dependent ATP release has been shown to be impaired in many cardiovascular diseases such as sepsis [10], prediabetes [11] and type II diabetes [12]. In these studies, the amount of ATP released was decreased for

---

[1]A version of this chapter has been published in PLOS ONE [1].

the same stimulus. Therefore, RBCs become a potential screening target for cardiovascular disorders.

Although SO_2-dependent ATP release has been measured, there are currently no studies that quantify the dynamics of this process. Since ATP release is believed to be involved in the regulation of O_2 distribution, understanding the dynamics is crucial for our understanding of the regulatory pathway. The time required for ATP to be released determines the spatial sensitivity for the RBC to signal to the endothelium changes in their SO_2.

The ultimate goal of our research is to develop a cost effective tool to quantify the dynamics of ATP release from RBCs furthering our ability to characterize the underlying physiology of blood flow regulation. Various studies in the literature have developed means of controlling O_2 in microfluidic devices for a variety of applications [13–20], e.g. microfluidic devices for establishing hypoxia in cell cultures [13]. Many of these studies apply mathematical modelling to verify that they are correctly maintaining their target O_2 levels [14–16, 18, 19].

In an earlier study, we employed a novel micro-delivery approach to change local oxygen levels *in vivo* [21, 22]. We also previously described a computational model of an idealized microfluidic device to measure the dynamics of SO_2-dependent ATP release *in vitro* [23]. The objective of the design was to create a spatial step change in SO_2 in a steady flowing channel, then measure the corresponding ATP released from the RBCs. The resulting spatial information can then be translated into temporal. This approach was adapted from *Wan et al* [24], and is described in detail in our previous study [23]. In contrast to other devices for controlling oxygen, our application is intended to spatially control the O_2 content of flowing RBCs.

Although the previous model predicted that the device was able to create a sufficient drop in O_2, the idealized microfluidic device was not practical to fabricate using common soft

lithography techniques. This motivated a new device design that is both practical and functional. However, the complex geometric design of the new device and the use of O_2-permeable materials makes predicting the SO_2 of the RBCs more difficult. Therefore, in this study we develop a 3D computational model of the new device, in order to optimize the dimensions, and to ensure that O_2 characteristics in the device are sufficient for quantifying the dynamics of SO_2-dependent ATP release. Additionally, this model will be crucial to aid in the analysis of results of subsequent studies using this design.

4.2 Methods

In this work, we take a computational approach to design a device for measuring the dynamics of SO_2-dependent ATP release from RBCs. We propose a device that consists of two parts (see Fig 4.1), the first part being a microfluidic channel fabricated in PDMS using soft lithography techniques. This channel will be embedded in PDMS using a mould, and sealed with a PDMS spin coating technique. The second part being a large oxygen-impermeable gas flow channel with a window to allow gas exchange between the two channels. The two parts are aligned orthogonal to each other with the gas exchange window centred at their intersection. The bottom channel is designed to deliver a gas with a low concentration of oxygen, whereas the top microfluidic channel will deliver fully oxygen-saturated red blood cells suspended in a physiological buffer. The large gradient in oxygen partial pressure at the exchange window between the two channels drives the desaturation of the RBCs.

In the present work, we will explore the influence of geometry on the device's ability to control the oxygen levels the cells are exposed to using a computational model of fluid dynamics and mass transfer (kinetics of ATP release and reaction with luciferin/luciferase will be simulated in a subsequent model); see Fig 4.1 for the geometry. Due to the large number of geometric parameters we can vary, we start by analyzing a 1D analytic model of oxygen exchange to guide our choice of parameters to vary with the 3D model.
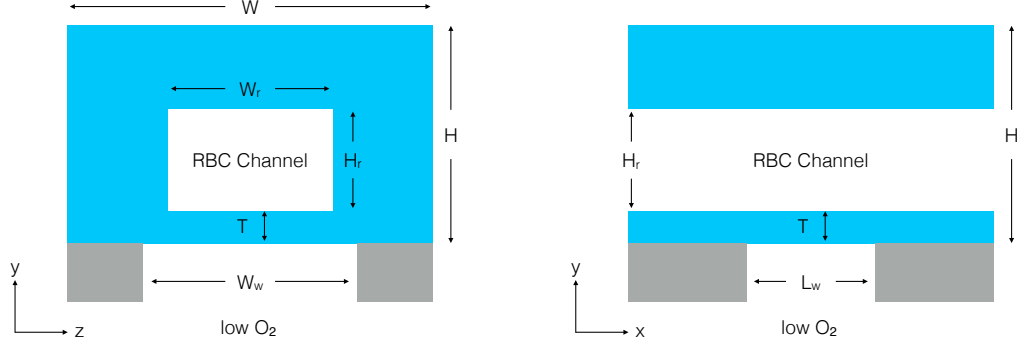
Figure 4.1: Device Design *Diagram of x-normal (left) and z-normal (right) views of the RBC channel and exchange window. The light blue colour represents PDMS and the grey colour represents glass.*

4.2.1 Analytic Model

The following equation describes the oxygen partial pressure, PO_2, of the blood in a microfluidic device with an exchange window of length L_w centred at $x = 0$.

$$D\frac{d^2 PO_2}{dx^2} - c\frac{dPO_2}{dx} = \begin{cases} k_1(PO_2 - P_0), & x \in \left(-\infty, -\frac{L_w}{2}\right) \\ k_1(PO_2 - P_0) + k_2(PO_2 - P_l), & x \in \left[-\frac{L_w}{2}, \frac{L_w}{2}\right] \\ k_1(PO_2 - P_0), & x \in \left(\frac{L_w}{2}, \infty\right) \end{cases} \tag{4.1}$$

with boundary conditions,

$$\lim_{x \to -\infty} P(x) = P_0 \tag{4.2a}$$

$$\lim_{x \to \infty} P(x) = P_0 \tag{4.2b}$$

where D is diffusivity of oxygen in plasma, c is the flow velocity, and k_1 and k_2 are the rates of oxygen permeation through the walls of the channel and the exchange window respectively; they depend on the thickness of the PDMS walls and the permeability of PDMS to O_2. P_0 is the external oxygen partial pressure and P_l is the oxygen partial pressure of the gas in the

exchange window. The microfluidic device is assumed to be infinitely long so that we can neglect inlet/outlet effects and the effects of oxygen binding to hemoglobin are neglected in the model.

Non-Dimensional Analysis

Non-dimensionalization allows us to determine the parameters that effect the behaviour of the solution. We introduce the following dimensionless parameters: $\xi = \frac{x}{L_w} + \frac{1}{2}$, $v = \frac{PO_2 - P_l}{P_0 - P_l}$, $u = 1 - v$, $Pe = \frac{cL_w}{D}$, $S_1 = \frac{k_1 L_w^2}{D}$ and $S_2 = \frac{k_2 L_w^2}{D}$ which gives,

$$\frac{d^2u}{d\xi^2} - Pe\frac{du}{d\xi} - S_1 u = \begin{cases} 0, & \xi \in (-\infty, 0) \\ S_2(u+1), & \xi \in [0,1] \\ 0, & \xi \in (1, \infty) \end{cases} \tag{4.3}$$

with homogeneous boundary conditions at infinity. Dimensionless O_2 is represented by v and the dimensionless drop in O_2 is represented by u. From the non-dimensionalization, we see that the behaviour of the solution depends on three independent parameters, Pe, S_1 and S_2. Pe is the Peclet number and represents the ratio of convective to diffusive transport. S_1 and S_2 are dimensionless k_1 and k_2, respectively. The dimensionless solution for a specific case is shown in Fig 4.2.

There are three main criteria that we will use to assess the performance of the device. First, the device must be able to cause a large enough change in O_2 to elicit ATP release from the RBCs. This first criterion can be quantified by taking the maximum drop in PO_2. Eq 4.4 gives this criterion in terms of the 1D model parameters,

$$\Delta PO_{2max} = (P_0 - P_l)u_{max} \tag{4.4}$$
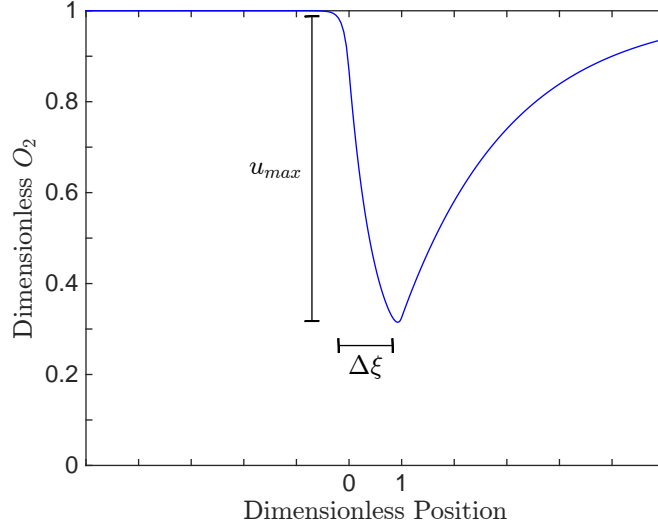
Figure 4.2: Dimensionless Solution *Solution to the 1D dimensionless model. The dimensionless O_2, v, is shown as a function of dimensionless position, ξ for $Pe = 10$, $S_1 = 5$ and $S_2 = 20$. The exchange window is between 0 and 1. The red arrow indicates $\Delta\xi = 1.04$ with u_{max} of 0.68. For this set of conditions, dimensionless O_2 begins to fall just before the window and continues to fall across the length of the window before beginning to rise.*

where u_{max} is the maximum value of $u(\xi)$.

Second, the drop in O_2 must be sufficiently rapid to resolve the dynamics of ATP release. This can be quantified as the amount of time between the maximum and the minimum PO_2. Since this time depends on $\Delta PO_{2_{max}}$, we normalize it with respect the drop. This criterion is a representation of the rate of O_2 drop. Eq 4.5 gives the second criterion in terms of the 1D model parameters,

$$\frac{\Delta PO_{2_{max}}}{\Delta t} = \frac{c(P_0 - Pl)}{L}\frac{u_{max}}{\Delta\xi} \tag{4.5}$$

where $\Delta\xi$ is the change in dimensionless position between when the maximum and minimum value of $u(\xi)$ deviate by 1% of their original values.

Third, the temporal resolution of the system has to be able to resolve the dynamics. This

can be quantified in terms of the spatial resolution, ϵ, of the system and the flow velocity, c, as $\tau = \frac{\epsilon}{c}$.

Parameter Selection

To select the ideal parameters for the 1D model, we optimize our three performance criteria. The parameters involved are the physical parameters $(P_0 - P_l)$, c, and L and the dimensionless parameters u_{max} and $\Delta\xi$, which are dependent on Pe, S_1 and S_2. In order to maximize the maximum drop in PO_2, u_{max} has to be maximized. Fig 4.3 shows u_{max} as a function of Pe for different values of S_1 and S_2. From Fig 4.3, u_{max} is maximized as $Pe \to 0$, $S_1 \to 0$ and $S_2 \to \infty$. As S_2 increases, u_{max} becomes less sensitive to S_1 and Pe.
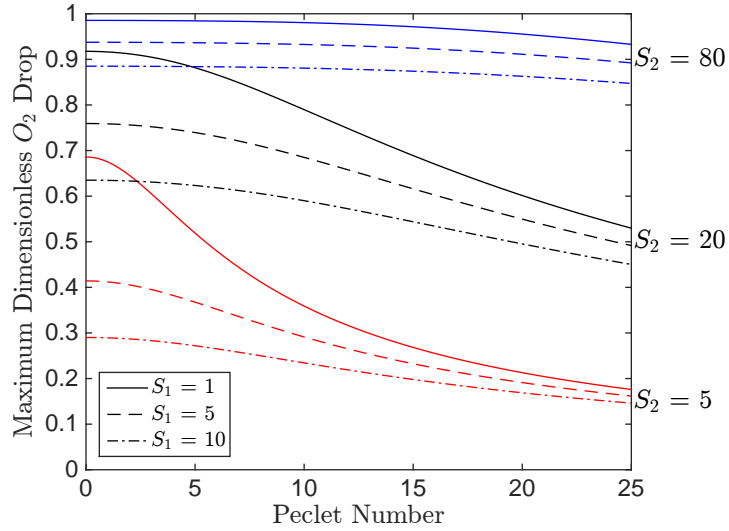
Figure 4.3: Dimensionless O$_2$ Drop *The maximum dimensionless O$_2$ drop, u_{max}, as a function of Péclet number, Pe. The solid, dashed and dot-dashed curves represent S_1 values of 1, 5 and 10, respectively. The red, black and blue curves represent values of S_2 of 5, 20 and 80 respectively.*

In order to maximize the rate of O$_2$ drop, $u_{max}/\Delta\xi$ should be maximized. Fig 4.4 shows $u_{max}/\Delta\xi$ as a function of Pe for varying values of S_1 and S_2. From Fig 4.4, $u_{max}/\Delta\xi$ is maximized for large Pe, small S_1, and large S_2. The effect of S_2 on O$_2$ drop rate is larger than that of S_1.
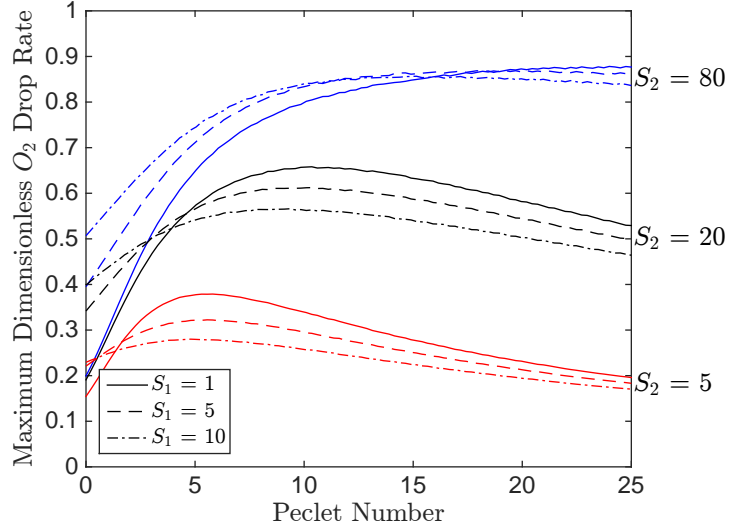
Figure 4.4: Dimensionless Drop Rate *The dimensionless rate of O_2, $u_{max}/\Delta\xi$, as a function of the Péclet number, Pe. The solid, dashed and dot-dashed curves represent S_1 values of 1, 5 and 10, respectively. The red, black and blue curves represent values of S_2 of 5, 20 and 80 respectively.*

To optimize both u_{max} and $u_{max}/\Delta\xi$ a compromise in Pe must be chosen since u_{max} is maximized for small Pe and $u_{max}/\Delta\xi$ is maximized for large Pe. However, since the effects of Pe on u_{max} are small for large S_2, if we can choose large S_2, we can choose the Pe to satisfy the optimization of $u_{max}/\Delta\xi$.

Since we cannot control diffusivity, the dimensionless parameters must be controlled by altering c, L, k_1 and k_2. To minimize S_1, k_1 should be as small as practical; physically this can be achieved by making the walls as thick as possible. To maximize S_2, k_2 should be made as large as possible; this can be achieved by making the spin coat layer as small as possible. $(P_0 - P_l)$ should also be made as large as practical.

The flow velocity, c, affects Pe, $\Delta PO_{2max}/\Delta t$ and the temporal resolution, τ. All three parameters are optimized with a larger c. The effect of window length, L_w, is less straightforward since it effects the dimensionless parameters and $\Delta PO_{2max}/\Delta t$. S_1 and S_2 are sensitive to L_w since they are related quadratically, and since they have opposite optima,

care must be taken while choosing the length of the exchange window. The effect of the window length will be explored with the 3D model.

4.2.2 Computational Model

Mesh Generation

The geometry construction and mesh generation were performed using the open source software GMSH [25]. The same mesh was used for both the fluid dynamics simulations and the mass transfer simulations.

For each geometry, a hybrid mesh was used, with structured regions in the flow channels and an unstructured region in the PDMS area (which is far from the region of interest) to reduce the number of elements. Element sizes were decreased until the solution no longer changed with mesh resolution. The resulting meshes varied between simulations, but typically the smallest elements (located in the RBC channel) were on the order of 0.01 mm, and the largest elements (located in the PDMS) were 0.5-1.0 mm.

Fluid Dynamics Simulations

The flow in both channels were assumed to be Newtonian, incompressible and isothermal. The blood was assumed to be a single homogeneous fluid. The resulting steady-state equations for flow in both channels are given by:

$$\nabla \cdot \vec{v}_i = 0 \tag{4.6a}$$

$$\rho_i \vec{v}_i \cdot \nabla \vec{v}_i = \mu_i \nabla^2 \vec{v}_i - \nabla p \tag{4.6b}$$

where $\vec{v}_i$, ρ_i, μ_i are the velocity, density and dynamic viscosity of the fluid respectively and p is the hydrodynamic pressure in the fluid. The subscripts $i = g, p, rbc$ refer to the

gas, plasma and red blood cells. Since the blood is assumed to be homogeneous $\vec{v}_p = \vec{v}_{rbc}$, $\rho_p = \rho_{rbc}$ and $\mu_p = \mu_{rbc}$.

Eq 4.6a and 4.6b were solved numerically using open source software OpenFOAM [26]. The software discretizes the equations using a finite volume method and solves the coupled system of equations using the Semi-Implicit Method for Pressure Linked Equations [27].

Mass Transfer Simulations

The following equations were used to model the oxygen transport throughout the microfluidic device [28]:

$$D_{pdms}k_{pdms}\nabla^2 PO_2 = 0 \qquad\qquad \in \Omega_{pdms} \qquad (4.7a)$$

$$k_g\vec{v}_g \cdot \nabla PO_2 = D_g k_g \nabla^2 PO_2 \qquad\qquad \in \Omega_g \qquad (4.7b)$$

$$\left[(1 - Ht)k_p\vec{v}_p + Ht\left(k_{rbc} + [Hb_T]\frac{dSO_2}{dPO_2}\right)\vec{v}_{rbc}\right] \cdot \nabla PO_2 =$$
$$D_p k_p \nabla^2 PO_2 \qquad\qquad \in \Omega_{rbc} \qquad (4.7c)$$

where D_i, k_i, PO_2, Ht, and $[Hb_T]$ are the diffusivity, solubility, oxygen partial pressure, hematocrit and total heme concentration of the blood respectively. The different regions of the device are designated by Ω_j, where the subscripts $j = pdms, g, rbc, p$ represent the PDMS, gas, red blood cells and plasma respectively. The derivative $\frac{dSO_2}{dPO_2}$ can be found from the Hill equation [29]:

$$SO_2 = \frac{PO_2^N}{P_{50}^N + PO_2^N} \qquad (4.8)$$

where SO_2 is hemoglobin oxygen saturation, N is the Hill coefficient and P_{50} is the partial pressure of oxygen at 50% saturation.

Eqs 4.7a-c were discretized using in-house software that utilizes a stabilized Galerkin finite element method programmed in C++; a least squares stabilizer was used in the convective regions of the domain [30]. The resulting non-linear system of equations were iteratively linearized and solved with the Generalized Minimal Residual Method [31]. Convergence was verified for the extreme cases by refining the mesh to be sure that the solution was independent of the choice of discretization. All simulations were run on a personal computer with an 8 core 4.2 GHz processor with 16 GB of RAM. Simulation times were less than an hour on one core.

To quantify the O_2 exchange in the 3D model we define the weighted drop in PO_2 by the following,

$$WD = max_{PO_2 \in x} \frac{1}{W_r} \int_{z=-\frac{W_r}{2}}^{z=\frac{W_r}{2}} \int_{y=y_0}^{y=y_0+H_r} PO_2(x,y,z)e^{-\mu(y-y_0)}dydz \qquad (4.9)$$

where W_r and H_r are the width and height of the RBC channel, respectively, y_0 is the location of the bottom of the channel and μ is the optical attenuation of blood plasma. This is a weighted integral of the PO_2 along the depth of the channel (y-direction) to give a stronger weighting to the PO_2 values closer to the bottom of the channel since that is where the detector will be located. It is then averaged across the width of the channel (z-direction) and the maximum value is taken along the stream-wise direction (x-direction).

The spatial drop time is quantified in the same way as for the 1D model; the 3D profile is reduced to one dimension by using the same weighted integral in y and taking the centreline in z.

4.3 Results

To investigate the effects of 3D geometric features, we simulated the O_2 transport in the microfluidic device for various dimensions of the RBC channel. In particular, we varied cross-sectional area of the RBC channel, as well as its aspect ratio to capture the effects of channel cross-section. In addition, we varied the length of the exchange window to determine how the O_2 drop and its rate are affected. We also varied spin-coat thickness to determine how important it is for our particular geometry and physical conditions. Fig 4.5 shows a specific solution of the 3D model using the parameters in Table 4.1; this figure shows the weighted centreline profile.

Parameter	Value
Baseline Oxygen Partial Pressure ($mmHg$)	160
Gas Oxygen Partial Pressure ($mmHg$)	0
Diffusivity of Oxygen in Nitrogen (mm^2/s)	17.6
Solubility of Oxygen in Nitrogen ($\mu M/mmHg$)	5.342105
Solubility of Oyxgen in RBCs ($\mu M/mmHg$)	1.47
Diffusivity of Oxygen in Plasma (mm^2/s)	0.00275
Solubility of Oxygen in Plasma ($\mu M/mmHg$)	1.33
Diffusivity of Oxygen in PDMS (mm^2/s)	0.00355
Solubility of Oxygen in PDMS ($\mu M/mmHg$)	17.959
Total Heme Concentration (μM)	5350
Oxygen Partial Pressure at 50 % Saturation (mmHg)	37
Hill Coefficient	2.7
Hematocrit	0.1

Table 4.1: *Model Parameters*

First, the cross-sectional area of the RBC channel was varied maintaining a constant mean velocity. The channels simulated were square in cross-section ranging from 100x100 μm^2 to 500x500 μm^2. The maximum drop in PO$_2$ increased with increasing cross-sectional area (see Fig 4.6). This appears to be due to the increased surface area for exchange as well as the increased volume in the channel contributing to the weighted drop. In contrast, rate of drop decreases with area. This is likely due to the increasing volume of the RBC channel.
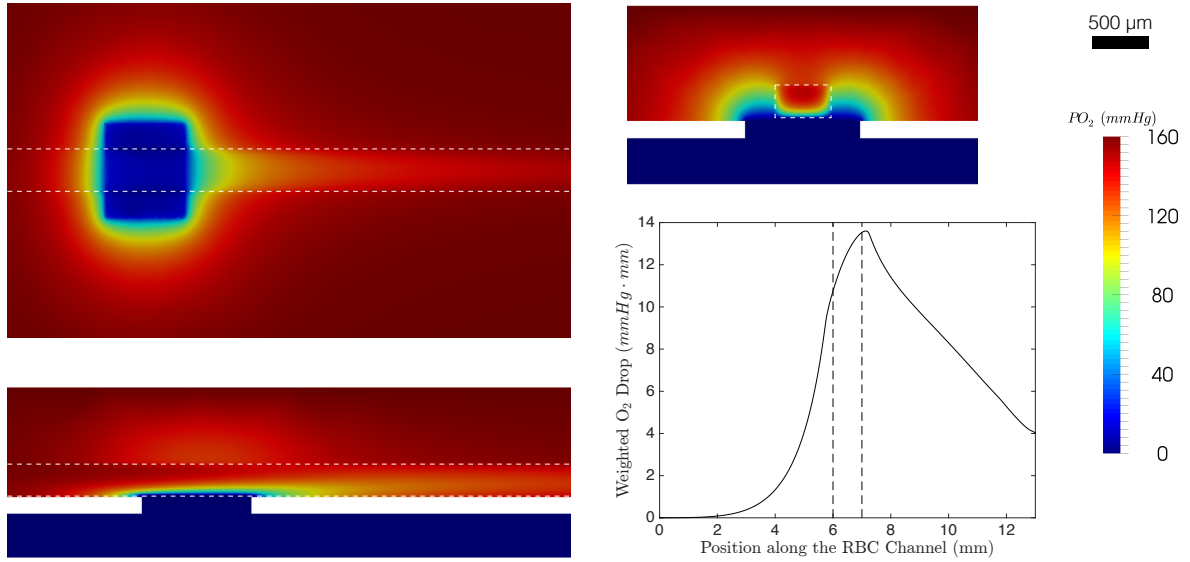
Figure 4.5: Solution to the 3D model *The top left colormap shows the y-normal plane close to the bottom edge of the channel (y = 0.5775). The bottom left colormap shows the z-normal plane through the center of the geometry. The colormap on the top right shows the x-normal plane through the center of the geometry. The white dashed line indicates the RBC channel. The plot in the bottom right shows the weighted centreline drop in PO_2. The black dashed line indicates the location of the exchange window.*

From Fig 4.7, channels with smaller height to width ratio perform better at dropping the O_2 compared to short, wide channels of the same area. This is due to multiple factors: first, the channels that are taller have more volume contributing to the weighted drop (see Eq 4.9). Second, the taller channels are thin, allowing the more surface area on their sides to be exposed to low O_2. Fig 4.8 shows colour maps for the two extreme cases. The change in drop rate follows the same trend as with the weighted drop.

Increasing the length of the window causes an increased drop in PO_2 and an increased drop rate (see Fig 4.9). The increase in PO_2 drop can be explained by having a longer window, exposing more of the channel to low O_2.

Increasing the spin-coat layer thickness causes a decrease in the drop in PO_2; this relationship is approximately linear. The change in drop rate follows a similar trend to the drop in O_2 (see Fig 4.10). In terms of the 1D model, increasing the spin-coat thickness increases
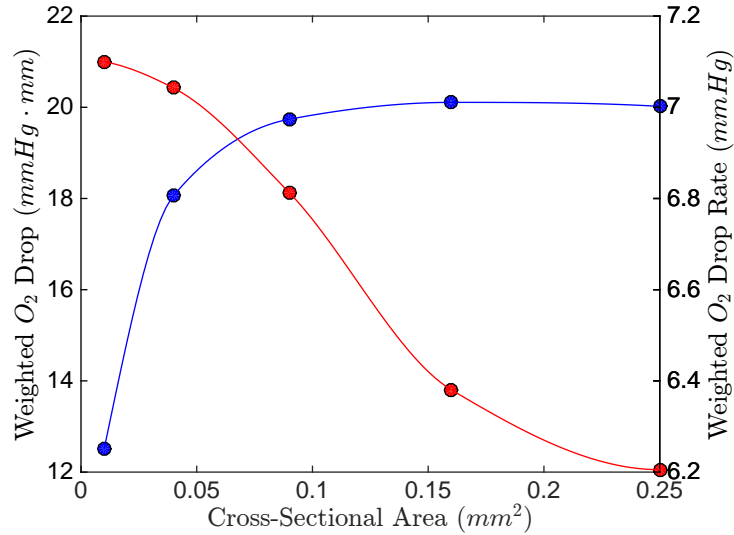
Figure 4.6: Effect of RBC Channel Cross Sectional Area *The weighted O_2 drop (blue) and weighted O_2 drop rate (red) as a function of RBC channel cross-sectional Area. The channels simulated are square in cross-section.*

S_2, which causes a smaller drop in O_2 and a smaller drop rate (see Figs 4.3 and 4.4); this trend agrees with our 3D results. Hematocrit has negligible effect on both the weighted drop and the drop rate (Fig 4.11).

4.4 Discussion

Ellsworth *et al* suggested that ATP release time is less than 500 milliseconds [32] based on the RBC transit time in an isolated arteriole preparation exposed to low oxygen levels. Based on this estimate, we require a system with a resolution on the order of milliseconds. Wan et al measured shear-dependent ATP release time and reports it to be on the order of 25-75 milliseconds [24]. If the mechanisms responsible for ATP release are similar for both shear-dependent and O_2-dependent release, then we expect, ATP release time to be similar to the value measured in their study. Understanding the time course for ATP release from RBCs is important since it determines where in the vasculature ATP is released and where the vessels will sense ATP. Further, many inflammatory diseases have been associated with
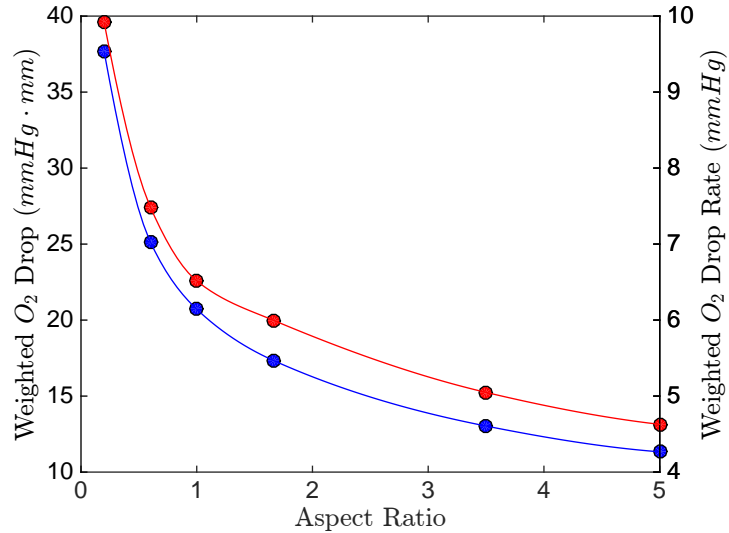
Figure 4.7: Effect of RBC Channel Aspect Ratio *The weighted O_2 drop (blue) and weighted O_2 drop rate (red) as a function of RBC channel aspect ratio (width:height). The area of the channels simulated was held constant (0.15 mm^2).*

impaired ATP release, thus a measurement of ATP release dynamics could be used to screen for these diseases.

In previous work, we showed the feasibility of using steady-state flow to measure the dynamics of SO_2-dependent ATP release *in vitro* [23]. This work was based on an ideal device in order to test the viability of the concept. We demonstrated two important design criteria, first, that the device was able to cause a sufficient drop in O_2 and second, that we were able to recover time-dependent changes in the ATP signal. Although this study was able to show the feasibility of our device, the idealized design described in this article was not practical to fabricate.

With the practical considerations in mind, we developed a simple 1D model of oxygen transport in our device in order to qualitatively evaluate some of the simulation parameters to reduce the number of simulations required to determine the optimal design for our application. The 1D model is an idealization of the device and does not account for geometric information such as the RBC channel's cross-section dimensions, though some of the ge-
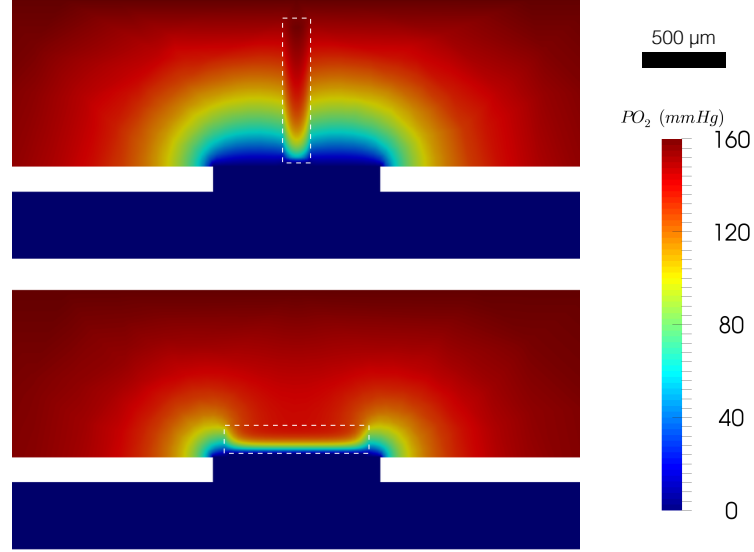
Figure 4.8: Simulation of RBC Channel Aspect Ratios *The PO_2 solution showing the x-normal plane through the center of the geometry for two different aspect ratios. The colormap on the top shows the simulation results for a channel with 1:5 width to height ratio. The colormap on the bottom shows the simulation results for a channel with a 5:1 width to height ratio. The white dashed line indicates the RBC channel.*

ometric information is embedded in the model parameters, such as PDMS thickness. To compare the performance of the 1D model against our 3D simulations, we show the weighted O_2 drop predicted by the 1D model for varying exchange window lengths and PDMS spin coat thicknesses (see Fig. 4.12).

The 1D model predicts the O_2 drop to level off and reach a steady value as the exchange window length increases. The 3D model predicts the O_2 drop to increase with increasing window length, though for the parameters used, the simulation results do not reach a steady drop. Further, the value of the drop is considerably lower than predicted by the 1D model. Considering the PDMS spin coat thickness, the 1D model predicts the O_2 drop to approach zero as the thickness increases; the O_2 drop is predicted to approach the maximum drop as the thickness approaches zero. Comparing these results to the 3D simulations, the O_2 drop is substantially lower than predicted by the 1D model and does not begin to level off for the lowest thickness simulated. While the 1D model predictions appear reasonable, the O_2 drop is overestimated compared to the 3D model and is more sensitive to the variations in
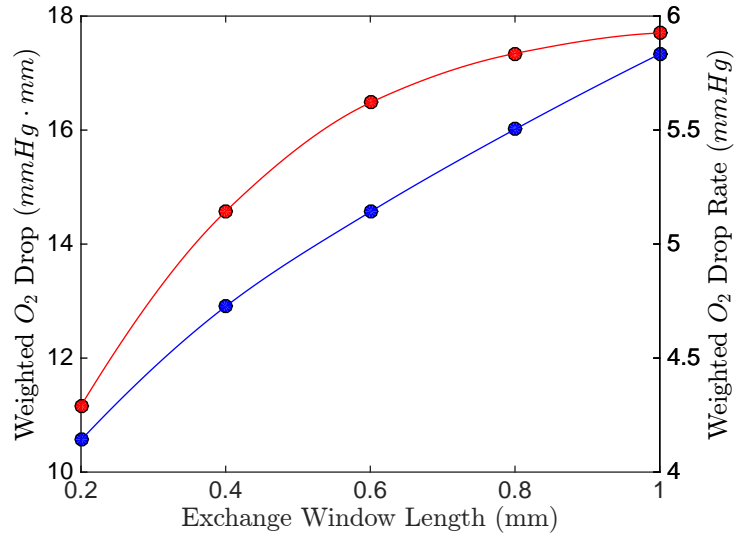
Figure 4.9: Effect of Exchange Window Length *The weighted O_2 drop (blue) and weighted O_2 drop rate (red) as a function of exchange window length.*

the geometric parameters.

The 1D model approaches the 3D model as the RBC channel becomes infinitely wide and its height becomes infinitesimally small. It assumes cross-stream diffusion in the RBC flow is negligible and diffusion in the PDMS occurs only vertically. Further, the 1D model also assumes that the fluid velocity in the gas channel is infinite, so that the low oxygen is maintained at the gas channel side of the exchange surface. Due to these simplifications, the 1D model overestimates the drop in O_2; these simplifications also account for the increased sensitivity of the geometric parameters. Although the 1D model does not accurately account for the O_2 content in the device, it allows us to qualitatively determine the behaviour of changing certain parameters. Also, since the model can be solved analytically, we can simulate a large range and achieve practically continuous information. Therefore, the 1D analytical model is a useful tool for qualitatively understanding the physical details of our system, but a 3D model is required to quantify the extent of the behaviour.

Though the 1D model was useful in helping us determine how the O_2-permeable walls will
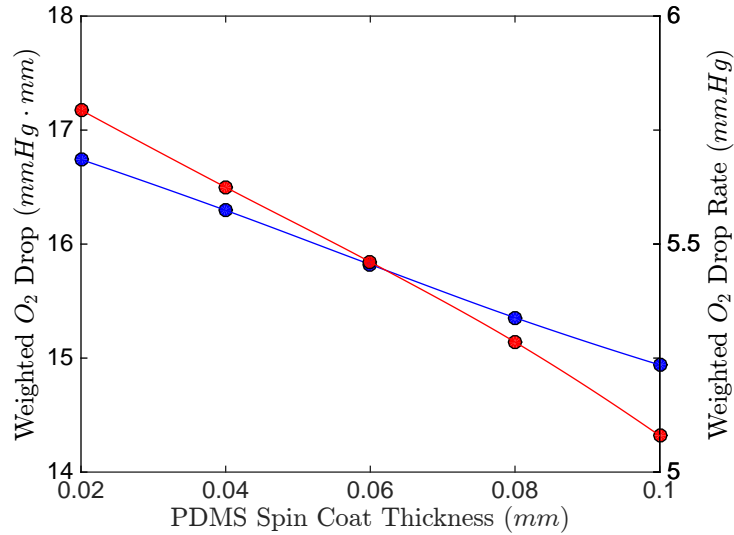
Figure 4.10: Effect of Spin Coat Thickness *The weighted O_2 drop (blue) and weighted O_2 drop rate (red) as a function of PDMS spin-coat thickness.*

affect the O_2 exchange, it fails to capture some of the important 3D features. Thus, we used a 3D model to explore how the O_2 exchange is affected when we have a channel of finite cross-section and diffusion around the sides of the RBC channel from the exchange window and outside surfaces.

The first 3D aspect of the device geometry we look at is the RBC channel's cross-section. From Fig 4.6, it is clear that there is an optimal cross-sectional area. Channels with larger cross-sectional areas have larger surface areas, leading to more area for the exchange. However, the exchange is limited to the lower walls of the channel since the exchange window is on the bottom. For the larger channels, the width of the window limits how much of the side walls' surface area is exposed to the low levels of O_2. If we now allow the channel to increase in surface area, but not get any wider, we can optimize the amount of surface area exposed to the low levels of oxygen; this is demonstrated in Figs 4.7 and 4.8. In contrast our previous results showed channels that are less deep are more beneficial since the drop extends across the whole channel [23]. However, this was because the 2D model in [23] assumes that the channel and window are infinitely wide; thus, it neglects the effect of low oxygen on the sides of the channel.
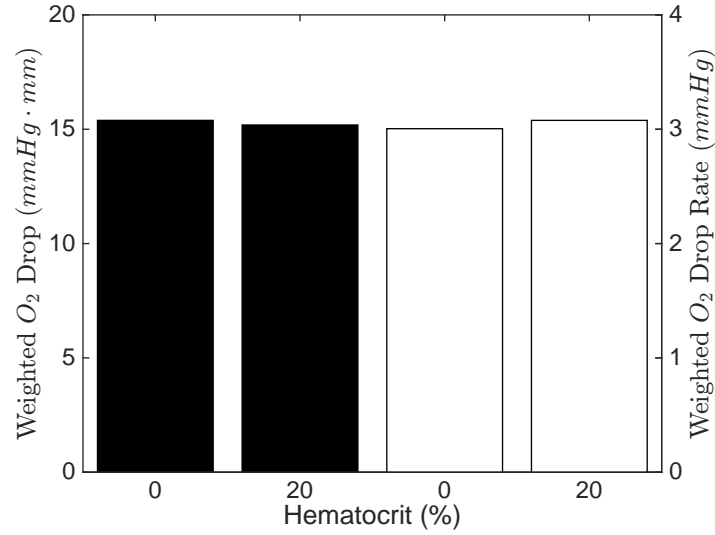
Figure 4.11: Effect of Hematocrit *The weighted O_2 drop (black bars) and weighted O_2 drop rate (white bars) for 0% and 20% hematocrit. A negligible effect is shown for both.*
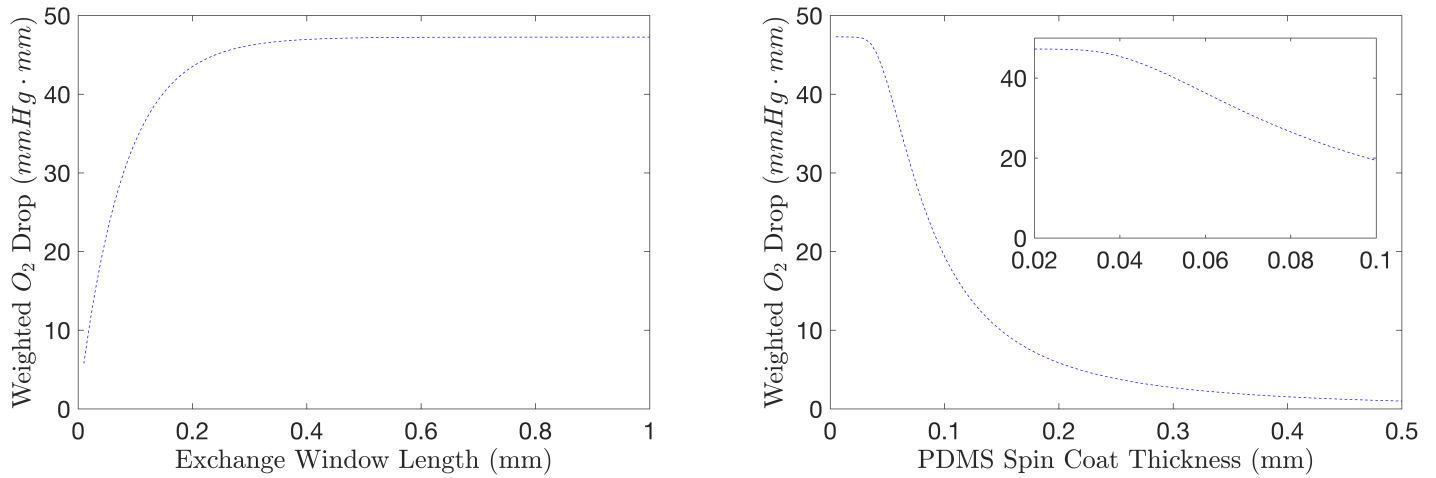
Figure 4.12: 1D Model Prediction of Geometric Parameters *Weighted O_2 drop was simulated using the 1D model to determine the effect of varying exchange window length (left) and PDMS spin-coat thickness (right). The inset in the right panel shows the parameter range used in the 3D simulations. The results of the simulations were re-dimensionlized in order to be comparable to the 3D simulation results (see Fig. 4.9 and 4.10). Note: the parameters range used in the 3D simulations for the exchange window length was 0.1-1.*

In the 1D model, the length of the window is the characteristic length. Thus it not only effects O_2 exchange through Equation 4.5, but it also effects u_{max} and $u_{max}/\Delta\xi$ through the dimensionless parameters. From Fig 4.9, we see that having a longer window is better for both the drop and the drop rate of O_2. The benefits of longer windows will become less important as O_2 in the channel approaches zero. Practically, a very large exchange window will result in a structurally weak device; the thin PDMS layer separating the RBC and gas channel may rupture or deform. Therefore, the exchange window should be large enough to cause a sufficient drop in oxygen, but not so long that the device becomes structurally compromised.

The 1D model indicates that the ideal device would have an infinitely thin spin-coat layer. However, practically, we need a barrier that closes the RBC channel so that it does not leak; thus it has to be thick enough so that it does not rupture under the pressure of the flow. Physically, we can fabricate spin-coat thicknesses on the order of 20 μm and these channels do not rupture under the pressure of the flow. From Fig 4.10, we can see that in the range of practical spin-coat sizes (20-100 μm), the spin-coat thickness does not affect the O_2 exchange substantially. Therefore, small variability in the thickness of the spin coat layer will not affect the effectiveness of the device.

Interestingly, hematocrit has only a small effect on the O_2 exchange in our device. From Fig 4.11, we can see that lower hematocrit is better for exchange, though, the change is not large. An important point to consider is that larger hematocrit will result in more RBCs available to release ATP, increasing the amount of signal coming form the system. However, the amount of RBCs affects the optics of the system since they absorb visible light. Therefore, we should use a hematocrit that is large enough to attain a measurable ATP signal, but not so large that all the signal is attenuated by the cells. We considered this effect in a previous study [23].

In this study, we did not simulate every possible geometric parameter, such as the length of the RBC channel, the height of the PDMS around the channel, the width of the window, and the dimensions of the gas channel. We no not expect the length of the RBC channel to be too important for exchange. For the purposes of the analysis of the experimental results, the flow should be fully developed. Therefore the channel should be longer than the entrance length, though at the flow rates typically used in microfluidics, the entrance lengths are quite small (on the order of 3-30 μm). As for oxygen exchange in shorter channels, the drop will be smaller since the source of oxygen is closer to the exchange window. This will also result in a steeper rate. However, these effects are only important for channels on the order of the entrance length.

Practically, the exchange window cannot exceed a width of 1 mm due to the risk of the PDMS spin-coat deforming into the window causing distortion to the optical image. Intuitively, wider windows will improve exchange since there will be more area for exchange, though the effect will become insignificant as the window becomes much wider than the channel. From the 1D model, we expect more PDMS around the RBC channel to be better as this decreases the effective permeability of the walls. However, if there is too much PDMS above the channel, there may be optical problems.

This study focuses on the ability of the proposed microfluidic device to cause a drop of PO_2 in a flowing RBC suspension. However, the main goal of this device is to measure the release of ATP from RBCs in response to their SO_2. The relationship between PO_2 and SO_2 is modelled by the Hill equations (Equation 4.8). Fig 4.13 shows the Hill equation for human RBCs. This figure demonstrates that for low and high PO_2, large changes in PO_2 are required to change saturation. In contrast, in the mid-range of PO_2, only small changes in PO_2 are required to produce large changes in SO_2. Since the RBCs in our simulation span PO_2 values from zero to 160, we expect our device to almost fully desaturate the RBCs.
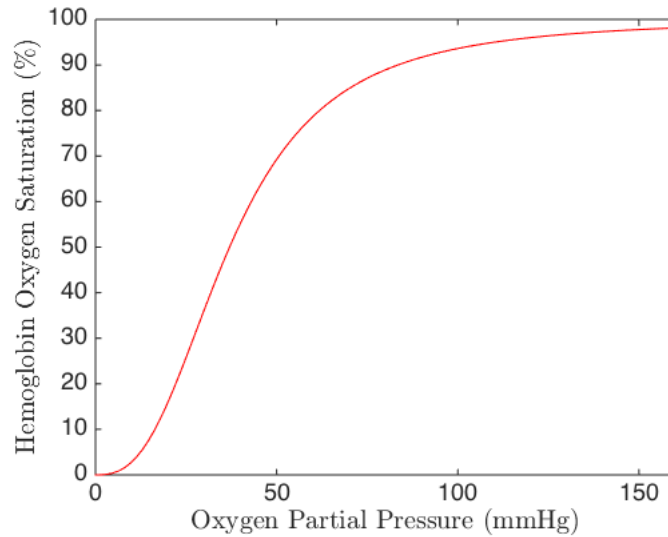
Figure 4.13: Hemoglobin Binding Curve *Hemoglobin oxygen saturation as a function of partial pressure determined by the Hill equation.*

The ideal device should have a low width to height ratio with a large area such that the width of the channel is much less than that of the exchange window. The device should have a spin-coat layer that is thin as possible, while still being able to withstand the flow pressure The exchange window should be long enough, but not so long that though it that the spin-coat layer sinks into the window. The hematocrit should be chosen to get a large enough signal from the ATP but small enough to not lose light from attenuation. The weighted centreline PO_2 and SO_2 drop are shown in Fig 4.14.

Microfluidic devices have become increasingly popular for use in biological studies due to their reduced sample consumption, relative low costs and length scales that are comparable to dimensions on the cellular level. Microfluidic devices are used in a wide range of biological applications including hemodynamics at the microvascular scale [33–35] and cell behaviour under shear stress [24, 36, 37]. Microfluidic devices can be used to establish gradients of small molecules [38–41]. Further, in recent years, microfluidic devices have been used to create micro-scale cell cultures that mimic *in vivo* micro-environments to study physiological tissue interactions [42–45]. Due to their vast applications in biological settings, microfluidic
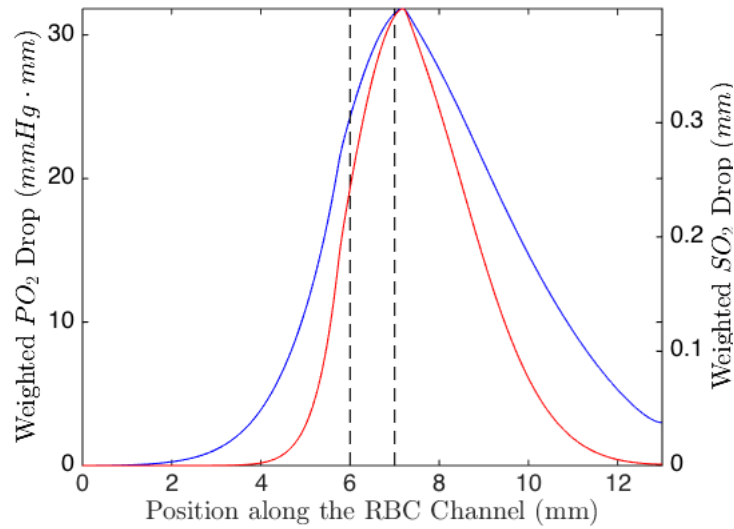
Figure 4.14: Simulation of Ideal Design *The ideal device was simulated with channel height of 0.5 mm and width of 0.3 mm, a 0.02 mm spin coat and a 1 mm long exchange window. This figure shows the weighted centreline drop in PO_2 (blue) and the weighted centreline SO_2 (red) as a function of position along the RBC channel. The black dashed line indicates the location of the exchange window.*

devices must be designed to meet the oxygen requirements of the study. Living cells are highly sensitive to the oxygen levels in their environment and may behave irregularly when exposed to unphysiological levels [46–48]. And since the results of our study demonstrate the crucial role that geometry can play in oxygen transport, it is an important consideration for the design of microfluidic channels. Our methods can also be applied to other gases and solutes as well as temperature.

Various studies have implemented mathematical models in order to validate and optimize microfluidic designs [14–16, 18, 19]. In these studies, the use of mathematical modelling was necessary for ensuring the proper distribution of oxygen in their application. Some of these studies considered only 2D models of their devices [14–16], while others used 3D models [18, 19]. In the studies that employed 2D models, 2D geometry was often sufficient to approximate the overall transport due to inherent symmetries in the device. In our application, a 3D geometry was crucial for two reasons. First, our device possessed two stream-wise directions (gas flow direction and RBC flow direction). Further a 2D model

would not allow us to vary parameters that lay orthogonal to the plane that was being modelled.

In conclusion, although the 1D model provided important qualitative insights, the 3D model demonstrated that diffusion through the PDMS surrounding the RBC channel yielded unexpected relationships important to the design of the device. Thus the use of a 3D transport model is crucial for guiding our optimal design.

References

[1] R. J. Sové, G. M. Fraser, D. Goldman, and C. G. Ellis, "Finite element model of oxygen transport for the design of geometrically complex microfluidic devices used in biological studies," *PLOS ONE*, vol. 11, no. 11, p. e0166289, 2016.

[2] M. L. Ellsworth, T. Forrester, C. G. Ellis, and H. H. Dietrich, "The erythrocyte as a regulator of vascular tone," *American Journal of Physiology-Heart and Circulatory Physiology*, vol. 269, no. 6, pp. H2155–H2161, 1995.

[3] D. J. Fischer, N. J. Torrence, R. J. Sprung, and D. M. Spence, "Determination of erythrocyte deformability and its correlation to cellular ATP release using microbore tubing with diameters that approximate resistance vessels in vivo," *Analyst*, vol. 128, no. 9, pp. 1163–1168, 2003.

[4] G. Bergfeld and T. Forrester, "Release of ATP from human erythrocytes in response to a brief period of hypoxia and hypercapnia," *Cardiovascular Research*, vol. 26, no. 1, pp. 40–47, 1992.

[5] D. B. Light, T. L. Capes, R. T. Gronau, and M. R. Adler, "Extracellular ATP stimulates volume decrease in Necturus red blood cells," *American Journal of Physiology-Cell Physiology*, vol. 277, no. 3, pp. C480–C491, 1999.

[6] J. E. Jagger, R. M. Bateman, M. L. Ellsworth, and C. G. Ellis, "Role of erythrocyte in regulating local O2 delivery mediated by hemoglobin oxygenation," *American Journal of Physiology-Heart and Circulatory Physiology*, vol. 280, no. 6, pp. H2833–H2839, 2001.

[7] H. H. Dietrich, Y. Kajita, and R. Dacey, "Local and conducted vasomotor responses in isolated rat cerebral arterioles," *American Journal of Physiology-Heart and Circulatory Physiology*, vol. 271, no. 3, pp. H1109–H1116, 1996.

[8] M. L. Ellsworth, C. G. Ellis, D. Goldman, A. H. Stephenson, H. H. Dietrich, and R. S. Sprague, "Erythrocytes: oxygen sensors and modulators of vascular tone," *Physiology*, vol. 24, no. 2, pp. 107–116, 2009.

[9] C. G. Ellis, S. Milkovich, and D. Goldman, "What is the efficiency of atp signaling from erythrocytes to regulate distribution of o2 supply within the microvasculature?," *Microcirculation*, vol. 19, no. 5, pp. 440–450, 2012.

[10] R. M. Bateman, M. D. Sharpe, J. E. Jagger, and C. G. Ellis, "Sepsis impairs microvascular autoregulation and delays capillary response within hypoxic capillaries," *Critical Care*, vol. 19, no. 1, pp. 1–14, 2015.

[11] C. G. Ellis, D. Goldman, M. Hanson, A. H. Stephenson, S. Milkovich, A. Benlamri, M. L. Ellsworth, and R. S. Sprague, "Defects in oxygen supply to skeletal muscle of pre-diabetic ZDF rats," *American Journal of Physiology-Heart and Circulatory Physiology*, vol. 298, no. 6, pp. H1661–H1670, 2010.

[12] R. S. Sprague, A. H. Stephenson, E. A. Bowles, M. S. Stumpf, and A. J. Lonigro, "Reduced expression of Gi in erythrocytes of humans with type 2 diabetes is associated with impairment of both cAMP generation and ATP release," *Diabetes*, vol. 55, no. 12, pp. 3588–3593, 2006.

[13] C. Li, W. Chaung, C. Mozayan, R. Chabra, P. Wang, and R. K. Narayan, "A new approach for on-demand generation of various oxygen tensions for in vitro hypoxia models," *PloS one*, vol. 11, p. e0155921, May 2016.

[14] M. Zahorodny-Burke, B. Nearingburg, and A. L. Elias, "Finite element analysis of oxygen transport in microfluidic cell culture devices with varying channel architectures, perfusion rates, and materials," *Chemical Engineering Science*, vol. 66, pp. 6244–6253, Dec. 2011.

[15] M.-C. Kim, R. H. W. Lam, T. Thorsen, and H. H. Asada, "Mathematical analysis of oxygen transfer through polydimethylsiloxane membrane between double layers of cell culture channel and gas chamber in microfluidic oxygenator," *Microfluidics and Nanofluidics*, vol. 15, pp. 285–296, Feb. 2013.

[16] T.-Y. Kang, J. M. Hong, J. W. Jung, J. J. Yoo, and D.-W. Cho, "Design and assessment of a microfluidic network system for oxygen transport in engineered tissue," *Langmuir*, vol. 29, pp. 701–709, Jan. 2013.

[17] S. C. Oppegard and D. T. Eddington, "A microfabricated platform for establishing oxygen gradients in 3-D constructs," *Biomedical Microdevices*, vol. 15, pp. 407–414, Jan. 2013.

[18] L. Wang, W. Liu, Y. Wang, J.-c. Wang, Q. Tu, R. Liu, and J. Wang, "Construction of oxygen and chemical concentration gradients in a single microfluidic device for studying tumor cell–drug interactions in a dynamic hypoxia microenvironment," *Lab on a Chip*, vol. 13, no. 4, pp. 695–705, 2013.

[19] Y.-A. Chen, A. D. King, H.-C. Shih, C.-C. Peng, C.-Y. Wu, W.-H. Liao, and Y.-C. Tung, "Generation of oxygen gradients in microfluidic devices for cell culture using spatially confined chemical reactions," *Lab on a Chip*, vol. 11, no. 21, pp. 3626–3633, 2011.

[20] H. E. Abaci, R. Devendra, R. Soman, G. Drazer, and S. Gerecht, "Microbioreactors to manipulate oxygen tension and shear stress in the microenvironment of vascular stem and progenitor cells," *Biotechnology and Applied Biochemistry*, vol. 59, pp. 97–105, Mar. 2012.

[21] N. W. Ghonaim, L. W. Lau, D. Goldman, C. G. Ellis, and J. Yang, "A micro-delivery approach for studying microvascular responses to localized oxygen delivery," *Microcirculation*, vol. 18, no. 8, pp. 646–654, 2011.

[22] N. W. Ghonaim, G. M. Fraser, C. G. Ellis, J. Yang, and D. Goldman, "Modeling steady state SO2-dependent changes in capillary ATP concentration using novel O2 micro-delivery methods," *Frontiers in Physiology*, vol. 4, 2013.

[23] R. J. Sové, N. Ghonaim, D. Goldman, and C. G. Ellis, "A computational model of a microfluidic device to measure the dynamics of oxygen-dependent ATP release from erythrocytes," *Plos One*, 2013.

[24] J. Wan, W. D. Ristenpart, and H. A. Stone, "Dynamics of shear-induced ATP release from red blood cells," *Proceedings of the National Academy of Sciences*, vol. 105, no. 43, pp. 16432–16437, 2008.

[25] C. Geuzaine and J.-F. Remacle, "Gmsh: A 3-D finite element mesh generator with built-in pre-and post-processing facilities," *International Journal for Numerical Methods in Engineering*, vol. 79, no. 11, pp. 1309–1331, 2009.

[26] H. G. Weller, G. Tabor, H. Jasak, and C. Fureby, "A tensorial approach to computational continuum mechanics using object-oriented techniques," *Computers in Physics*, vol. 12, no. 6, pp. 620–631, 1998.

[27] S. V. Patankar and D. B. Spalding, "A calculation procedure for heat, mass and momentum transfer in three-dimensional parabolic flows," *International Journal of Heat and Mass Transfer*, vol. 15, no. 10, pp. 1787–1806, 1972.

[28] J. D. Hellums, P. K. Nair, N. S. Huang, and N. Ohshima, "Simulation of intraluminal gas transport processes in the microcirculation," *Annals of Biomedical Engineering*, vol. 24, no. 1, pp. 1–24, 1995.

[29] A. V. Hill, "The possible effects of the aggregation of the molecules of haemoglobin on its dissociation curves," *J Physiol (Lond)*, vol. 40, pp. 4–7, 1910.

[30] J. N. Reddy and D. K. Gartling, *The finite element method in heat transfer and fluid dynamics.* CRC press, 2010.

[31] Y. Saad and M. H. Schultz, "GMRES: A generalized minimal residual algorithm for solving nonsymmetric linear systems," *SIAM Journal on Scientific and Statistical Computing*, vol. 7, no. 3, pp. 856–869, 1986.

[32] H. H. Dietrich, M. L. Ellsworth, R. S. Sprague, and R. G. Dacey, "Red blood cell regulation of microvascular tone through adenosine triphosphate," *American Journal of Physiology-Heart and Circulatory Physiology*, vol. 278, no. 4, pp. H1294–H1298, 2000.

[33] G. Cokelet, R. Soave, G. Pugh, and L. Rathbun, "Fabrication of in vitro microvascular blood flow systems by photolithography," *Microvascular Research*, vol. 46, no. 3, pp. 394–400, 1993.

[34] S. S. Shevkoplyas, S. C. Gifford, T. Yoshida, and M. W. Bitensky, "Prototype of an in vitro model of the microcirculation," *Microvascular Research*, vol. 65, no. 2, pp. 132–136, 2003.

[35] D. J. Quinn, I. Pivkin, S. Y. Wong, K.-H. Chiam, M. Dao, G. E. Karniadakis, and S. Suresh, "Combined simulation and experimental study of large deformation of red blood cells in microfluidic systems," *Annals of Biomedical Engineering*, vol. 39, no. 3, pp. 1041–1050, 2011.

[36] A. K. Price, D. J. Fischer, R. S. Martin, and D. M. Spence, "Deformation-induced release of atp from erythrocytes in a poly (dimethylsiloxane)-based microchip with channels that mimic resistance vessels," *Analytical Chemistry*, vol. 76, no. 16, pp. 4849–4855, 2004.

[37] M. J. Moehlenbrock, A. K. Price, and R. S. Martin, "Use of microchip-based hydrodynamic focusing to measure the deformation-induced release of atp from erythrocytes," *Analyst*, vol. 131, no. 8, pp. 930–937, 2006.

[38] X. Jiang, Q. Xu, S. K. Dertinger, A. D. Stroock, T.-m. Fu, and G. M. Whitesides, "A general method for patterning gradients of biomolecules on surfaces using microfluidic networks," *Analytical Chemistry*, vol. 77, no. 8, pp. 2338–2347, 2005.

[39] S. K. Dertinger, D. T. Chiu, N. L. Jeon, and G. M. Whitesides, "Generation of gradients having complex shapes using microfluidic networks," *Analytical Chemistry*, vol. 73, no. 6, pp. 1240–1246, 2001.

[40] V. V. Abhyankar, M. A. Lokuta, A. Huttenlocher, and D. J. Beebe, "Characterization of a membrane-based gradient generator for use in cell-signaling studies," *Lab on a Chip*, vol. 6, no. 3, pp. 389–393, 2006.

[41] H. Wu, B. Huang, and R. N. Zare, "Generation of complex, static solution gradients in microfluidic channels," *Journal of the American Chemical Society*, vol. 128, no. 13, pp. 4194–4195, 2006.

[42] N. K. Inamdar and J. T. Borenstein, "Microfluidic cell culture models for tissue engineering," *Current Opinion in Biotechnology*, vol. 22, no. 5, pp. 681–689, 2011.

[43] D. Huh, G. A. Hamilton, and D. E. Ingber, "From 3d cell culture to organs-on-chips," *Trends in Cell Biology*, vol. 21, no. 12, pp. 745–754, 2011.

[44] J. El-Ali, P. K. Sorger, and K. F. Jensen, "Cells on chips," *Nature*, vol. 442, no. 7101, pp. 403–411, 2006.

[45] A. M. Ghaemmaghami, M. J. Hancock, H. Harrington, H. Kaji, and A. Khademhosseini, "Biomimetic tissues on a chip for drug discovery," *Drug Discovery Today*, vol. 17, no. 3, pp. 173–181, 2012.

[46] L. Jornot, M. Mirault, and A. Junod, "Protein synthesis in hyperoxic endothelial cells: evidence for translational defect," *Journal of Applied Physiology*, vol. 63, no. 2, pp. 457–464, 1987.

[47] S. P. Sanders, J. L. Zweier, P. Kuppusamy, S. J. Harrison, D. Bassett, E. W. Gabrielson, and J. Sylvester, "Hyperoxic sheep pulmonary microvascular endothelial cells generate free radicals via mitochondrial electron transport.," *Journal of Clinical Investigation*, vol. 91, no. 1, p. 46, 1993.

[48] R. Bjerkvig, J. Thorsen, E. Svendsen, H. Holmsen, and T. Thorsen, "Effects of hyperoxia on human endothelial cell proliferation and morphology in vitro.," *Undersea Biomedical Research*, vol. 19, no. 6, pp. 415–426, 1992.

Chapter 5

Using digital inpainting to estimate incident light intensity for the calculation of red blood cell oxygen saturation from microscopy images[1]

5.1 Introduction

Adequate oxygen supply is crucial to the proper functioning of most tissues in the body, and therefore blood oxygenation is an important indicator of tissue function. For instance, measurements of blood oxygenation have implications for the study of pre-diabetes [1] and sepsis [2–4]. Red blood cells (RBCs) are the primary carriers of oxygen (O_2) in the circulatory system, accounting for approximately 98% of the O_2 carried in the blood [5]. Due to the low solubility of O_2 in blood plasma, O_2 binds with high affinity to the vast quantity of hemoglobin in RBCs. Since most of the O_2 in the blood is bound to the hemoglobin in RBCs, hemoglobin oxygen saturation (SO_2) is an appropriate measure of O_2 content in the blood [5].

---

[1]A version of this chapter has been accepted to the Journal of Biophotonics.

Advances in the accuracy and ease of SO_2 measurements were made when it was recognized that a second, oxygen-independent wavelength could be used to calibrate SO_2 measurements, without the need to calculate optical path lengths and hematocrit. The proposition of using a two-wavelength spectroscopic method to measure SO_2 was first proposed by Matthes *et al.* [6] in 1935, who built an apparatus to measure ear SO_2 . Since then, many methods have been developed based on this principle [5, 7–12]. In particular, Ellsworth *et al.*, 1987 developed a computer-based approach for measuring SO_2 of a single RBC flowing through capillaries in live *in vivo* experiments by using the light intensity measurements along the centerline of vessels. This method was improved by Ellis *et al.* [11, 13] to allow for simultaneous image acquisition at both wavelengths by introducing a second video camera. Further advances were made by Japee *et al.*, 2005 [12], who extended the analysis to full frame images, instead of being limited to single pixel line. Many recent animal studies have relied on these methods to make measurements of SO_2 [1, 4, 14–17].

Theoretically, dual-wavelength SO_2 measurements are calculated from the ratio of optical densities between two wavelengths, as outlined in Ellsworth 1987 [5]. The optical densities can be calculated from:

$$OD = \log_{10}\left(\frac{I_0}{I}\right),$$
(5.1)

where I is the light intensity that was transmitted through the RBCs and I_0 is the incident light. Therefore, SO_2 calculations require not only the measured light intensities, I, at two wavelengths, but also the incident light, I_0, at both wavelengths. Previous researchers [5, 11, 13] have estimated I_0 by using video data to measure the light intensity of the plasma gaps between the RBCs as they travel single file through the capillary. As the RBCs move out of the way, the plasma intensity gives the intensity of the pixels behind the RBC. This can be accomplished algorithmically by calculating the maximum intensity, I_{max} at each

pixel over a specified number of frames, since RBCs absorb more light, and thus have lower intensity values than the plasma. In a maximum intensity image, moving RBCs disappear [18] revealing the plasma light intensity.

The efficacy of I_{max} as an approximation for I_0 is dependent on RBC velocity, the size of plasma gaps, as well as camera exposure time. The RBCs must move quickly enough to show the background tissue, and the plasma gap must be large enough that the camera captures the background light intensity. If the exposure is too long, the RBC can appear blurred throughout the plasma gap, artificially decreasing the size of the plasma gap or absorbing light, thus attenuating I_0. Ensuring that I_{max} captures the incident light intensity at all pixels is controlled by using an appropriate number of frames, a fast frame rate, and a short exposure time. However, I_{max} will fail if there are stationary cells, or if hematocrit is large enough that there are no plasma gaps. Additionally, if the background varies more rapidly than the time between I_0 estimations, I_{max} will be a poor estimation of I_0; this will be more problematic when slow RBC velocities require a large number of frames to calculate I_{max}. In general, provided we can use a small number of frames, I_{max} is a good estimation of I_0 for digital cameras with high signal to noise ratio (SNR) under the acquisition conditions.

In this study, we propose an alternate, and complementary method for estimating I_0 that does not suffer from the aforementioned deficiencies, through the use of digital inpainting. Digital inpainting is an image processing technique used to estimate missing information in an image. In this paper we demonstrate the use of inpainting to determine the incident light intensity to calculate SO_2. Specifically, we will compare two different inpainting methods to the method currently employed in the literature to estimate the incident light intensity.

5.2   Methods

5.2.1   Maximum Intensity Images

The maximum intensity images, I_{max}, were calculated by determining the maximum intensity of each pixel over a specified number of frames, expressed as a time, Δt. This method is modified from methods presented in the literature [5, 11, 18, 19] which approximate I_0 as $I_{max} - 3\sigma$, where σ is the standard deviation of the intensity over time. However, the cost of calculating σ is relatively large, so with the advent of low-noise digital cameras, it is sufficient to use I_{max} [1, 4, 14–17].

5.2.2   Inpainting

Digital inpainting is traditionally used to remove unwanted features from images using global and/or local image information [20–22]. Many inpainting methods are based on solving partial differential equations (PDEs) using the surrounding pixel intensity values as fixed-value boundary conditions. Analogies are often made to mass transport in order to derive the PDE for inpainting. To estimate I_0, we considered two inpainting methods, the first based on diffusion and the second on convection.

Diffusion-Based Inpainting

An inpainting method based on simple diffusion would solve Laplace's equation with fixed-value boundary conditions representing steady-state diffusion:

$$\nabla^2 I_0^d = 0 \qquad \in \Omega \tag{5.2a}$$

$$I_0^d = I \qquad \in \partial\Omega \,, \tag{5.2b}$$

where I_0^d is the diffusion-based in-painted image, Ω is the inpainting domain, $\partial\Omega$ is the inpainting boundary and I is the original image (see, e.g., [23]).

This equation can be solved numerically using a number of well-known schemes. In this study, Equation 5.2 was discretized using the second-order central difference scheme, and the system was then solved using the Gauss-Seidel method with successive over-relaxation.

Inpainting based on simple diffusion has a tendency to blur sharp features, and for this reason, anisotropic diffusion is often used [22]; these methods use a diffusion coefficient that depends on the gradient of the image. However, we suspect simple diffusion will perform sufficiently well when the image has a relatively homogeneous background, which is often the case for our application.

Convection-Based Inpainting

An inpainting method based on convection would solve:

$$\vec{c} \cdot \nabla I_0^c = 0 \qquad \in \Omega \tag{5.3a}$$

$$I_0^c = I \qquad \in \partial\Omega \,, \tag{5.3b}$$

where I_0^c is the convection-based in-painted image, I is the original image and $\vec{c}$ is a vector field that dictates the direction of convective transport. For this study, the direction field was chosen as a modification to the coherence direction of the image as described in Bornemann and Marz 2007 [24]. Figure 5.1 shows the coherence direction (in white) of a 40x *in-vivo* microscopy image of capillaries and other microvessels in skeletal muscle.
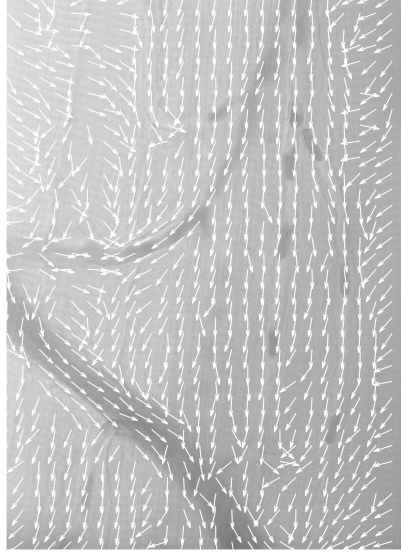
Figure 5.1: *Modified coherence direction of 40x in-vivo microscopy image of a capillary network in rat skeletal muscle (extensor digitorum longus).*

The modified coherence direction of an image can be calculated from the eigenvector corresponding the smallest eigenvalue of the matrix described by the modified structure tensor of the image. The modified structure tensor can be calculated as:

$$J = \frac{G_\rho \star (\mathbb{1}_\Gamma \nabla u_\sigma \otimes \nabla u_\sigma)}{G_\sigma \star \mathbb{1}_\Gamma} \tag{5.4a}$$

$$u_\sigma = \frac{G_\sigma \star (\mathbb{1}_\Gamma I)}{G_\sigma \star \mathbb{1}_\Gamma}, \tag{5.4b}$$

where $\star$ denotes convolution, $\otimes$ denotes the tensor product, I is the known image intensities, $\mathbb{1}_\Gamma$ is the indicator function describing the region that has already been inpainted and G_σ is a Gaussian with mean 0 and standard deviation of σ.

In order to solve this non-linear convection problem rapidly, we discretize and solve the PDE using a fast-marching scheme as described in various studies [24–26]. A fast-marching scheme is solved by calculating each point in the domain sequentially following a specified order. The value at each point, $\vec{x}$, in the inpainting domain can be calculated by a weighted

sum of the neighbouring values that have already been calculated,

$$I_0^c(\vec{x}_k) = \sum_{nb} w(\vec{x}_k, \vec{x}_{nb}) I_0^c(\vec{x}_{nb}), \tag{5.5}$$

where the index k denotes the current node and nb denotes the neighbouring nodes that have already been in-painted such that $|\vec{x}_{nb} - \vec{x}_k| \le \varepsilon$, where ε dictates the size of the neighbourhood used in this scheme.

If the order and weighting function are chosen appropriately, one can solve the PDE. We solved each value in the domain in the order of increasing distance from the boundary. We chose to use the weighting function described in Bornemann et $al.$, 2007 [24] given by:

$$w(\vec{x}_1, \vec{x}_2) = \sqrt{\frac{\pi}{2}} \frac{\mu}{|\vec{x}_1 - \vec{x}_2|} \exp\left(-\frac{\mu^2}{2\varepsilon^2} \left(\vec{c}^{\perp}(\vec{x}_1) \cdot (\vec{x}_1 - \vec{x}_2) \right)^2 \right), \tag{5.6}$$

where μ is a user specified parameter.

Due to the nature of this fast-marching scheme, instead of solving Equation 5.3, the following PDE is solved:

$$\vec{v} \cdot \nabla I_0^c = 0 \qquad \in \Omega \tag{5.7a}$$

$$I_0^c = I \qquad \in \partial\Omega \tag{5.7b}$$

$$\vec{v} = \begin{cases} \vec{c} & \hat{n} \cdot \vec{c} > 0 \\ -\vec{c} & \hat{n} \cdot \vec{c} < 0 \\ \hat{n} & \hat{n} \cdot \vec{c} = 0 \, , \end{cases} \tag{5.7c}$$

where $\hat{n}$ is the normal to the boundary, $\partial\Omega$, and $\vec{c}$ is the desired convection field (i.e. the coherence direction).

If the direction field is parallel to the domain boundary (i.e. $\hat{n} \cdot \vec{c} = 0$), the fast-marching scheme will convect the image information perpendicular to the boundary instead of along the convection field. For this reason, we exclude parts of the boundary that are parallel to the convection field in the determination of the distance ordering, as in Marz *et al.* 2011 [26]. Specifically, we require that:

$$(\hat{n} \cdot \vec{c})^2 < \gamma. \tag{5.8}$$

For convection inpainting there are five user-specified parameters: ε, σ, ρ, μ and γ. For this study, unless stated otherwise, we used $\varepsilon = 15$, $\sigma = 2.5$, $\rho = 10$, $\mu = 20$ and $\gamma = 0.2$. These parameters were based on the recommendations in the studies by März [24, 26], modified to ensure the vector field was parallel to the muscle fibres. The parameters were determined on different fields of view than the one used for the analyses below. All image intensities were normalized such that $0 \leq I \leq 1$.

5.2.3   Oxygen Saturation Calculation

We calculated SO_2 from:

$$SO_2 = \frac{b_1 - b_2 R}{a_2 R - a_1} \tag{5.9a}$$

$$R = \frac{OD(\lambda_1)}{OD(\lambda_2)} \tag{5.9b}$$

$$a_i = \epsilon_{Hb_{O_2}}(\lambda_i) - \epsilon_{Hb}(\lambda_i) \tag{5.9c}$$

$$b_i = \epsilon_{Hb}(\lambda_i), \tag{5.9d}$$

where $\epsilon_{Hb_{O_2}}$ and ϵ_{Hb} are the extinction coefficients of oxy- and deoxy- hemoglobin at wavelength λ_i, respectively.

5.2.4   Image Acquisition

The images used in this study were captured using two QImaging Rolera XR digital cameras attached to the side port of an Olympus XI-81 inverted microscope using a 50/50 beam-splitter to two narrow bandpass filters centred at 442 nm and 454 nm. The images were taken from an *in vivo* preparation of rat *extensor digitorum longus* (EDL) muscle. For more information on the *in vivo* preparation, see Fraser *et al.* 2012 [15].

5.3   Results

Image inpainting was applied to intravital video microscopy images to recover the incident intensity behind the RBCs. The inpainting domain was constructed by masking out RBCs using a thresholding technique to locate the RBCs similar to Japee *et al.* [12, 19]. Figure 5.2 shows the results of inpainting a 40x image. This image was chosen since it is highly

textured and therefore demonstrates the ability of inpainting to recover local features within an image. From Figure 5.2, diffusion-based inpainting tends to blur features in the image, whereas the convection-based approach tends to recover the structures in the image.
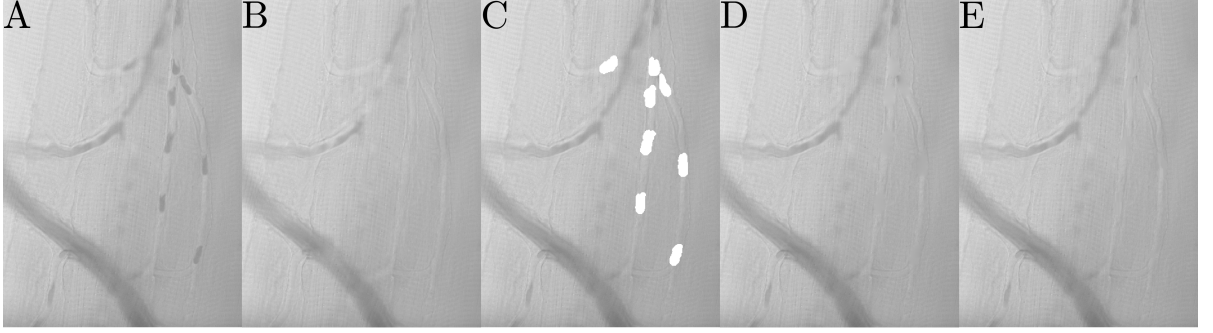
Figure 5.2: *(A) A single frame from a 40x in vivo capture of rat EDL. (B) Maximum intensity image calculated over 5 frames ($\Delta t = 0.24$ s). (C) Masked regions (in white) indicating the inpainting domain. (D) Diffusion-based inpainting image. (E) Convection-based inpainting image ($\varepsilon = 6$, $\sigma = 0.5$, $\rho = 8$, $\mu = 100$ and $\gamma = 0.2$).*

Ultimately, I_{max} is sensitive to the number of frames used to calculate the maximum, which we express as Δt (the number of frames divided by the frame rate). To demonstrate how I_{max} depends on Δt, we track the pixel intensities of a single pixel within a capillary in a 20x image, as shown in Figure 5.3—this demonstrates that when the time step is too small, as when $\Delta t = 0.2$ s, I_{max} sometimes fails to capture the background intensity. However, as Δt is increased, I_{max} also increases, leading to an over-approximation of the background intensity. To demonstrate the sensitivity of I_{max} to the fluctuations in the image, we also track a pixel in a tissue region, as shown in the bottom panel of Figure 5.3.

To compare the effectiveness of inpainting, we calculated the difference between I_{max} and the inpainted image on a pixel-by-pixel basis in an example 20x image. However, since I_{max} is not the true solution, this does not accurately measure the error in inpainting. To estimate the true error in I_0, we inpaint plasma regions that do not have RBCs, and compare the inpainting solution to the original image. This method is also used to estimate the error in I_{max}.
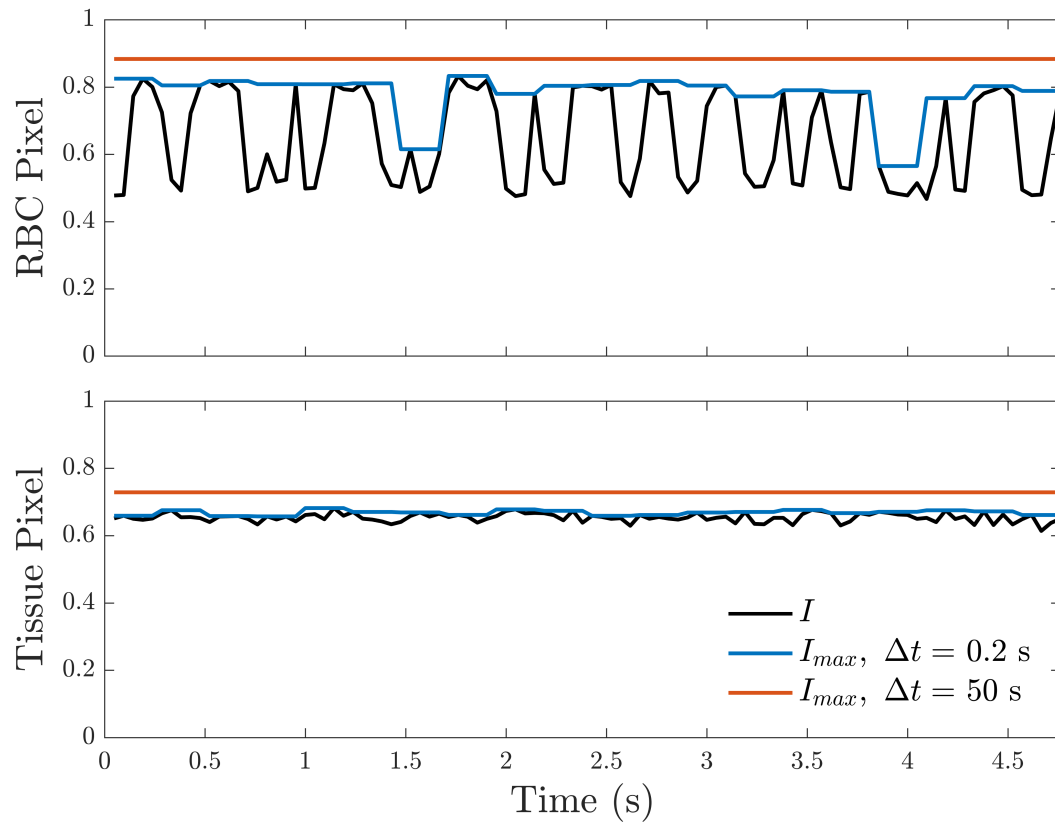
Figure 5.3: *Pixel intensity (black) of a representative pixel in a capillary (top) and the tissue (bottom) for a 20x in vivo capture of a rat EDL. I_{max} calculated with 5 ($\Delta t = 0.24$ s) and 1050 ($\Delta t = 50$ s) frames is shown in blue and red, respectively.*

Figure 5.4 shows the image used to assess the error in I_0 (panel A), as well as the masked RBCs (panel B) and the masked plasma regions (panel C). The RBC masked region consists of 3675 pixels, and the plasma masked region consists of 2900 pixels.
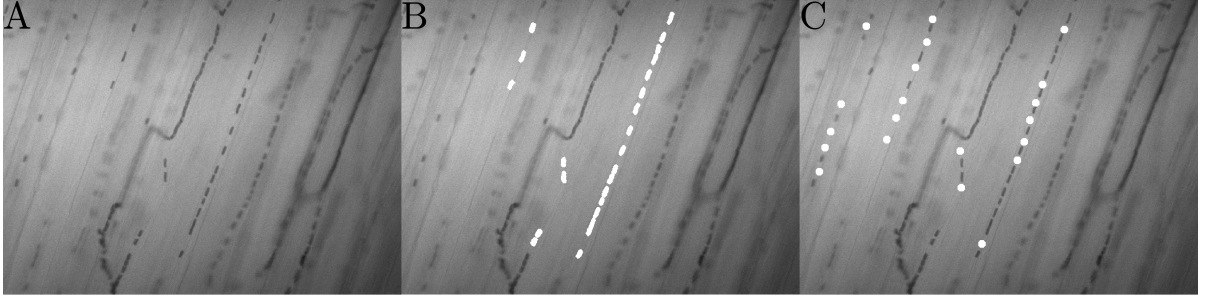
Figure 5.4: *(A) An example 20x in-vivo microscopy image. (B) Masked RBC regions (in white) indicating the inpainting domain used to calculate I_0 behind the RBCs. (C) Masked plasma regions (in white) indicating the inpainting domain used to determine the error of our I_0 calculations.*

The error in the different I_0 estimations is shown in Figure 5.5. This is plotted over a wide range of Δt values, since I_{max} is sensitive to this parameter. The top panel compares the inpainted I_0 values to I_{max}, calculated as the absolute value of the difference between the inpainted region and I_{max} and then averaged over all pixels. The difference is higher for very low Δt since I_{max} does not remove the RBC. Then, as discussed, after the optimum Δt, I_{max} does increasingly worse as Δt increases.

Thus far, we have compared the inpainting solution to the I_{max} solution; however, we are primarily interested in how all three I_0 estimates compare to the true I_0. To estimate the true error in the inpainting solution, we estimate I_0 within the plasma regions since these regions do not contain RBCs, and are thus equal to I_0. Using the masked plasma region shown in Figure 5.4C, the error is calculated as the mean of the absolute value of the difference between the masked regions of an image, and the three estimates of I_0 (I_{max}, I_0^d and I_0^c), as shown in bottom panel of Figure 5.5. This figure clearly shows the increasing error in

I_{max} with Δt. It also shows that the inpainting methods perform quite well, outperforming I_{max} even at small Δt values. It also appears that convection-based inpainting outperforms diffusion-based inpainting, as expected, though the difference is surprisingly small.
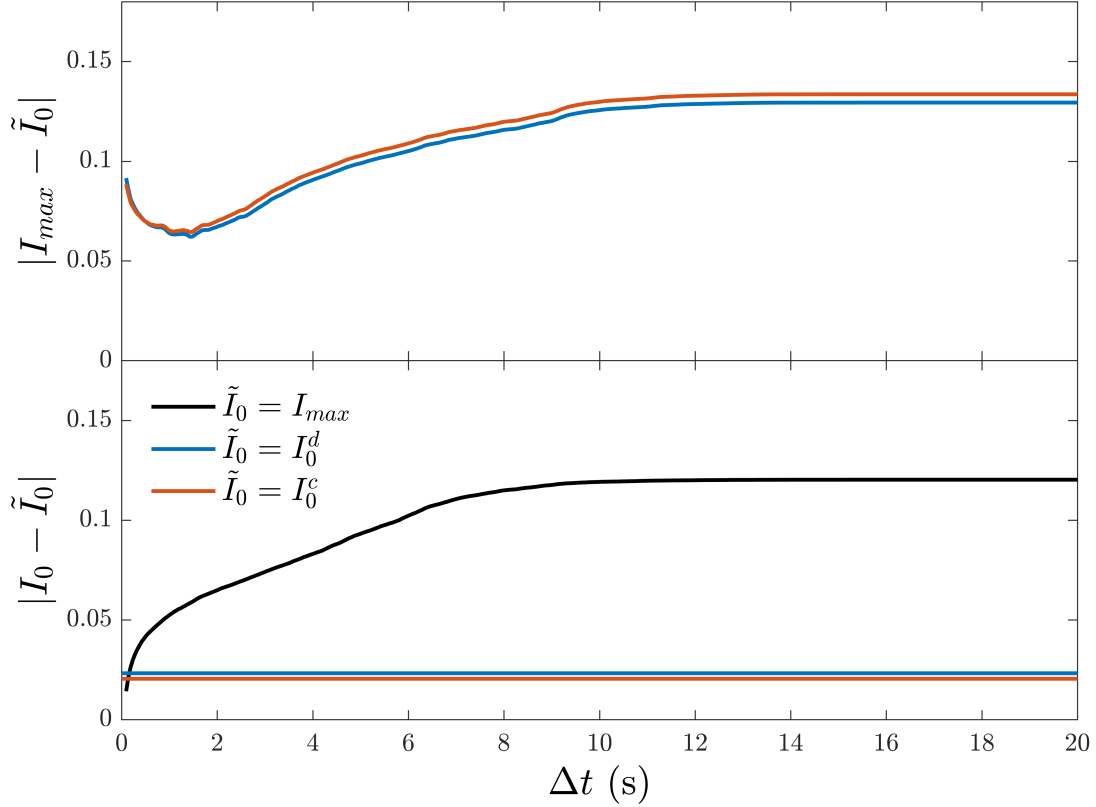
Figure 5.5: *Error estimation for an example image. (Top) Comparison of I_0 calculated using inpainting to the maximum intensity-based, I_{max}, calculation. Error is calculated as the mean of the absolute value of the difference between the inpainted image and the I_{max} image, averaged across all pixels in the masked region. (Bottom) Comparison of I_0 estimates to true I_0. The images used were captured at 21 frames/s.*

Histograms of the different pixel errors calculated above are shown in Figure 5.6. Since I_{max} is always larger than the true I_0, the errors are always negative as shown in the left panel. For $\Delta t = 2$s and 50s, the average absolute errors are -0.06 ± 0.03 and -0.13 ± 0.04, respectively. For the inpainting methods, both diffusion and convection inpainting have average absolute errors 0.00 ± 0.03.
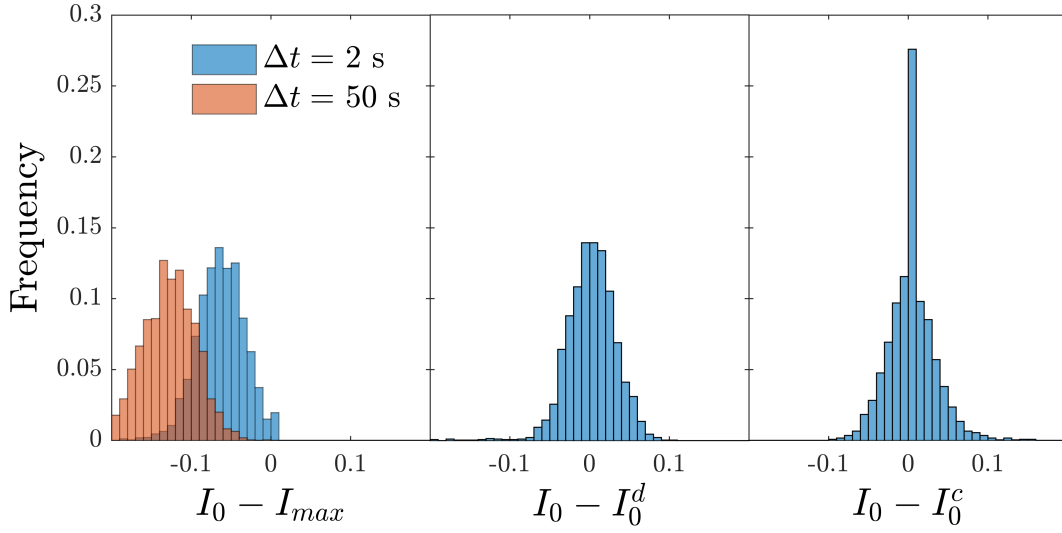
Figure 5.6: *Distribution of errors for the example image shown in Fig 5.4. The distribution of errors measured as $I_0 - \tilde{I}_0$, where $\tilde{I}_0 = I_{max}$, I_0^d and I_0^c. I_{max} (left) is calculated with 5 ($\Delta t = 0.24$ s) and 1050 ($\Delta t = 50$ s) frames. Errors are always negative, since I_{max} over-approximates the background light intensity. Diffusion (middle) and convection (right) based inpainting methods have similar errors, and a standard deviation of 0.03.*

To relate these errors in I_0 to the errors in SO_2 measurements, we first express the true incident intensity, I_0, for both wavelengths in terms of the estimated incident intensity, $\tilde{I}_0$, as:

$$I_0^i = \tilde{I}_0^i + \xi_i, \tag{5.10}$$

where the index, i, indicates the wavelength, λ_i, and ξ_i is the estimation error.

We can then write the error in saturation as:

$$E_s = SO_2 - \tilde{SO}_2, \tag{5.11}$$

where SO_2 is the true saturation and $\tilde{SO_2}$ is the estimated saturation. The estimated saturation can be expressed as a function of the I_0 errors, ξ_1 and ξ_2 and the true saturation, SO_2 using Equation 5.9 with the estimated optical density ratio, $\tilde{R}$,

$$\tilde{R} = \frac{OD(\lambda_1) + \log_{10}\left(1 - \frac{\xi_1}{I_0^1}\right)}{OD(\lambda_2) + \log_{10}\left(1 - \frac{\xi_2}{I_0^2}\right)}, \tag{5.12}$$

where $OD(\lambda_i)$ is the true optical density at wavelength, λ_i, which can be expressed by:

$$OD(\lambda_i) = \left(\epsilon_{Hb}(\lambda_i)(1 - SO_2) + \epsilon_{HbO_2}(\lambda_i)SO_2\right)cx, \tag{5.13}$$

where c is RBC hemoglobin saturation, x is path length and ϵ_{HbO_2} and ϵ_{Hb} are the extinction coefficients of oxy/deoxy-hemoglobin, respectively.

Since the errors in I_0 only show up as relative error, and assuming a typical RBC hemoglobin concentration of 20 mM and a path length of 8 µm, the error in saturation is only a function of true saturation, SO_2, and the relative errors $\hat{\xi}_1$ and $\hat{\xi}_2$, where $\hat{\xi}_i = \frac{\xi_i}{I_0^i}$. Figure 5.7 shows a contour plot of the absolute error in SO_2 as a function of relative errors in incident intensities at both wavelengths. Since the error in saturation is also dependent on true SO_2, we show the worst case error at $SO_2 = 0$, the best case at $SO_2 = 1$ and a typical case ($SO_2 = 0.65$).

Finally, we calculated SO_2 for individual RBCs using all three methods, as shown in Figure 5.8. SO_2 was calculated as outlined in Section 5.2.3 using the median optical densities of each cell. The coefficients a_1, a_2, b_1 and b_2 were calculated according to Equation 5.9 c-d using the hemoglobin extinction coefficients ($\lambda_1 = 442$ nm, $\lambda_2 = 454$ nm) tabulated by
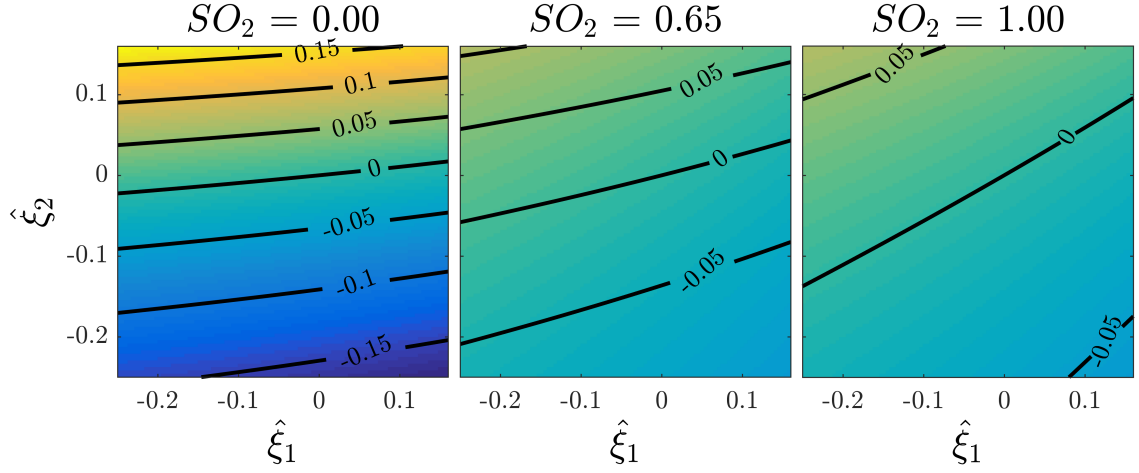
Figure 5.7: *Contour plot of the absolute errors in SO_2 as a function of the relative errors in I_0, for three different SO_2 values.*

Scott Prahl [27].

5.4   Discussion

In this paper, we have applied digital inpainting to estimate the background intensity image, I_0, in order to calculate SO_2. We evaluated the accuracy of our I_0 estimates by performing the calculation on regions where I_0 was already known. Overall, inpainting was more accurate at estimating I_0 than the previous I_{max} method in most cases, with convection slightly outperforming diffusion. Though convection-based inpainting outperformed its diffusion-based counterpart, diffusion-based inpainting is much more straightforward to implement and is less computationally demanding. The I_{max} method, however, performs better than inpainting when the Δt parameter is sufficiently small since the background intensity is less likely to vary over short periods of time and there is less chance for outlier noise to appear.

In practice, Δt values used to measure SO_2 typically range from 3 s to 60 s, with a mode of 4 s. In this range of Δt, inpainting is more accurate than the maximum intensity image for estimating I_0. Further, there are many cases where I_{max} fails: capillaries with very slow or
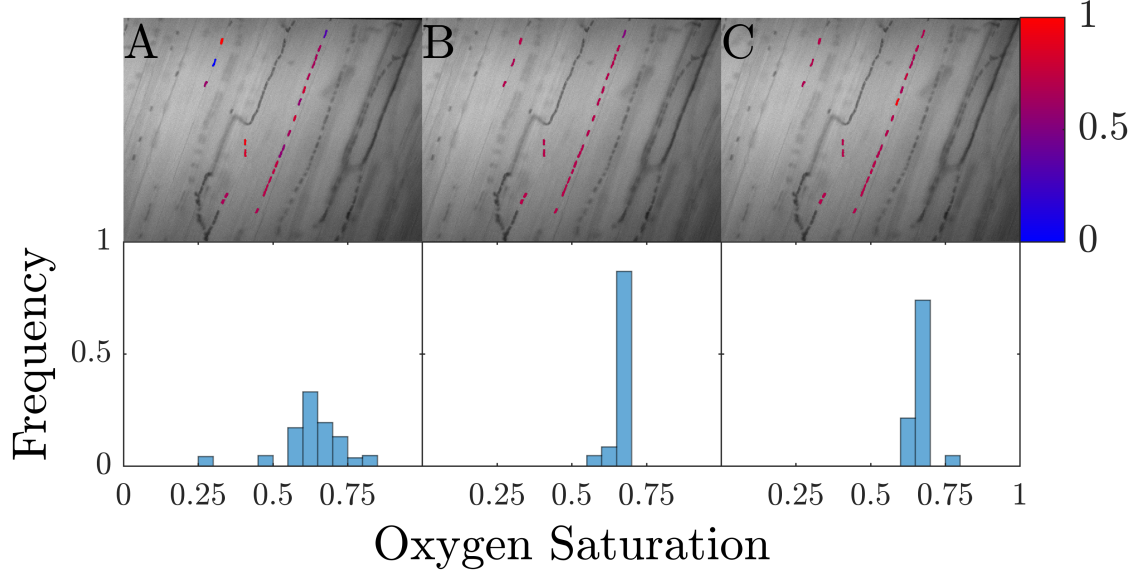
Figure 5.8: *Calculated SO_2 values for selected in-focus cells, using (A) $\tilde{I}_0 = I_{max}$ ($\Delta t \approx 4$ s), (B) $\tilde{I}_0 = I_0^d$ and (C) $\tilde{I}_0 = I_0^c$. The top half of the figure shows the SO_2 overlaid on top of the original image. The bottom half shows the distribution of the SO_2 values.*

stopped flow and vessels with high hematocrit are not able to be analyzed. Additionally, in some instances, long exposure times are required to collect enough light to visualize the tissue; this results in an attenuated approximation of I_0 using the maximum intensity based estimation. In all of these cases, digital inpainting can be used to estimate I_0 since it is not dependent on temporal data. However, though inpainting methods can correctly recover I_0 for long exposure times, the resulting SO_2 would not be correct if the RBC of interest is blurred due to motion since the estimated intensity of the RBC would be larger than the true intensity.

Based on the errors in our I_0 estimation, we can predict what the errors in SO_2 will be. Figure 5.7 shows that SO_2 error is more sensitive to positive errors than negative errors. Thus since our I_{max} estimation always over-approximates I_0, errors in SO_2 are less sensitive to errors in I_{max}. The errors in I_0 for the inpainting methods are symmetric about zero, though they have a very low standard deviation, thus the resulting errors in saturation are low. It is interesting to note that the errors are saturation dependent, with SO_2 errors being more sensitive to errors in I_0 at low SO_2. However, SO_2 values close to zero are

rarely seen *in-vivo*. Although not explicitly shown, the errors in SO_2 are also dependent on the wavelengths chosen. If we chose one wavelength (λ_2) to be isosbestic, then the error in SO_2 is inversely proportional to the difference in the extinction coefficient of oxy- and deoxy-hemoglobin. Therefore, choosing a wavelength such that there is a large difference in extinction coefficients would result in an SO_2 error that is less sensitive to errors in I_0 estimation. It is important to note that we presented the results for only one representative image as a demonstration of the use on inpainting to estimate incident light. Inclusion of more images would be necessary to generalize our inferences.

Additionally, we calculated SO_2 values on a cell-by-cell basis using each of the three methods. All three I_0 estimations give comparable SO_2 values, though there is a larger range of SO_2 values from the I_{max} approach. In practice, rather than using extinction coefficients to calculate the SO_2 coefficients, we can calculate the coefficients using data from RBCs with known SO_2 values. This improves the performance of the I_{max}-based approach since the calibration values account for the over-approximation in I_{max}. This is not required for inpainting since the inpainting approach does not systematically overestimate I_0.

One factor to consider in inpainting is that it requires a defined inpainting region. The size and shape of the RBC mask may influence the inpainting solution since PDEs are highly sensitive to geometry. For diffusion-based inpainting, the solution is an average of the boundary propagated inward equally from every direction. This property makes the diffusion-based approach sensitive to the location of the boundaries. For example, in some images the capillaries have a brighter intensity than the surrounding tissue. In this example, an inpainting boundary that is fully contained within the capillary will outperform an inpainting boundary that extends into the sounding tissue. The convection-based approach is less sensitive to this phenomenon since pixel information convects along the coherence directions. In our images, the coherence directions run parallel to the muscle fibres, preventing the transport of information from the tissue into the capillary.

Though the convection inpainting scheme used in this manuscript is not overly sensitive to the masked region, the method does involve a number of free parameters (ε, σ, ρ, μ and γ). These may affect the accuracy of our I_0 estimation. The ε parameter dictates how many points the scheme uses to calculate the value at each point in the domain, which influences how well the scheme can accurately represent the direction of the convection. For example, a convection direction that is perpendicular to the boundary requires only one point, where as small angles to the boundary require more. The σ and ρ parameters dictate the calculation of the coherence direction; σ determines how sensitive the coherence directions are to changes in intensity and ρ determines the sensitivity to variations in the gradient. Images with a large amount of noise should choose large σ values. For our application, we chose large ρ values to ensure that the coherence direction only follows the larger features. The μ parameter dictates how much diffusion is allowed; as $\mu \to \infty$, the artificial diffusion goes to zero. Artificial diffusion ensures that the solution is continuous when the coherence direction is not well-defined (i.e. in the center of the domain). The γ parameter dictates which portions of the boundary are allowed to convect information into the boundary. For our application, we know that the large features are muscle fibres that run parallel along capillaries, thus we chose a large γ to ensure that the convection only comes along muscle fibres. In this work, the parameters were not chosen to minimize the error in I_0, though an optimization could potentially be done to yield better results.

In this study, we only considered two possible inpainting algorithms, though there are numerous other possible schemes in the literature. Another common PDE-based example is anisotropic diffusion-based inpainting, which uses a diffusion coefficient that is inversely proportional to the image gradient [22]. This type of scheme yields similar results to a convection based approach, which can be seen by expanding the anisotropic diffusion equation (see Equation 5.14). There also exists texture-based inpainting approaches which attempt to preserve the texture of an image throughout the inpainting domain; an example of

texture-based inpainting is described in [28]. Additionally, there have been advances in machine learning algorithms to determine inpainting domains. For instance, blind inpainting determines which regions to inpaint based on their different texture from the background [29]. Such an algorithm could allow for automatic detection of all RBC regions in the tissue.

$$\nabla \cdot \left(D(I_0^{ad})\nabla I_0^{ad} \right) = 0 \tag{5.14a}$$

$$\nabla D(I_0^{ad}) \cdot \nabla I_0^{ad} + D(I_0^{ad})\nabla^2 I_0^{ad} = 0 \tag{5.14b}$$

$$\vec{c} \cdot \nabla I_0^{ad} + D(I_0^{ad})\nabla^2 I_0^{ad} = 0 \tag{5.14c}$$

$$\vec{c} = \nabla D(I_0^{ad}) \tag{5.14d}$$

Inpainting techniques have also been applied to many different biological applications. For example, they can be used to create 3D a reconstruction of MRI images from 2D slices [30], to pre-process MRI images to help with registration [31, 32], in vascular reconstruction [33] and to help analyze cDNA microarrays [34].

Despite the many benefits of using digital inpainting to recover I_0, there are some drawbacks. First, inpainting is more computationally demanding than the I_{max} method with convection being more demanding than diffusion. Second, inpainting requires a separate algorithm for determining the locations of the RBCs, making it more difficult to automate. If computational resources are an issue, one could implement a hybrid approach that uses digital inpainting when the I_{max} methods fails or when a higher resolution of I_0 is required.

Overall, digital inpainting is a method for restoring images that is beginning to be applied to biological applications. In this study, we have tested whether digital inpainting can be used to improve dual-wavelength SO_2 measurements, by providing a better estimate of background light intensity. We have found that inpainting is a viable method for calculat-

ing I_0, and that it is often more accurate than the common I_{max} method. In addition to outperforming I_{max} in most cases, it succeeds in cases where the traditional I_{max} algorithm fails, such as for stopped or slow moving cells, capillaries with high hematocrit or rapidly changing background intensities. Additionally, since inpainting allows I_0 to be calculated for each individual frame, inpainting allows for a higher temporal resolution of the background intensity than I_{max}. Taken together these improvements in I_0 estimation represent a major advance for spectrophotometric measurement of red blood cell SO_2 in intravital video applications.

References

[1] C. G. Ellis, D. Goldman, M. Hanson, A. H. Stephenson, S. Milkovich, A. Benlamri, M. L. Ellsworth, and R. S. Sprague, "Defects in oxygen supply to skeletal muscle of prediabetic ZDF rats," *American Journal of Physiology-Heart and Circulatory Physiology*, vol. 298, no. 6, pp. H1661–H1670, 2010.

[2] D. Goldman, R. M. Bateman, and C. G. Ellis, "Effect of sepsis on skeletal muscle oxygen consumption and tissue oxygenation: interpreting capillary oxygen transport data using a mathematical model," *American Journal of Physiology-Heart and Circulatory Physiology*, vol. 287, no. 6, pp. H2535–H2544, 2004.

[3] D. Goldman, R. M. Bateman, and C. G. Ellis, "Effect of decreased O_2 supply on skeletal muscle oxygenation and O_2 consumption during sepsis: role of heterogeneous capillary spacing and blood flow," *American Journal of Physiology-Heart and Circulatory Physiology*, vol. 290, no. 6, pp. H2277–H2285, 2006.

[4] R. M. Bateman, M. D. Sharpe, J. E. Jagger, and C. G. Ellis, "Sepsis impairs microvascular autoregulation and delays capillary response within hypoxic capillaries," *Critical Care*, vol. 19, no. 1, p. 389, 2015.

[5] M. L. Ellsworth, R. N. Pittman, and C. G. Ellis, "Measurement of hemoglobin oxygen saturation in capillaries," *American Journal of Physiology-Heart and Circulatory Physiology*, vol. 252, no. 5, pp. H1031–H1040, 1987.

[6] K. Matthes, "Über den einfluß der atmung auf die sauerstoffsättigung des arterienblutes," *Naunyn-Schmiedeberg's Archives of Pharmacology*, vol. 176, no. 6, pp. 683–696, 1934.

[7] G. A. Millikan, "The oximeter, an instrument for measuring continuously the oxygen saturation of arterial blood in man," *Review of scientific Instruments*, vol. 13, no. 10, pp. 434–444, 1942.

[8] B. Chance, "Spectrophotometry of intracellular respiratory pigments," *Science*, vol. 120, no. 3124, pp. 767–775, 1954.

[9] N. M. Anderson and P. Sekelj, "Studies on the light transmission of nonhemolyzed whole blood. determination of oxygen saturation," *The Journal of laboratory and clinical medicine*, vol. 65, no. 1, pp. 153–166, 1965.

[10] R. N. Pittman and B. R. Duling, "A new method for the measurement of percent oxyhemoglobin," *Journal of applied physiology*, vol. 38, no. 2, pp. 315–320, 1975.

[11] C. G. Ellis, M. L. Ellsworth, and R. Pittman, "Determination of red blood cell oxygenation in vivo by dual video densitometric image analysis," *American Journal of Physiology-Heart and Circulatory Physiology*, vol. 258, no. 4, pp. H1216–H1223, 1990.

[12] S. A. Japee, R. N. Pittman, and C. G. Ellis, "Automated method for tracking individual red blood cells within capillaries to compute velocity and oxygen saturation," *Microcirculation*, vol. 12, no. 6, pp. 507–515, 2005.

[13] C. G. Ellis, M. L. Ellsworth, R. N. Pittman, and W. L. Burgess, "Application of image analysis for evaluation of red blood cell dynamics in capillaries," *Microvascular research*, vol. 44, no. 2, pp. 214–225, 1992.

[14] N. W. Ghonaim, L. W. Lau, D. Goldman, C. G. Ellis, and J. Yang, "A micro-delivery approach for studying microvascular responses to localized oxygen delivery," *Microcirculation*, vol. 18, no. 8, pp. 646–654, 2011.

[15] G. M. Fraser, S. Milkovich, D. Goldman, and C. G. Ellis, "Mapping 3-D functional capillary geometry in rat skeletal muscle in vivo," *American Journal of Physiology-Heart and Circulatory Physiology*, vol. 302, no. 3, pp. H654–H664, 2012.

[16] G. M. Fraser, D. Goldman, and C. G. Ellis, "Comparison of generated parallel capillary arrays to three-dimensional reconstructed capillary networks in modeling oxygen transport in discrete microvascular volumes," *Microcirculation*, vol. 20, no. 8, pp. 748–763, 2013.

[17] N. W. Ghonaim, G. M. Fraser, C. G. Ellis, J. Yang, and D. Goldman, "Modeling steady state SO_2-dependent changes in capillary atp concentration using novel O_2 micro-delivery methods," *Frontiers in physiology*, vol. 4, 2013.

[18] S. A. Japee, C. G. Ellis, and R. N. Pittman, "Flow visualization tools for image analysis of capillary networks," *Microcirculation*, vol. 11, no. 1, pp. 39–54, 2004.

[19] S. A. Japee, R. N. Pittman, and C. G. Ellis, "A new video image analysis system to study red blood cell dynamics and oxygenation in capillary networks," *Microcirculation*, vol. 12, no. 6, pp. 489–506, 2005.

[20] M. Bertalmio, G. Sapiro, V. Caselles, and C. Ballester, "Image inpainting," in *Proceedings of the 27th annual conference on Computer graphics and interactive techniques*, pp. 417–424, ACM Press/Addison-Wesley Publishing Co., 2000.

[21] M. Bertalmio, A. L. Bertozzi, and G. Sapiro, "Navier-stokes, fluid dynamics, and image and video inpainting," in *Computer Vision and Pattern Recognition, 2001. CVPR 2001. Proceedings of the 2001 IEEE Computer Society Conference on*, vol. 1, pp. I–I, IEEE, 2001.

[22] T. F. Chan and J. Shen, "Nontexture inpainting by curvature-driven diffusions," *Journal of Visual Communication and Image Representation*, vol. 12, no. 4, pp. 436–449, 2001.

[23] D. Auroux and M. Masmoudi, "A one-shot inpainting algorithm based on the topological asymptotic analysis," *Computational & Applied Mathematics*, vol. 25, no. 2-3, pp. 251–267, 2006.

[24] F. Bornemann and T. März, "Fast image inpainting based on coherence transport," *Journal of Mathematical Imaging and Vision*, vol. 28, no. 3, pp. 259–278, 2007.

[25] A. Telea, "An image inpainting technique based on the fast marching method," *Journal of graphics tools*, vol. 9, no. 1, pp. 23–34, 2004.

[26] T. März, "Image inpainting based on coherence transport with adapted distance functions," *SIAM Journal on Imaging Sciences*, vol. 4, no. 4, pp. 981–1000, 2011.

[27] S. Prahl, "Optical absorption of hemoglobin," tech. rep., Oregon Medical Laser Center, 1999.

[28] J. F. Cai, R. H. Chan, and Z. Shen, "Simultaneous cartoon and texture inpainting," *Inverse Probl. Imaging*, vol. 4, no. 3, pp. 379–395, 2010.

[29] N. Cai, Z. Su, Z. Lin, H. Wang, Z. Yang, and B. W. K. Ling, "Blind inpainting using the fully convolutional neural network," *The Visual Computer*, vol. 33, no. 2, pp. 249–261, 2017.

[30] A. Souza and R. Senn, "Model-based super-resolution for MRI," in *Engineering in Medicine and Biology Society, 2008. EMBS 2008. 30th Annual International Conference of the IEEE*, pp. 430–434, IEEE, 2008.

[31] M. Sdika and D. Pelletier, "Nonrigid registration of multiple sclerosis brain images using lesion inpainting for morphometry or lesion mapping," *Human brain mapping*, vol. 30, no. 4, pp. 1060–1067, 2009.

[32] N. Guizard, K. Nakamura, P. Coupé, V. S. Fonov, D. L. Arnold, and D. L. Collins, "Non-local means inpainting of ms lesions in longitudinal image processing," *Frontiers in neuroscience*, vol. 9, 2015.

[33] P. Teikari, M. Santos, C. Poon, and K. Hynynen, "Deep learning convolutional networks for multiphoton microscopy vasculature segmentation," *arXiv preprint arXiv:1606.02382*, 2016.

[34] P. O'Neill, G. D. Magoulas, and X. Liu, "Quality processing of microarray image data through image inpainting and texture synthesis," in *Biomedical Imaging: Nano to Macro, 2004. IEEE International Symposium on*, pp. 117–120, IEEE, 2004.

Chapter 6

Microfluidic Device for the Rapid Oxygen Desaturation of Hemoglobin in Red Blood Cells: A Tool for Studying Oxygen-Dependent ATP Release

6.1   Introduction

Red blood cells (RBCs) play an important role as the carrier of oxygen (O_2) in the circulatory system. They are also thought to be involved in the local regulation of O_2 supply through the O_2-dependent release of ATP [1–4]. By this mechanism, ATP is released through pannexin-1 channels in the RBC membrane in response to low hemoglobin oxygen saturation (SO_2). The intraluminal ATP then binds to endothelial P2Y2 receptors causing a conducted vasodilatory response to increase local blood flow [2, 5–9]. In addition to O_2 desaturation [1, 10], RBCs release ATP in response to numerous other stimuli, including shear-stress [11], pH [1] and osmotic pressure [12]. Although the mechanisms for the release of ATP from RBCs have been extensively studied [11, 13–15], the role of ATP release as a mechanism for O_2 regulation remains unclear.

One important consideration in the regulation of O_2 is the time required for ATP to be released from the RBCs following desaturation. Since the RBCs are in motion, the location of ATP release is dictated by RBC velocity and ATP release time. Thus, the dynamics dictate the spatial acuity of this regulatory mechanism. Understanding the dynamics of this process could not only have implications in the understanding of oxygen regulation, but may also play a role in the investigation of disease since O_2-dependent ATP release has been shown to be impaired in diseases such as type II diabetes [14, 16] and sepsis [17].

The objective of this study is to develop an experimental system to control the spatial oxygenation of isolated RBCs *in vitro* to facilitate the measurement of the dynamics of O_2-dependent ATP release. To measure the dynamics, a similar approach to Wan *et al.* [18] can be used, where they measured the dynamics of shear-dependent ATP release from RBCs using a microfluidic device. In their setup, they used a microfluidic device with a constriction to cause a spatial increase in shear stress to stimulate the release of ATP. ATP was measured using a firefly luciferase assay and the position of the signal relative to the change in shear was related to ATP release time. In the place of the constriction, we will stimulate the release of ATP by using an O_2-permeable window interfaced with a gas exchange device to cause a rapid change in SO_2.

This system was first proposed in Sové *et al.* [19], where we extensively modelled the experimental design to see if such a setup would be sensitive enough to detect ATP release time from RBCs. The computational model consisted of an idealized microfluidic device whose walls were impermeable to O_2, but which contained an O_2-permeable window to cause the rapid change in O_2. The computational model not only simulated the transport of O_2 in the microfluidic device, but also the release of ATP and subsequent detection. This confirmed that the experimental design was theoretically feasible and that we could measure ATP release time. Additionally, it demonstrated that the relationship between the ATP concentration and the luminescence from the firefly luciferase was not straightforward.

While the idealized design was deemed sufficient for our study, fabrication techniques for oxygen-impermeable materials such as glass are often expensive and require specialized equipment. Therefore, we revised our design to be cost-effective and easier to manufacture. Due to the simplicity and cost effectiveness of PDMS-based microfabrication techniques, we chose to use PDMS (polydimethyl siloxane), a highly O_2-permeable material, for the primary substrate of the device. In order to cause the localized change in O_2, we needed to interface the device with an O_2 impermeable material with a window to allow for gas exchange. Since this design differed significantly from the original idealized design, we used a 3D computational model of O_2 transport to confirm that we could still cause a rapid change in O_2 [20]. This model also allowed us to optimize the device geometry to maximum the change in O_2.

The current study presents the fabrication of an experimental system that can cause a rapid change in RBC SO_2 for the measurement of the dynamics of O_2-dependent ATP release from RBCs. We quantify the changes in SO_2 using a dual-wavelength microscopy system to demonstrate the ability of the device to cause rapid and local desaturation. Finally, we quantify the sensitivity of our system by determining the minimum ATP concentration we can measure.

6.2   Methods

6.2.1   Gas Exchange Chamber

The gas exchange chamber design was based on previous work [21]. It was comprised of a microscope stage insert, a gasket to form the side walls of the gas channel and a platform for the inlet and outlet of the channel (see Figure 6.1); these components were designed in FreeCAD and 3D printed. The bottom of the channel was closed by a replaceable glass

slide and the top of the channel was closed by a custom, laser-cut glass slide with a square window (1x1 mm) for gas exchange using a process described in [22]. The components were assembled together using vacuum grease to ensure no gas leakage.
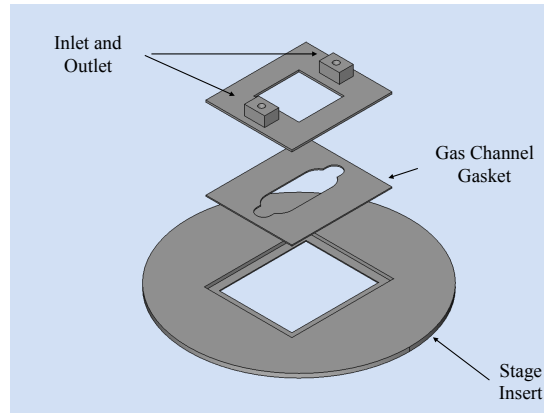
Figure 6.1: *Three dimensional CAD model of gas chamber components. The inlet/outlet mount, gas channel gasket and stage insert were 3D printed. The gas channel is sealed on the bottom with a glass slide and on the top with a laser-cut glass slide.*

A PDMS microfluidic device (fabrication described in Section 6.2.2) was aligned with the gas exchange window such that the RBC flow is perpendicular to the gas flow. A schematic of the microfluidic device-gas channel interface is shown in Figure 6.2.
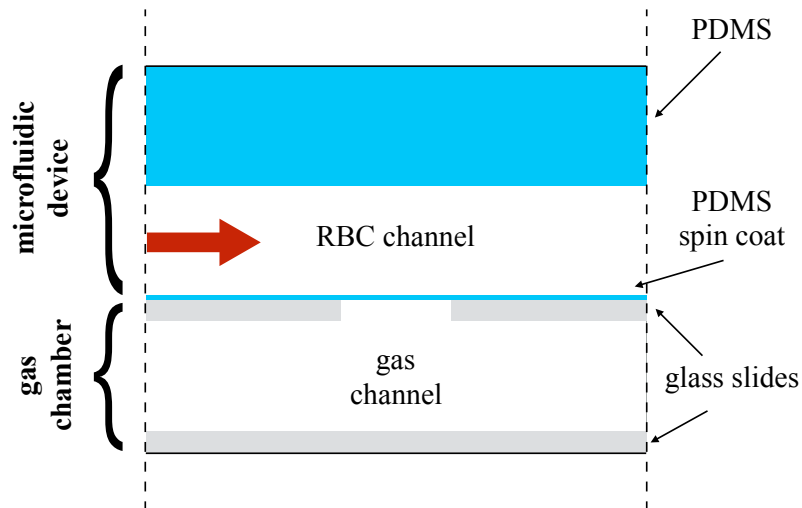
Figure 6.2: *Schematic of the microfluidic device with gas chamber interface. Red arrow indicates the direction of RBC flow. The gas channel flow is orthogonal to the RBC flow.*

6.2.2 Microfluidic Device

Fabrication: Microfluidic devices were fabricated with poly-dimethyl siloxane (PDMS; Dow Corning Corporation Sylgard® 184) using impression molding similar to techniques described in [23–25]; the master was machined from acrylic by micro-milling using a standard three-axis CNC mill (TrakK3SX-3 with ProTrakSMX control module; Southwestern Industries Inc.). It was designed with removable walls to facilitate the removal of PDMS from the master (Figure 6.3). PDMS was mixed in a 10:1 ratio of prepolymer base to cross-linking agent. Liquid PDMS was poured into the master and cured at 60 °C for 90 minutes. After curing, it was removed from the mold and trimmed to the final shape. The bottom of the channel was fabricated by spin-coating PDMS at 2000 rpm for 60 seconds onto a glass slide following methods by [23–25] (Figure 6.3). The two components were joined using the partial curing method described in [25]. In this method, the spin-coated layer was partially cured at 50 °C for 29 minutes and the bond was formed by bringing the two components into conformal contact with no external pressure; the assembled device was cured at 60 °C for 90 minutes. Cured devices were carefully peeled away from the glass slide taking care not to break the thin PDMS bottom. Once fully cured, the microfluidic devices were placed firmly on the glass exchange surface to form a temporary bond held together by Van der Waals forces.

Design considerations: To optimize the rapid desaturation of the RBCs in the microfluidic device, we used a 3D O_2 transport model of O_2 in the microfluidic device [20]. The model predicted that channels with a larger height to width ratio were able to cause a large drop in PO_2 in the channel. This consideration was weighed against the stability of high aspect ratio PDMS channels. Resolution of the micro-milling system was also a consideration. Smaller channels could be obtained by photolithography, though micro-milling was a cheaper alternative for prototyping. In this study we used a channel that was 500 µm high by 300 µm wide (Figure 6.4). The model also suggested that the PDMS spin coat layer should be made as small as practical. Various spin-coating speeds were used to produce
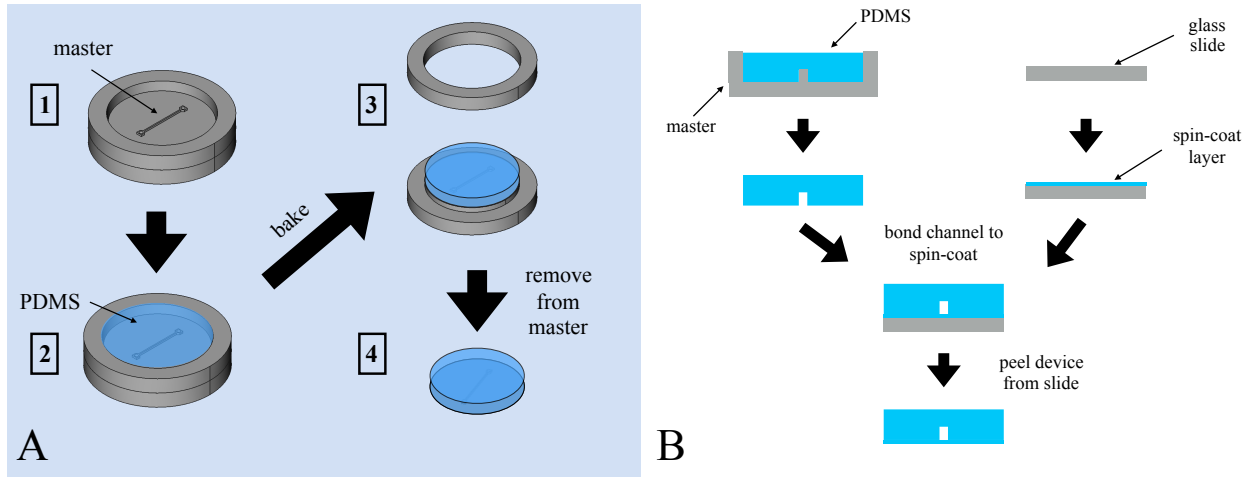
Figure 6.3: *Schematic of the fabrication process. Panel A shows a 3D CAD model of the master to form the PDMS channel. Step 3 shows the removable walls of the master which facilitates PDMS removal. Panel B shows a schematic of the fabrication process. PDMS is added to the master, cured and removed from the master. PDMS is spin-coated to a glass slide where is it partially cured. The two pieces are brought into conformal contact and fully cured.*

PDMS spin coats in the range of 5 to 100 µm; the devices were peeled from the glass surface and inspected for tears in the membrane. The thinest, practical PDMS spin coat layer was approximately 15-25 µm.

6.2.3   Experimental Setup

Whole blood was collected from the arterial line of anesthetized Sprague-Dawley rats into a heparinized vacutainer tubes. RBCs were isolated by centrifugation (2000 rpm for 3 minutes) and suspended in a physiological buffer solution (2.545 mg/mL $(CH_2OH)_3CNH_2$, 8.210 mg/mL NaCl, 0.350 mg/mL KCl, 0.295 mg/mL $CaCl_2 2H_2O$, 0.290 mg/mL $MgSO_4 7H_2O$, 5.000 mg/mL bovine albumin, 1.000 mg/mL D-glucose; pH of 7.4). Centrifugation and resuspension were repeated three times to ensure the solution was free of clotting agents.

The RBC solution was driven through the microfluidic device via polyethylene tubing (PE50); the flow rate was controlled by gravity feed. The system temperature was monitored using a thermocouple and controlled to 37 °C using a heat lamp; the heat lamp was
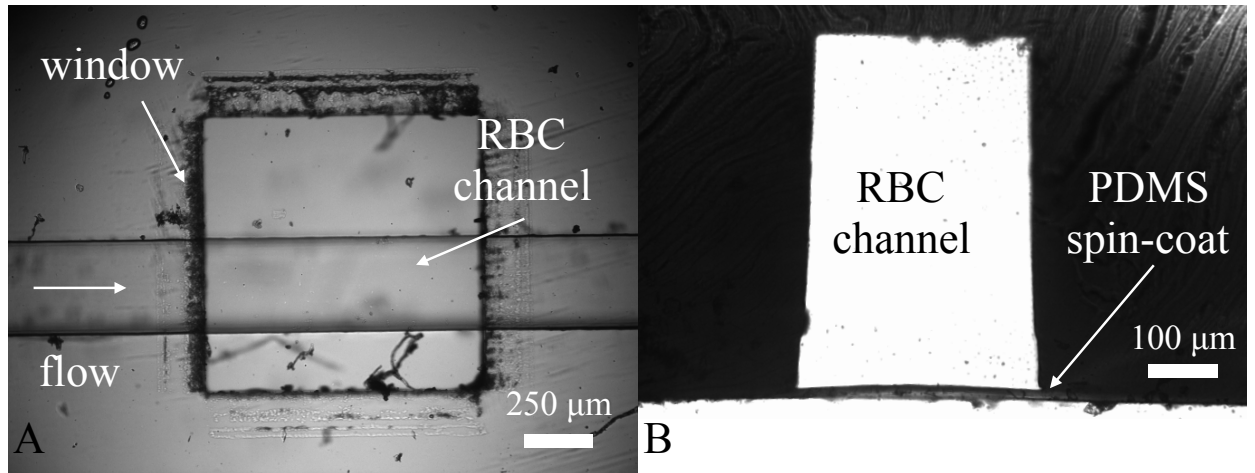
Figure 6.4: *Micrograph of the microfluidic device. Panel A shows a 10X micrograph of the microfluidic device assembled with the glass slide with the gas exchange window (1×1 mm). Panel B shows a 20X micrograph of the device cross-section orthogonal to the flow direction. The channel dimensions are approximately 500×300 µm. The PDMS spin coat layer thickness varies between approximately 18-28 µm.*

turned off during capture to prevent optical artifacts.

6.2.4   RBC SO$_2$ Measurement

RBCs were imaged on an Olympus IX-81 microscope at 20X magnification. Images were captured at approximately 30 frames per second using a Hamamatsu digital camera (ORCA Flash4.0). The transmitted light was split into two using a beam splitter (Cairn Optosplit Bypass) to two different 10 nm band pass filters centred at 442 nm and 454 nm. Each beam of filtered light was projected onto one half of the digital camera charged coupled device (CCD). In this configuration, both filters are recorded simultaneously.

Image analysis was done in MATLAB 2016b (MathWorks Inc.). Hemoglobin oxygen saturation of RBCs was determined using the ratio of optical densities as described in [26]. The optical densities were calculated using the diffusion-based inpainting method described in [27]. The high spatial resolution of the Hamamatsu cameras enabled the calculation of SO$_2$

on a pixel-by-pixel basis.

Briefly, SO_2 can be calculated from the ratio of optical densities according to

$$SO_2 = \frac{b_1 - b_2 R}{a_2 R - a_1} \tag{6.1a}$$

$$a_i = \varepsilon_{Hb_{O_2}}(\lambda_i) - \varepsilon_{Hb}(\lambda_i) \tag{6.1b}$$

$$b_i = \varepsilon_{Hb}(\lambda_i) \tag{6.1c}$$

$$R = \frac{OD(\lambda_1)}{OD(\lambda_2)}, \tag{6.1d}$$

where $OD(\lambda)$ is optical density at wavelength λ; λ_1 is 454 nm and λ_2 is 442 nm. $\varepsilon_{Hb_{O_2}}$ and $\varepsilon_{Hb}(\lambda_i)$ are the extinction coefficients of fully oxygen saturated and desaturated hemoglobin, respectively. Figure 6.5 shows the hemoglobin extinction coefficients as a function of wavelength for fully oxygen saturated and fully oxygen desaturated hemoglobin, as tabulated in [28].

Optical densities of individual RBCs were calculated on a pixel-by-pixel basis; this was done by capturing stationary RBCs on the bottom surface of the microfluidic in two fields of view, one centred at the beginning of the window the second centred at the end of the window. The median optical density for each RBC was reported. RBCs were not included in the calculation if they were obscured by other objects in the image.

6.2.5   ATP Measurement

ATP concentrations were measured using a luciferin and luciferase cocktail. 5 mg of D-luciferin (Sigma-Aldrich Co.) was diluted into 10 mL of physiological buffer solution. 20 mg of luciferase (Sigma-Aldrich Co.) was diluted in 2 mL of physiological buffer. The
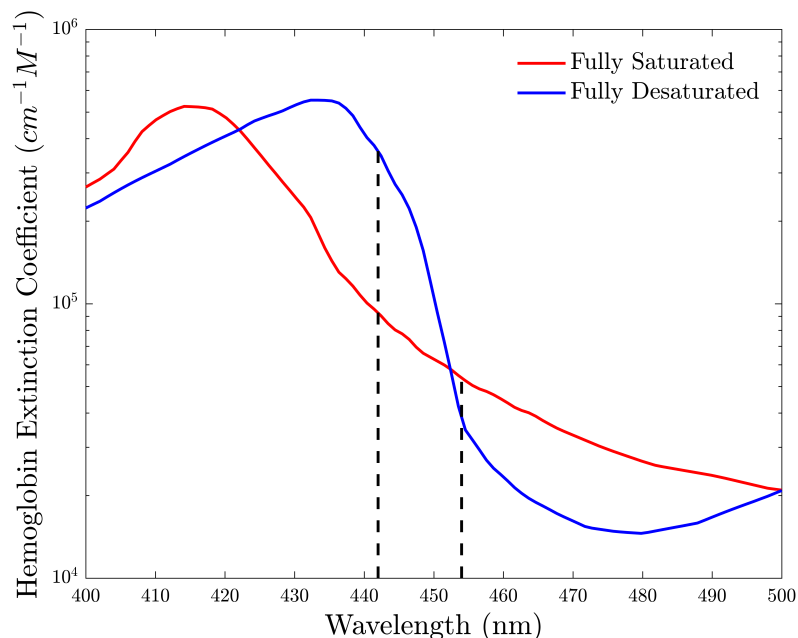
Figure 6.5: *Extinction coefficients of fully oxygen saturated and fully desaturated hemoglobin as a function of wavelength. The black dashed lines indicate the wavelengths used in this study. Data were compiled from [28].*

luciferin and luciferase dilutions were mixed one-to-one to produce the final mixture; the mixture was allowed to stand for 20 minutes before use. ATP standards were prepared by serial dilution of 5 mg of ATP sodium salt in 1 mL of H_2O. Measurements were made using either a QuantEM EMCCD digital camera or a Photon Technology International D-104 photometer.

125 µL of luciferase cocktail was added to a blackout chamber placed over the objective of the microscope. 250 µL of ATP was added after a one minute baseline recording. We used a 15 s exposure for the EMCCD camera and a 1 s exposure for the photometer. Measurements were made using a 4X objective in a dark room. In both methods, the peak intensity was compared to the baseline.

6.3   Results

6.3.1   SO$_2$ Measurements

As discussed in Section 6.2.4, RBC SO$_2$ can be measured using the optical properties of RBCs. Specifically, it can be calculated from the ratio of optical densities at two wavelengths, where optical density is given by the logarithm (base 10) of the ratio of incident light intensity to transmitted light intensity. The transmitted light intensity is measured by the pixel intensity, and incident light intensity is estimated using diffusion-based inpainting as described in [27]. Figure 6.6 shows 20X microscopy images of stationary RBCs at the bottom surface of the microfluidic device at two wavelengths (442 and 454 nm). This figure visibly shows a change in red blood cell absorption in the 442 nm wavelength. Very little change can seen in the 454 wavelength; this is because at this wavelength, hemoglobin absorption is close to isosbestic (i.e. independent of SO$_2$; see Figure 6.5). This figure demonstrates that RBCs exposed to low oxygen over the window have a higher optical density as would be expected for desaturated cells.

Median RBC optical densities of individual RBCs as a function of position downstream in the microfluidic device are shown in Figure 6.7. Data were taken from two fields of view at the beginning and end of the exchange window; data in the middle of the window were not included since no fiducial markers were present to allow for the spatial positioning of the data relative to the window. Outside of the window, optical densities are similar in both wavelengths, while inside the window there is an increase in optical density at the 442 nm wavelength in the window and a decrease in optical density at the 454 nm wavelength. This figure also shows the optical density ratio, R (optical density at 454 nm divided by optical density at 442 nm). The optical density ratio begins high outside the window and drops rapidly in the window; the optical density ratio starts to drop before the window.
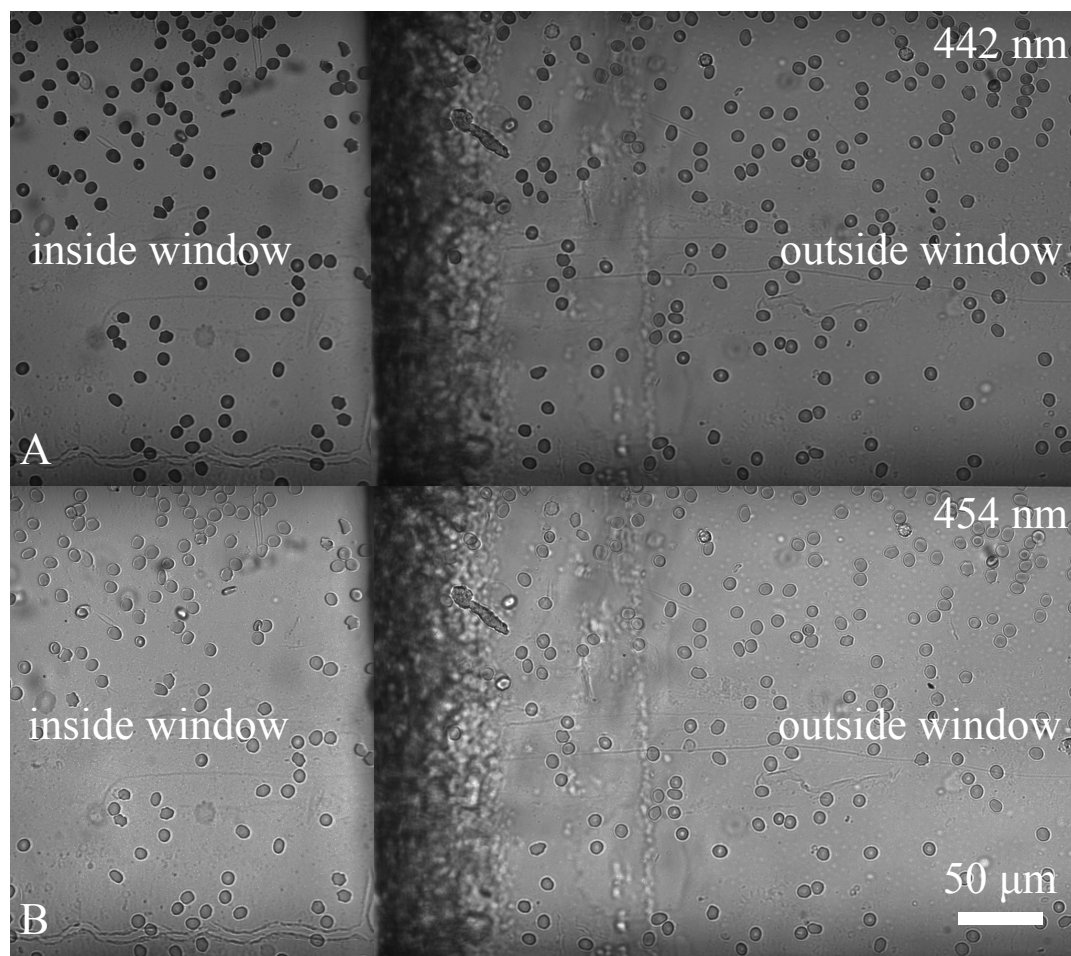
Figure 6.6: *Images of RBCs in the microfluidic device are shown for wavelengths 442 nm (A) and 454 (B) inside and outside of the oxygen exchange window. Due to the optical properties of the microfluidic device, RBCs at the same depth inside and outside of the window are in different focal planes. Thus for the purpose of this figure two images are stitched together to show inside and outside the window at the same time.*
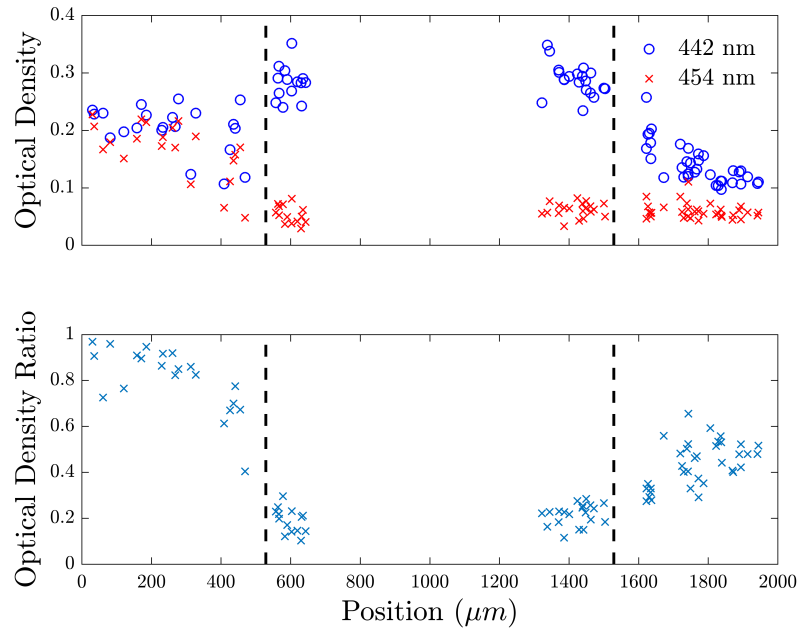
Figure 6.7: *Optical density of red blood cells as a function of position downstream in the microfluidic device. The top panel shows the optical density at 442 nm (blue) and 454 nm (red). The bottom panel shows the ratio of the optical density at 454 nm to the optical density at 442 nm. The dashed lines indicate the edges of the O_2 exchange window.*

To quantify the change in saturation, the optical density ratio can be related to SO_2 using the extinction coefficients of hemoglobin at both wavelengths (see Section 6.2.4). Figure 6.8 shows the relationship used to calculate SO_2; it was calculated with Equation 6.1 using the extinction coefficients of fully saturated and desaturated hemoglobin at 442 and 454 nm. It is important to note that this relationship assumes that the filters used are perfect zero-width bandpass filters centred at their corresponding wavelengths; in reality, our filters have non-perfect 10 nm bandpasses.

Figure 6.9 shows SO_2 as a function of position. We displayed the solution to a simple 1D analytical model of O_2 transport described in [20] on the same axis to demonstrate that the data are consistent with the physical model. Four free parameters were used to fit the data (Pe, S_1 and S_2 from the model presented by Sové *et al.* [20] and a scaling factor to allow the model to have saturations greater than 1). The Hill equation was used to convert the model from oxygen tension to SO_2 ($N = 2.7$, $P_{50} = 37$ mmHg). This figure demonstrates

the rapid change in O_2 in the channel. These results demonstrate the device's ability to rapidly desaturate the RBCs within 200 µm. SO_2 values range from 1.13 before the window to 0.02 in the window. The values greater than one are likely due to the simplifications made in the optical density ratio-SO_2 relationship.
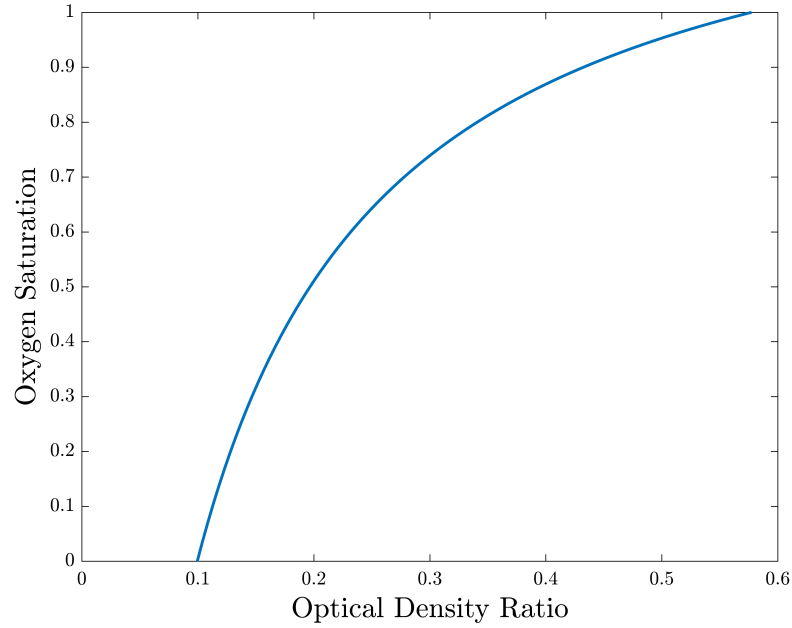
Figure 6.8: *Relationship between the ratio of the optical density at 454 nm to the optical density at 442 nm and RBC SO_2.*
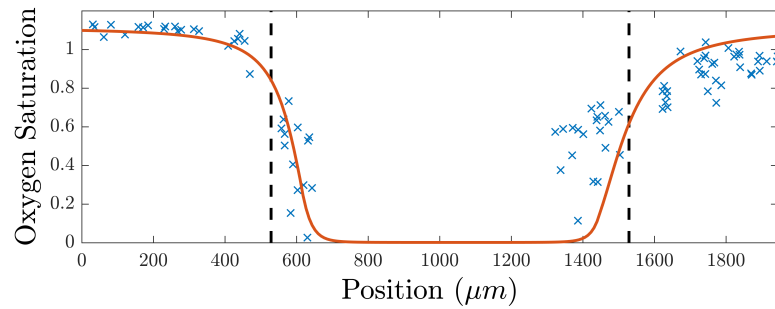
Figure 6.9: *SO_2 as a function of position downstream in the microfluidic device. Each data point is calculated from the optical density ratios in Figure 6.7 using the relationship in Figure 6.8. The black dashed lines indicate the position of the window. For comparison, the solution to a 1D model of O_2 transport proposed in [20] (red; $Pe = 1$, $S_1 = 6$ and $S_2 = 300$) is displayed on the same axis. The model was scaled to fit the data.*

6.3.2 ATP Measurements

We performed ATP standard measurements to determine the minimum ATP concentration we could detect. For this, ATP solutions of various concentrations were injected into a blackout chamber with the luciferase cocktail. The corresponding light flux was measured with either an EMCCD camera or a photometer. Figure 6.10 shows an example ATP standard curve measured with the EMCCD camera with a 15 s exposure. Each concentration was repeated three times. This result indicates the lower limit of the detection of ATP is between 1×10^{-8} and 1×10^{-7} M. Although designed to use with CCD camera, preliminary tests with a photometer show increased sensitivity; using a 1 s exposure, the photometer can read ATP concentrations as low as 1×10^{-9} M.
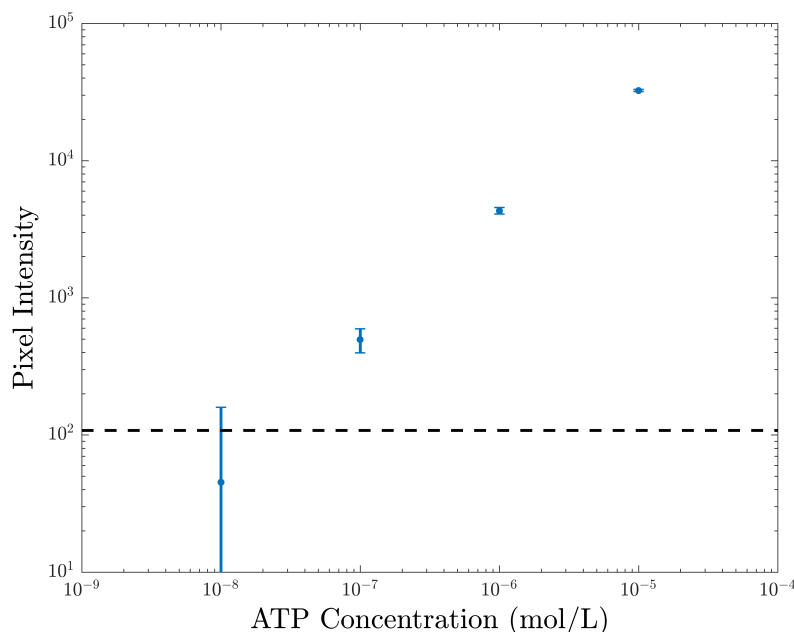
Figure 6.10: *ATP standard curve for EMCCD camera. Each data point represents the mean pixel intensity of the peak frame minus the mean pixel intensity of the baseline frames. Error bars represent standard deviation of the peak frame. The dashed line indicates the standard deviation of baseline frames.*

6.4   Discussion

This work presents the design and fabrication of a microfluidic device designed to cause a rapid spatial change in RBC SO_2 for the measurement of O_2-dependent ATP release from RBCs. We demonstrate that this device is able to cause a large, rapid change in RBC SO_2 that is localized around the gas exchange window. To quantify the sensitivity of our experimental system and in particular, to determine the practicality of using an EMCCD camera for the measurement of ATP, we have determined the minimum ATP concentration we can measure using our camera to be on the order of 1×10^{-7} M. Finally, we explored the possibility of using a photometer to measure ATP release, since this was the method Wan *et al.* [18] used; preliminary results suggest that this system would be more sensitive than the EMCCD system.

The design of the device presented in this work was inspired by a similar design by Wan and colleagues in 2008, where they measured ATP release time for the shear-dependent release of ATP from RBCs using a microfluidic device. The shear stress was induced using a constriction in the microfluidic device such that there was a spatial change in shear in a time-invariant flow. ATP concentration was measured at various positions along the microfluidic device using a firefly luciferase assay with a photometer. In their setup, ATP release time was determined by measuring the distance between the beginning of the constriction and the start of the increase in ATP concentration and using the average RBC speed to get release time [18].

The objective of our current research is to adapt Wan's experiment for the measurement of ATP release time for the O_2-dependent release of ATP from RBCs. Though there are many similarities between the two protocols, inducing a rapid change in RBC oxygenation is far from straight-forward. To cause the spatial change in O_2, we proposed to replace the constriction in the microfluidic device with a gas exchange window. However, due to

the nature of molecular diffusion, ensuring the change is large enough and spatially confined is a challenge. This challenge was first addressed using mathematical modelling of an idealized microfluidic device to determine if the experiment was theoretically feasible [19]. In particular, we determined that we could induce a spatial change in RBC SO_2 and that we could calculate ATP release time from the resulting light signal. This model was also used to demonstrate the sensitivity of the change in SO_2, and as a result released ATP, to various experimental parameters such as the channel height and flow rate. An important consideration in the experimental design is to choose a flow rate that is slow enough to induce a large enough change in O_2 but fast enough to achieve a sufficient temporal resolution.

One of the largest impeding factors was the fabrication of the microfluidic device. The device Wan used was fabricated in PDMS, which is one the most common materials for microfluidic fabrication in academic laboratories [24]. The concern is that PDMS is a highly O_2-permeable material, which complicates the predictions of the RBC desaturation made with the idealized microfluidic device. To address this complication, a 3D O_2 transport model was used to optimize the geometric dimensions of the microfluidic device [20]. In the current study, we developed the protocol to fabricate the PDMS-based microfluidic device designed in [20].

To determine how effective the microfluidic device is at desaturating RBCs, we measured SO_2 in the device using a dual wavelength spectroscopy method. In our lab, these measurements are typically made in our intravital video preparation to assess capillary oxygenation [21, 29]. In these protocols, SO_2 measurements are made for in-focus RBCs flowing single file through a capillary, and incident light intensity is calculated as the maximum intensity in a sequence of images. Adapting these methods for use *in vitro* presents several challenges. Firstly, in the intravital studies, RBCs are deformed as they flow through the capillaries. When flowing freely in the microfluidic device, they are not deformed and lens the background light. Additionally, RBCs in the microfluidic device change focal planes, making it

difficult to choose a focal plane for the measurement the optical densities of moving RBCs. Therefore, we decided to only measure SO_2 of stationary RBCs on the bottom surface of the microfluidic device; these RBCs experience the largest change in SO_2 while flowing RBCs deeper in the channel will experience a smaller change. Since the background intensity of lensed and stationary cells cannot be done using the maximum intensity image, we instead use the newly proposed inpainting method [27].

Ultimately, the device should have the temporal resolution to measure ATP release time. For O_2-dependent release, ATP release time was suggested to be less than 500 ms based on the transit time of RBCs in an isolated arteriole preparation exposed to low O_2 [2]. If it is similar to that of shear-dependent release, it is likely to be between 25-75 ms as found in [18]. Since ATP release time is measured by a spatial displacement, temporal resolution is affected by two factors (1) the spatial resolution of the detector and (2) the RBC velocity. In the study by Wan *et al.*, the average RBC velocity through the constriction in their channel was 60 mm/s; this rapid RBC velocity gave them a large temporal resolution. In our system, RBC velocity influences SO_2 such that a larger velocity reduces the drop in SO_2 [19, 20]. Additionally, high RBC velocity results in high shear stress which may elicit a shear-dependent response. Therefore, using a large RBC velocity is problematic in our application, limiting our temporal resolution; thus, this application requires excellent spatial resolution of the detector. In our system, preliminary tests were done using an EMCCD digital camera with a CCD array of 512 by 512 pixels. At 4X magnification, this corresponds to a spatial resolution of approximately 3.5 μm. Assuming an average RBC velocity of 0.08 mm/s, this corresponds to a 44 ms temporal resolution.

A final consideration is whether the detector has the sensitivity to measure the resulting concentration of ATP from O_2-dependent release. We have determined that the detection limit of the EMCCD camera is of the order of 1×10^{-7} M. Wan *et al.* reported peak concentrations on the order of 1×10^{-6} M in their device. If the O_2-dependent mechanism releases

at a similar rate, the system can detect it; this assumes the number of RBCs affected by the stimulus is similar in both devices. An alternative to a CCD array is to use a photometer, as in [18]. However, to achieve a high spatial resolution throughout the channel, numerous closely spaced point measurements are required. With a photometer, this procedure requires manually translating the detector along the channel. Using a CCD array allows for the simultaneous capture of point measurements of a large region of the channel, but is less sensitive than a photometer. Therefore, if the CCD array is not sensitive enough to measure the ATP signal, a photometer may be used.

Using this device to measure ATP release time will strongly support the hypothesis that RBCs release ATP in response to desaturation. Recent reports in the literature have suggested that hemolysis may responsible for most or all ATP release measured *in vitro* due to hypotonic shock, shear stress, and hypoxia [30, 31]. This device can rule out hemolysis as a cause, since cell lysis would not occur in a time-invariant manner; thus the steady-state signal would only reflect the O_2-dependent release.

In addition to determining ATP release time, this device could be used to study the dynamics of O_2-dependent ATP release in both health and disease. For example, healthy RBCs could be used with signalling pathway inhibitors to help determine the mechanism for ATP release. Further, since impairments in ATP release have been linked to various diseases [14, 16, 17], this device could be used as a screening tool.

In summary, we have developed an *in vitro* tool to rapidly desaturate RBCs spatially for the purpose of measuring the dynamics of O_2-dependent ATP release. The device is capable of causing a rapid and large spatial desaturation. Our CCD camera approach is able to detect ATP concentrations on the order of 1×10^{-7} M. This work presents an important step forward in the study of O_2-dependent release of ATP from RBCs as a mechanism for O_2 regulation in the microcirculation.

References

[1] M. L. Ellsworth, T. Forrester, C. G. Ellis, and H. H. Dietrich, "The erythrocyte as a regulator of vascular tone," *American Journal of Physiology-Heart and Circulatory Physiology*, vol. 269, no. 6, pp. H2155–H2161, 1995.

[2] H. H. Dietrich, M. L. Ellsworth, R. S. Sprague, and R. G. Dacey Jr, "Red blood cell regulation of microvascular tone through adenosine triphosphate," *American Journal of Physiology-Heart and Circulatory Physiology*, vol. 278, no. 4, pp. H1294–H1298, 2000.

[3] M. L. Ellsworth, C. G. Ellis, D. Goldman, A. H. Stephenson, H. H. Dietrich, and R. S. Sprague, "Erythrocytes: oxygen sensors and modulators of vascular tone," *Physiology*, vol. 24, no. 2, pp. 107–116, 2009.

[4] C. G. Ellis, S. Milkovich, and D. Goldman, "What is the efficiency of ATP signaling from erythrocytes to regulate distribution of O_2 supply within the microvasculature?," *Microcirculation*, vol. 19, no. 5, pp. 440–450, 2012.

[5] L. Corr and G. Burnstock, "Analysis of P2-purinoceptor subtypes on the smooth muscle and endothelium of rabbit coronary artery.," *Journal of Cardiovascular Pharmacology*, vol. 23, no. 5, pp. 709–715, 1994.

[6] A. Rubino, V. Ralevic, and G. Burnstock, "Contribution of P1 (A2b subtype) and P2-purinoceptors to the control of vascular tone in the rat isolated mesenteric arterial bed," *British Journal of Pharmacology*, vol. 115, no. 4, pp. 648–652, 1995.

[7] W. T. McCullough, D. M. Collins, and M. L. Ellsworth, "Arteriolar responses to extracellular ATP in striated muscle," *American Journal of Physiology-Heart and Circulatory Physiology*, vol. 272, no. 4, pp. H1886–H1891, 1997.

[8] D. M. Collins, W. T. McCullough, and M. L. Ellsworth, "Conducted vascular responses: communication across the capillary bed," *Microvascular Research*, vol. 56, no. 1, pp. 43–53, 1998.

[9] M. Malmsjö, D. Erlinge, E. D. Högestätt, and P. M. Zygmunt, "Endothelial P2Y receptors induce hyperpolarisation of vascular smooth muscle by release of endothelium-derived hyperpolarising factor," *European journal of pharmacology*, vol. 364, no. 2, pp. 169–173, 1999.

[10] G. Bergfeld and T. Forrester, "Release of ATP from human erythrocytes in response to a brief period of hypoxia and hypercapnia," *Cardiovascular Research*, vol. 26, no. 1, pp. 40–47, 1992.

[11] R. S. Sprague, M. L. Ellsworth, A. H. Stephenson, and A. J. Lonigro, "ATP: the red blood cell link to no and local control of the pulmonary circulation," *American Journal of Physiology-Heart and Circulatory Physiology*, vol. 271, no. 6, pp. H2717–H2722, 1996.

[12] D. B. Light, T. L. Capes, R. T. Gronau, and M. R. Adler, "Extracellular ATP stimulates volume decrease in Necturus red blood cells," *American Journal of Physiology-Cell Physiology*, vol. 277, no. 3, pp. C480–C491, 1999.

[13] J. E. Jagger, R. M. Bateman, M. L. Ellsworth, and C. G. Ellis, "Role of erythrocyte in regulating local O_2 delivery mediated by hemoglobin oxygenation," *American Journal of Physiology-Heart and Circulatory Physiology*, vol. 280, no. 6, pp. H2833–H2839, 2001.

[14] R. S. Sprague, A. H. Stephenson, E. A. Bowles, M. S. Stumpf, and A. J. Lonigro, "Reduced expression of Gi in erythrocytes of humans with type 2 diabetes is associated with impairment of both cAMP generation and ATP release," *Diabetes*, vol. 55, no. 12, pp. 3588–3593, 2006.

[15] M. S. Hanson, M. L. Ellsworth, D. Achilleus, A. H. Stephenson, E. A. Bowles, M. Sridharan, S. Adderley, and R. S. Sprague, "Insulin inhibits low oxygen-induced atp release from human erythrocytes: Implication for vascular control," *Microcirculation*, vol. 16, no. 5, pp. 424–433, 2009.

[16] C. G. Ellis, D. Goldman, M. Hanson, A. H. Stephenson, S. Milkovich, A. Benlamri, M. L. Ellsworth, and R. S. Sprague, "Defects in oxygen supply to skeletal muscle of pre-diabetic ZDF rats," *American Journal of Physiology-Heart and Circulatory Physiology*, vol. 298, no. 6, pp. H1661–H1670, 2010.

[17] R. M. Bateman, M. D. Sharpe, J. E. Jagger, and C. G. Ellis, "Sepsis impairs microvascular autoregulation and delays capillary response within hypoxic capillaries," *Critical Care*, vol. 19, no. 1, p. 389, 2015.

[18] J. Wan, W. D. Ristenpart, and H. A. Stone, "Dynamics of shear-induced ATP release from red blood cells," *Proceedings of the National Academy of Sciences*, vol. 105, no. 43, pp. 16432–16437, 2008.

[19] R. J. Sové, N. Ghonaim, D. Goldman, and C. G. Ellis, "A computational model of a microfluidic device to measure the dynamics of oxygen-dependent ATP release from erythrocytes," *PLOS ONE*, vol. 8, p. e81537, Nov. 2013.

[20] R. J. Sové, G. M. Fraser, D. Goldman, and C. G. Ellis, "Finite element model of oxygen transport for the design of geometrically complex microfluidic devices used in biological studies," *PLOS ONE*, vol. 11, no. 11, p. e0166289, 2016.

[21] R. J. Sové, S. Milkovich, H. Nikolov, D. Holdsworth, G. M. Fraser, and C. G. Ellis, "Localized oxygen exchange platform for intravital video microscopy for the investigation of microvascular oxygen regulation," *in preparation*, 2018.

[22] S. Nikumb, Q. Chen, C. Li, H. Reshef, H. Zheng, H. Qiu, and D. Low, "Precision glass machining, drilling and profile cutting by short pulse lasers," *Thin Solid Films*, vol. 477, no. 1-2, pp. 216–221, 2005.

[23] D. C. Duffy, J. C. McDonald, O. J. A. Schueller, and G. M. Whitesides, "Rapid prototyping of microfluidic systems in poly(dimethylsiloxane)," *Analytical Chemistry*, vol. 70, pp. 4974–4984, Oct. 1998.

[24] J. C. McDonald, D. C. Duffy, J. R. Anderson, D. T. Chiu, and H. Wu, "Fabrication of microfluidic systems in poly(dimethylsiloxane)," *Electrophoresis*, no. 21, pp. 27–40, 2000.

[25] J. S. Go and S. Shoji, "A disposable, dead volume-free and leak-free in-plane PDMS microvalve," *Sensors and Actuators A: Physical*, vol. 114, no. 2, pp. 438–444, 2004.

[26] S. A. Japee, R. N. Pittman, and C. G. Ellis, "A new video image analysis system to study red blood cell dynamics and oxygenation in capillary networks," *Microcirculation*, vol. 12, no. 6, pp. 489–506, 2005.

[27] R. J. Sové, N. E. Drakos, G. M. Fraser, and C. G. Ellis, "Using digital inpainting to estimate incident light intensity for the calculation of red blood cell oxygen saturation from microscopy images," *accepted to Journal of Biophotonics*, 2018.

[28] S. Prahl, "Optical absorption of hemoglobin," tech. rep., Oregon Medical Laser Center, 1999.

[29] N. W. Ghonaim, L. W. Lau, D. Goldman, C. G. Ellis, and J. Yang, "A micro-delivery approach for studying microvascular responses to localized oxygen delivery," *Microcirculation*, vol. 18, no. 8, pp. 646–654, 2011.

[30] J. Sikora, S. N. Orlov, K. Furuya, and R. Grygorczyk, "Hemolysis is a primary atp-release mechanism in human erythrocytes," *Blood*, vol. 124, no. 13, pp. 2150–2157, 2014.

[31] A. S. Keller, L. Diederich, C. Panknin, L. J. DeLalio, J. C. Drake, R. Sherman, E. K. Jackson, Z. Yan, M. Kelm, M. M. Cortese-Krott, *et al.*, "Possible roles for ATP release from RBCs exclude the cAMP-mediated Panx1 pathway," *American Journal of Physiology-Cell Physiology*, vol. 313, no. 6, pp. C593–C603, 2017.

Chapter 7

Final Summary

The regulation of O_2 distribution in the microcirculation is a complex control system that can adjust vascular tone to alter the distribution of RBCs to precisely match O_2 supply with O_2 demand. Numerous researchers provide evidence for the existence of an O_2-dependent mechanism for O_2 regulation, however, the location of the O_2 sensor remains unclear [1]. The goal of this thesis was to develop tools to facilitate the study of the regulation of O_2 distribution in the microcirculation by applying concepts in mathematics, physics and engineering. In this thesis, we took a two-tiered approach. First, at the level of the microvasculature, we developed a gas exchange device that allows for the local manipulation of capillary RBC SO_2 *in vivo* to study the spatial dependence of ATP release. Secondly, to study one of the proposed sensors, the RBC, directly, we developed an *in vitro* device capable of causing rapid changes in SO_2. Due to the challenges associated with the development and analysis of the experimental tools, extensive computational modelling was done. Challenges in measuring RBC SO_2 in the *in vitro* microfluidic device motivated the need for an image processing technique to calculate the RBC SO_2 from light microscopy images; this new technique was also applicable to measurements *in vivo*. At a high level, this thesis:

1. presents the novel design for a modular gas exchange platform that was demonstrated to cause perturbations in RBC SO_2 *in vivo* both experimentally and computationally,

2. demonstrates that localized changes in RBC SO_2 in an isolated group of capillaries

can elicit a flow response,

3. proposes a experiment to measure the dynamics of O_2-dependent ATP release from RBCs using a novel microfluidic device design,

4. explores the feasibility of this experimental approach using a comprehensive mathematical model of the experimental system,

5. presents a computational model of O_2 transport throughout the wall and channels of the microfluidic device proposed above for the optimization of various geometric parameters,

6. demonstrates the use of digital inpainting to calculate the incident light intensity in microscopy images for calculation of RBC SO_2 overcoming many deficiencies with the methodology currently used in the field,

7. presents the construction and experimental validation of the microfluidic device to cause a localized spatial deoxygenation of RBCs.

In this chapter, the main results from each study of this thesis are summarized, followed by a discussion of the future directions of this work.

7.1   Summary of Results

In 2011, our lab developed an O_2 delivery platform capable of causing changes in capillary O_2 saturation (SO_2) limited to a small area of tissue in an intravital video microscopy system [2]. Although the O_2 exchange platform induced changes in red blood cell (RBC) SO_2, corresponding changes in supply rate were not reported [2]. This method was altered to increase the surface area for exchange; a 100 μm diameter circular exchange area was replaced by a 1000 by 200 μm rectangular area. As predicted by computational studies [3], this modification was able to elicit a vascular response despite causing similar changes in

capillary SO_2 [4]; the difference was the number of affected capillaries. Although this setup was able to elicit a vascular response to O_2, ideally we would have a more localized stimulus. Another challenge with the previous apparatus is that it could only resolve capillaries within 60 µm from the surface of the tissue.

In Chapter 2, we developed an O_2 delivery platform with a smaller exchange area that is also thin enough to allow us to focus on capillaries deeper throughout the muscle. A GPU-accelerated, 3D O_2 transport model of diffusion through the tissue was implemented to estimate the extent of the change in tissue oxygenation. The O_2 exchange platform is able to cause changes in RBC SO_2 of capillaries close to the window. Further, these changes resulted in corresponding changes in RBC supply rate. The computational model predicted the drop in O_2 is confined to 80 µm from the edge of the window. Overall, we have developed an O_2 delivery system that is capable of causing localized changes in SO_2 which can be used to further investigate microvascular O_2 regulation. The observation that RBC supply rate was tightly linked to the imposed changes in RBC SO_2 inspired our interest in the role of RBCs in O_2 sensing and regulation.

RBCs have been proposed to be a sensor in blood flow regulation through the O_2-dependent release of ATP, a potent vasodilator. Chapters 3, 4 and 6 focus on the development of an experimental device that will allow for the rapid desaturation of RBCs in order to study this potential mechanism in isolation. In 2008, a study at Harvard measured the dynamics of shear-dependent ATP release from RBCs using a microfluidic device with a constriction in the channel to increase shear stress [5]. The brief period of increased shear stress resulted in ATP release within 25 to 75 milliseconds downstream of the constriction. Thus our goal is to apply a similar approach to determine the dynamics of O_2-dependent ATP release. In the place of the constriction, an O_2-permeable membrane interfaced with a low O_2 gas exchange chamber would be used to decrease the SO_2 of the RBCs flowing through the channel.

Chapter 3 describes the first stage in achieving this goal: the development of a computational model of the proposed experimental system to determine the feasibility of altering SO_2 rapidly enough to measure ATP release dynamics. The computational model was constructed based on hemodynamics, molecular transport of oxygen and ATP, kinetics of luciferin/luciferase reaction for reporting ATP concentrations, light absorption by hemoglobin, and sensor characteristics. A linear model of oxygen saturation-dependent ATP release with variable time delay was used in this study. The computational results demonstrate that a microfluidic device with a 100 µm deep channel will cause a rapid decrease in oxygen saturation over the oxygen-permeable membrane that yields a measurable light intensity profile. The simulation also demonstrates that the complex dynamics of ATP release from erythrocytes with ATP degradation by luciferin/luciferase in a flowing system results in light intensity values that are not directly related to ATP concentrations. A computational model is required for proper interpretation of experimental data.

The idealized microfluidic device described in Chapter 3 assumed the device was fabricated using an O_2-impermeable material with an O_2-permeable window for gas exchange. Considerations to cost and ease of fabrication motivated a new design. With the fast emergence of microfluidics, non-specialist are able to rapidly prototype microfluidic devices in PDMS [6]. Unfortunately, this revision had a substantial impact on our original design, since PDMS is highly O_2-permeable. This motivated the need for a flexible 3D computational model of O_2 transport.

In Chapter 4, oxygen transport simulations were used to optimize the geometric design parameters for a similar system which is easier to fabricate using PDMS soft lithography techniques. The system is composed of a microfluidic device stacked on top of a large, gas-impermeable flow channel with a window to allow gas exchange. The microfluidic device is fabricated using soft lithography in polydimethyl-siloxane, an oxygen-permeable material. Our objective was twofold: (1) optimize the parameters of our system and (2) develop a

method to assess the oxygen distribution in complex 3D microfluidic device geometries. 3D simulations of oxygen transport were performed to simulate oxygen distribution throughout the device. The simulations demonstrate that microfluidic device geometry plays a critical role in molecule exchange, for instance, changing the orientation of the short wide microfluidic channel results in a 97% increase in oxygen exchange. Since microfluidic devices have become a more prominent tool in biological studies, understanding the transport of oxygen and other biological molecules in microfluidic devices is critical for maintaining a physiologically relevant environment. We have also demonstrated a method to assess oxygen levels in geometrically complex microfluidic devices.

To experimentally validate the ability of the microfluidic device to desaturate RBCs, SO_2 can to be measured in the device by taking advantage of spectroscopic properties of hemoglobin. When this technique is applied to transmission microscopy, the calculation of saturation requires determination of incident light intensity at each pixel occupied by the RBC; this value is often approximated from a sequence of images as the maximum intensity over time. This methods often fails in our microfluidic system since RBCs in the microfluidic device tend to lens light due to the biconcave shape of the RBC. This lensing artifact causes a ring of high intensity light around the RBC, causing the maximum intensity-based algorithm to fail. RBCs in capillaries must deform to pass through the narrow vessel, in this configuration there are fewer artifacts, thus this problem is less confounding to *in vivo* measurements. In addition, the maximum intensity-based method is not suitable to measure SO_2 of stationary cells.

Therefore, in Chapter 5, we propose a new way of approximating incident light intensity using digital inpainting. The proposed method estimates incident light intensity with a percent error of approximately 3% on average, which exceeds the accuracy of the maximum intensity based method in most cases. The error in incident light intensity corresponds to a maximum error of approximately 2% saturation. Therefore, though this new method is

computationally more demanding than the traditional technique, it can be used in cases where the red maximum intensity-based method fails (e.g. stationary cells), or when higher accuracy is required. It can also be used to measure SO_2 in the microfluidic device.

With all of the required tools in place, the objective of Chapter 6 was to present the design and development of the experimental system to control the spatial oxygenation of RBCs facilitating the measurement of the dynamics of ATP release. The experimental system consisted of two parts: our previously developed micro-delivery gas exchange platform and an O_2-permeable microfluidic device designed and refined using computational modelling. The gas exchange chamber was used to cause a localized change in O_2 in the microfluidic device such that the flowing RBCs suspended in physiological buffer would be experience a rapid change in O_2. To quantify the change, the newly developed inpainting method was used. RBCs in the microfluidic device were rapidly desaturated to near-zero SO_2. In future work, a firefly luciferase assay can be used to measure the position of ATP released from RBCs, which can then be used to determine ATP release time. We determined that the EMCCD camera is capable of detecting changes in ATP as low as 1×10^{-7} M; the photometer offers even better sensitivity detecting down to 1×10^{-9} M using a short exposure time of 1 s at the cost of lower spatial resolution. In summary, we have developed an experimental *in vitro* system to impose a spatial deoxygenation of RBCs in a steady flow microfluidic device to study the dynamics of O_2-dependent ATP release from RBCs.

7.2   Future Directions

In this thesis a variety of tools were developed to study the regulation of O_2 in the microcirculation. As such, this thesis serves as a basis that future researchers can use to answer exciting questions in physiology. The following section outlines potential applications of the developed tools.

Chapter 2 presented a device for the local desaturation of RBCs in capillaries *in vivo*. This device is capable of causing changes in O_2 limited to a handful of capillaries. With such a device, one could explore the potential location of the O_2 sensor in the microcirculation. For example, this device could be used to probe regions of the muscle absent of capillaries to determine whether the sensor may be extravascular. Further, consistent with the ATP release hypothesis, one could use this device to stimulate capillaries in one microvascular unit, to see whether a flow response is elicited in other micro vascular units attached to the same or different arterioles. This device could also be used to determine whether there are other factors controlling flow regulation other than passive rheology, such as pericytes. One could manipulate the SO_2 of multiple capillaries coming from the same arteriole to determine if the distribution of flow rates remains constant. Thus, this device allows for a number of future studies directed at perturbing the local oxygen microenvironment in the microcirculation.

Chapters 3, 4 and 6 presented the development of a device that could be used to measure the dynamics of O_2-dependent ATP release. This device would not only allow for the measurement of ATP release time, it could also serve as a confirmation that the ATP released is not due to hemolysis. However, before this device can be implemented, there are challenges that still need to be addressed.

For example, one challenge in measuring ATP is that hemoglobin absorption in the emission range of the luciferase reaction is high and O_2-dependent [7]. The firefly luciferase reaction emits light centered at 560 nm at 25 °C [8]. At this wavelength, hemoglobin absorbs more light when it is fully oxygen desaturated and thus, the same ATP concentration would appear to produce more light in RBCs exposed to high O_2. Furthermore, the wavelength emitted is also temperature-dependent and therefore absorption by hemoglobin would also have a temperature dependence. This may also have an impact on other *in vitro* measure-

ments of ATP release. This difficulty was overcome in the study by Jagger *et al.*, where whole blood was desaturated, but the ATP assay was perform on a dilution of the sample [9]. At low hematocrit, the absorption of light would be less, thus the effect of the oxygen dependence of the absorption would be minimal. Therefore, further refinements need to be made to the experimental protocol in order to measure ATP release dynamics.

After measuring the dynamics of ATP release in healthy blood, one could continue to explore the dynamics of ATP release in various pathological conditions. There have been various indications in the literature that ATP release may be impaired in various diseases including type II diabetes [10] and sepsis [11]. The system developed in this thesis may be used to determine whether the dynamics are also affected in disease; if so, it could be used clinically as a diagnostic tool.

As well as having clinical applications, the device can also be used to investigate the signalling pathway within the RBC. Some preliminary work done using a computational model of the cellular pathway for ATP release suggests the dynamics of ATP release would be altered when specific mechanisms in the pathway are perturbed (data not shown). In this preliminary work, a computational model of the pathway was developed by [12]. The computational model was then applied to the model of the experimental system developed in Chapter 3, replacing the ATP release module. This work had several interesting insights which can be pursued in the future. Firstly, ATP release turn-off time was different than ATP turn on-time. Secondly, impairment of specific mechanisms in the pathway leads to altered ATP release time; ATP turn-off time was affected more than ATP turn-on time. Therefore, computational modelling in conjunction with this microfluidic device could allow for the elucidation of the mechanism for ATP release.

In addition to the experimental tools, a set of computational tools were developed in order to design, evaluate and understand the experimental tools. For instance, in Chapter 4, a

3D model of O_2 transport was implemented using the finite element method to evaluate the efficacy of O_2 exchange in O_2-permeable microfluidic devices. This code was developed to be modular and can be used for any geometry. This program can be used in the development of future devices. Additionally, Chapter 5 describes an algorithm that estimates incident light intensity for the calculation of RBC SO_2. One important accomplishment of this algorithm is its ability to calculate SO_2 of stationary RBCs. This was useful for the quantification of the change in SO_2 in the microfluidic device, since we could measure SO_2 for cells adhering to the bottom walls of the device. Further, in sepsis, there are often very low flow or stopped flow vessels [13, 14], for which this algorithm could be used to determine SO_2. In future work, an automated RBC detection method can be implemented to facilitate the automation of inpainting. Once automated, inpainting can be incorporated into the existing analysis software for the calculation of SO_2.

7.3   Conclusion

In summary, this thesis has developed both *in vivo* and *in vitro* experimental tools, as well as computational tools to study the regulation of O_2 distribution in the microcirculation. Specifically, we have developed a microdelivery gas exchange platform to cause localized changes in capillary RBC SO_2 that result in a vascular flow response, and a microfludic device capable of rapidly desaturating RBCs to facilitate the measurement of the dynamics of O_2-dependent release of ATP from RBCs. To guide the development of these experimental devices, we also developed a set of computational and analytical tools including mathematical models of the physical devices and a novel approach to measuring RBC SO_2. Together these tools provide novel methodology that enable the pursuit of new avenues to advance the study of microvascular O_2 regulation.

References

[1] S. S. Segal, "Regulation of blood flow in the microcirculation," *Microcirculation*, vol. 12, no. 1, pp. 33–45, 2005.

[2] N. W. Ghonaim, L. W. Lau, D. Goldman, C. G. Ellis, and J. Yang, "A micro-delivery approach for studying microvascular responses to localized oxygen delivery," *Microcirculation*, vol. 18, no. 8, pp. 646–654, 2011.

[3] N. W. Ghonaim, G. M. Fraser, C. G. Ellis, J. Yang, and D. Goldman, "Modeling steady state SO_2-dependent changes in capillary ATP concentration using novel O_2 micro-delivery methods," *Frontiers in Physiology*, vol. 4, 2013.

[4] N. W. Ghonaim, "Investigating conducted microvascular response to localized oxygen delivery in vivo using a novel micro-delivery approach," 2013.

[5] J. Wan, W. D. Ristenpart, and H. A. Stone, "Dynamics of shear-induced ATP release from red blood cells," *Proceedings of the National Academy of Sciences*, vol. 105, no. 43, pp. 16432–16437, 2008.

[6] J. C. McDonald, D. C. Duffy, J. R. Anderson, D. T. Chiu, and H. Wu, "Fabrication of microfluidic systems in poly(dimethylsiloxane)," *Electrophoresis*, no. 21, pp. 27–40, 2000.

[7] S. Prahl, "Optical absorption of hemoglobin," tech. rep., Oregon Medical Laser Center, 1999.

[8] M. Deluca and W. McElroy, "Purification and properties of firefly luciferase," in *Methods in Enzymology*, vol. 57, pp. 3–15, Elsevier, 1978.

[9] J. E. Jagger, R. M. Bateman, M. L. Ellsworth, and C. G. Ellis, "Role of erythrocyte in regulating local O2 delivery mediated by hemoglobin oxygenation," *American Journal of Physiology-Heart and Circulatory Physiology*, vol. 280, no. 6, pp. H2833–H2839, 2001.

[10] R. S. Sprague, A. H. Stephenson, E. A. Bowles, M. S. Stumpf, and A. J. Lonigro, "Reduced expression of Gi in erythrocytes of humans with type 2 diabetes is associated with impairment of both cAMP generation and ATP release," *Diabetes*, vol. 55, no. 12, pp. 3588–3593, 2006.

[11] R. M. Bateman, M. D. Sharpe, J. E. Jagger, and C. G. Ellis, "Sepsis impairs microvascular autoregulation and delays capillary response within hypoxic capillaries," *Critical Care*, vol. 19, no. 1, p. 389, 2015.

[12] D. Goldman, G. M. Fraser, C. G. Ellis, R. S. Sprague, M. L. Ellsworth, and A. H. Stephenson, "Toward a multiscale description of microvascular flow regulation: O_2-dependent release of ATP from human erythrocytes and the distribution of ATP in capillary networks," *Frontiers in Physiology*, vol. 3, p. 246, 2012.

[13] C. G. Ellis, R. M. Bateman, M. D. Sharpe, W. J. Sibbald, and R. Gill, "Effect of a maldistribution of microvascular blood flow on capillary O_2 extraction in sepsis," *American Journal of Physiology-Heart and Circulatory Physiology*, vol. 282, no. 1, pp. H156–H164, 2002.

[14] J.-L. Vincent and D. De Backer, "Microvascular dysfunction as a cause of organ dysfunction in severe sepsis," *Critical Care*, vol. 9, no. 4, p. S9, 2005.

Appendix A

Animal Ethics Approval

2016-078:2:

AUP Number: 2016-078
AUP Title: Characterization of the Dynamics of the Local O2 Regulatory System and Role of the Red Blood Cell In Situ

Yearly Renewal Date: 09/01/2018

The YEARLY RENEWAL to Animal Use Protocol (AUP) 2016-078 has been approved by the Animal Care Committee (ACC), and will be approved through to the above review date.

 Please at this time review your AUP with your research team to ensure full understanding by everyone listed within this AUP.

As per your declaration within this approved AUP, you are obligated to ensure that:

        1) Animals used in this research project will be cared for in alignment with:
                        a) Western's Senate MAPPs 7.12, 7.10, and 7.15
                         http://www.uwo.ca/univsec/policies_procedures/research.html
                        b) University Council on Animal Care Policies and related Animal Care
Committee procedures http://uwo.ca/research/services/animalethics/animal_care_and_use_policies.html
        2) As per UCAC's Animal Use Protocols Policy,
                        a) this AUP accurately represents intended animal use;
                        b) external approvals associated with this AUP, including permits and scientific/departmental peer
approvals, are complete and accurate;
                        c) any divergence from this AUP will not be undertaken until the related Protocol Modification is
approved by the ACC; and
                        d) AUP form submissions - Annual Protocol Renewals and Full AUP Renewals - will be submitted
                        and attended to within timeframes outlined by the ACC.   http://uwo.ca/research/services/
animalethics/animal_use_protocols.html
        3) As per MAPP 7.10 all individuals listed within this AUP as having any hands-on animal contact will
                        a) be made familiar with and have direct access to this AUP;
                        b) complete all required CCAC mandatory training; and
                        c) be overseen by me to ensure appropriate care and use of animals.
        4) As per MAPP 7.15,
                        a) Practice will align with approved AUP elements;
                        b) Unrestricted access to all animal areas will be given to ACVS Veterinarians and ACC Leaders;
                        c) UCAC policies and related ACC procedures will be followed, including but not limited to:
                                        i) Research Animal Procurement
                                        ii) Animal Care and Use Records
                                        iii) Sick Animal Response
                                        iv) Continuing Care Visits
        5) As per institutional OH&S policies, all individuals listed within this AUP who will be using or potentially exposed to
hazardous materials will have completed in advance the appropriate institutional OH&S training, facility-level training, and reviewed
related (M)SDS Sheets, http://www.uwo.ca/hr/learning/required/index.html

Submitted by: Copeman, Laura
on behalf of the Animal Care Committee
University Council on Animal Care

Richard J. Sové

EDUCATION

09/12-Present **Ph.D. Candidate Medical Biophysics**
University of Western Ontario, London, Ontario

09/08-06/12 **B.M.Sc. Medical Biophysics**
University of Western Ontario, London, Ontario

DOCTORAL RESEARCH EXPERIENCE

Mathematical Modelling
Developed finite difference (2D&3D) and finite element (3D)
models to facilitate the design of systems to desaturate
red blood cells *in-vitro* and *in-vivo*.
Developed a 2D finite element model to investigate the effect
of interstitial geometry and capillary density on glucose
uptake in skeletal muscle.

Microfluidics
Fabricated microfluidic devices using impression moulding
and spin coating techniques.

Video Microscopy
Experience with transmission and epiluminescent
microscopy.

Image Processing
Developed various image processing algorithms to analyze
results of video microscopy.

AFFILIATIONS

Compute Canada, Microcirculatory Society

TEACHING EXPERIENCE

Winter 2017   **Undergraduate Lecturer**
Biophysical Analysis of Oxygen Transport (3rd year)
Medical Biophysics, University of Western Ontario
—-
Prepared and delivered eight one-hour lectures. Performed well on teaching evaluations. Overall, students thought I was effective, well-organized and approachable.

Winter 2017   **Undergraduate Course Development**
Pedagogy in Biophysics (Graduate Course)
Medical Biophysics, University of Western Ontario
—-
Developed curriculum and lecture material for a second year prospective undergraduate course using pedagogical concepts. Development was guided by current literature in pedagogy.

Winter 2013-2017   **Graduate Teaching Assistant**
Biophysical Analysis of Oxygen Transport (3rd year)
Medical Biophysics, University of Western Ontario
—-
Prepared material for, and delivered tutorials to reinforce lecture material through practice examples and assignment questions. Prepared and delivered short quizzes. Graded exams, quizzes and assignments.

Winter 2014-2016   **Guest Lecturer**
Finite Difference Method (3rd year)
Medical Biophysics, University of Western Ontario
—-
Prepared and delivered a two-lecture series on an introduction to numerical solutions to mass transport problems in biophysics.

Fall 2015   **Graduate Teaching Assistant**
Single Variable Calculus (1st year)
Applied Mathematics, University of Western Ontario
—-
Graded bi-weekly assignments, exams.

SUPERVISORY EXPERIENCE

Summer 2017	**Jason Baek**
Summer 2016	Undergraduate Student (Years 1-3)
Summer 2015	Projects: Measuring Diffusivity of Oxygen in PDMS,
	3D Reconstruction of Vascular Network from Images,
	Functional Imaging Development
	University of Western Ontario

Summer 2017	**Jaryd Christie**
	Undergraduate Student (Year 2)
	Project: Functional Imaging Development
	University of Western Ontario

Summer 2017	**Ande Doornekamp**
Summer 2016	Undergraduate Student (Year 1), High School Co-op Student
Fall 2015	Projects: Developing Computer-Microscope Interface,
	Functional Imaging Development
	University of Western Ontario

Summer 2017	**Isaac Kong**
	Undergraduate Student (Year 3)
	Project: Functional Imaging Development
	University of Western Ontario

Summer 2017	**Laura Mawdsley**
	Undergraduate Student (Year 4)
	Project: Functional Imaging Development
	University of Western Ontario

Winter 2015	**Bryan Meglei**
	Undergraduate Student (Year 3)
	Project: Computational Model of Oxygen in Microfluidics
	University of Western Ontario

COMMITTEES

09/15-09/18	**Graduate Recruitment Committee**
	Medical Biophysics, University of Western Ontario

02/18	**Graduate Program Review Committee**
	Physiology and Pharmacology, University of Western Ontario

SCHOLARSHIPS AND AWARDS

09/16-08/17	**Schulich Doctoral Excellence Award ($10,000)** Schulich School of Medicine and Dentistry
09/14-08/17	**Alexander Graham Bell Canada Graduate Scholarship ($105,000)** Natural Science and Engineering Research Council of Canada
09/14-08/15	**Ontario Graduate Scholarship ($15,000) - declined** Ontario Ministry of Training, Colleges and Universities
10/13	**Vascular Biology 2013 Abstract Award ($500)** Microcirculatory Society
09/13-08/14	**Alexander Graham Bell Canada Graduate Scholarship ($17,500)** Natural Science and Engineering Research Council of Canada
09/13-08/14	**Ontario Graduate Scholarship ($15,000) - declined** Ontario Ministry of Training, Colleges and Universities
09/12-08/14	**Vascular Training Fellowship ($18,000)** Canadian Institute of Health Research
09/11-04/12	**Dr. G.E. Hall Scholarship ($500)** Foundation Western – Awarded to the student with the highest average in third year Medical Sciences University of Western Ontario
09/11-04/12	**Richard Konrad Scholarship in Science ($1,500)** Foundation Western – Awarded to a student in third or fourth year in the Faculty of Science on the basis of academic excellence
05/10-08/10	**Undergraduate Research Award ($6,000)** Natural Science and Engineering Research Council of Canada

PEER REVIEWED PUBLICATIONS

1. **Sové RJ**, Drakos NE, Fraser GM, Ellis CG. Using digital inpainting to estimate incident light intensity for the calculation of red blood cell oxygen saturation from microscopy images. Accepted to Journal of Biophotonics.

2. **Sové RJ**, Goldman D, Fraser GM. A computational model of the effect of capillary density variability on oxygen transport, glucose uptake, and insulin sensitivity in prediabetes. Microcirculation 24: e12342. February 2017.

3. **Sové RJ**, Fraser GM, Goldman D, Ellis CG. Finite element model of oxygen transport for the design of geometrically complex microfluidic devices used in biological studies. PLoS One 11(11): e0166289. November 2016.

4. Stinziano JR, **Sové RJ**, Rundle HD, Sinclair BJ. Rapid desiccation hardening changes the cuticular hydrocarbon profile of *Drosophila melanogaster*. Comp Biochem Physiol 180: 38-42, February 2015.

5. **Sové RJ**, Ghonaim N, Goldman D, Ellis CG. A computation model of a microfluidic device for measuring oxygen-dependent ATP release from erythrocytes. PLoS One 8(11): e81537, November 2013.

PEER REVIEWED PRESENTATIONS
   Oral Presentations
1. **Sové RJ**, Goldman D, Ellis CG. Studying the dynamics of the oxygen-dependent ATP release pathway within erythrocytes using a computational model of a microfluidic device. Oral presentation at Vascular Biology 2013. Hyannis Port, Massachusetts, United States of America.

   Poster Presentations
2. **Sové RJ**, Goldman D, Fraser GM. Novel mathematical model of glucose transport in skeletal muscle interstitium. Physiology 2016. Dublin, Leinster, Ireland.

3. **Sové RJ**, Goldman D, Fraser GM. Characterizing insulin resistance using a spatial mathematical model of glucose transport in skeletal muscle interstitium. Muscle Health Research Day 2016. Toronto, Ontario, Canada.

4. **Sové RJ**, Goldman D, Fraser GM. 3D computational model of microfluidic device for cardiovascular screening. Experimental Biology 2016. San Diego, California, United States of America.

5. **Sové RJ**, Goldman D, Fraser GM, Ellis CG. 3D model of device for cardiovascular screening. London Health Research Day 2016. London, Ontario, Canada.

6. **Sové RJ**, Goldman D, Fraser GM, Ellis CG. Measurement and analysis of the dynamics of erythrocyte oxygen-dependent ATP release. Experimental Biology 2015. Boston, Massachusetts, United States of America.

7. **Sové RJ**, Goldman D, Ellis CG. A computational approach to studying the dynamics of oxygen-dependent ATP release from erythrocytes. London Health Research Day 2014. London, Ontario, Canada.

8. **Sové RJ**, Ghonaim NW, Goldman D, Ellis CG. Computational analysis of a microfluidic device for measuring oxygen dependent ATP release from erythrocytes. Experimental Biology 2012. San Diego, California, United States of America.

9. **Sové RJ**, Ghonaim NW, Goldman D, Ellis CG. Dynamics of oxygen dependent release of ATP from erythrocytes. London Health Research Day 2012. London, Ontario, Canada.